Final Scientific/Technical Report
Cover Page

Enhancement of SOFC Cathode Electrochemical Performance Using Multi-Phase Interfaces

- Federal Agency and Organization Element to Which Report is Submitted: Department of Energy, National Energy Technology Laboratory, Solid State Energy Conversion Alliance (SECA) Core Technology Program
- Federal Grant or Other Identifying Number Assigned by Agency: Award Number: DE-FE0009435
- Project Title: Enhancement of SOFC Cathode Electrochemical Performance Using Multi-Phase Interfaces
- PD/PI Name, Title and Contact Information (e-mail address and phone number): Dane Morgan, Associate Professor, Room 244 MSE, 1509 University Ave, Madison, WI 53706; ddmorgan@wisc.edu; phone: 608-265-5879, fax: 608-262-8353.
- DUNS Number: 001425594
- Recipient Organization (Name and Address): The Board of Regents of the University of Wisconsin System, Department: Research & Sponsored Programs Division: Graduate School, Suite 6401, 21 N Park St, Madison, WI 53715-1218
- Project/Grant Period (Start Date, End Date): 10/01/2012-09/30/2015
- Submission Date: 12/30/15
- Reporting Period: 01/01/2013-09/30/2015
- Report Term or Frequency: Final Report
- Months Completed: 36 of 36
- Signature of Submitting Official (electronic signatures (i.e., Adobe Acrobat) are acceptable):

  Submitted by Dane Morgan

  Dane Morgan

Disclaimer

Abstract

This work explored the use of oxide heterostructures for enhancing the catalytic and degradation properties of solid oxide fuel cell (SOFC) cathode electrodes. We focused on heterostructures of Ruddlesden-Popper and perovskite phases. Building on previous work showing enhancement of the Ruddlesden-Popper $(La,Sr)_2CoO_4$ / perovskite $(La,Sr)CoO_3$ heterostructure compared to pure $(La,Sr)CoO_3$ we explored the application of related heterostructures of Ruddlesden-Popper phases on perovskite $(La,Sr)(Co,Fe)O_3$. Our approaches included thin-film electrodes, physical and electrochemical characterization, elementary reaction kinetics modeling, and ab initio simulations. We demonstrated that Sr segregation to surfaces is likely playing a critical role in the performance of $(La,Sr)CoO_3$ and $(La,Sr)(Co,Fe)O_3$ and that modification of this Sr segregation may be the mechanism by which Ruddlesden-Popper coatings enhance performances. We determined that $(La,Sr)(Co,Fe)O_3$ could be enhanced in thin films by about 10× by forming a heterostructure simultaneously with $(La,Sr)_2CoO_4$ and $(La,Sr)CoO_3$. We hope that future work will develop this heterostructure for use as a bulk porous electrode.

Table of Contents

1 **EXECUTIVE SUMMARY** **6**

2 **MILESTONE SUMMARY** **8**

3 **PUBLICATIONS** **11**

4 **MOTIVATION AND SCOPE** **12**

5 **THRUST 1: CATHODE FILM GROWTH AND PHYSICAL AND ELECTROCHEMICAL CHARACTERIZATION** **13**

5.1 METHODOLOGY 13

5.1.1 Target Synthesis *13*

5.1.2 Film Deposition *13*

5.1.3 Structure and roughness characterizations *13*

5.1.4 Electrochemical impedance spectroscopy (EIS) *14*

5.1.5 Ex situ Auger electron spectroscopy (AES) *15*

5.2 PROJECT I. LSC_{113} DECORATED LSC_{214} FILMS 15

5.2.1 Sample fabrication *15*

5.2.2 Results on Surface oxygen reduction activity and surface chemistry *16*

5.2.2.1 Surface oxygen reduction activity of LSC_{214} decorated with LSC_{113} (LSC_{113}/LSC_{214}) 16

5.2.2.2 Surface chemistry of both LSC_{113}/LSC_{214} and LSC_{214}/LSC_{113} 17

5.3 PROJECT II. LSC_{214} DECORATION EFFECT ON $LSCF_{113}$ FILM AND ON LSC_{113} FILMS 19

5.3.1 Thickness dependent growth on base film LSCF *19*

5.3.2 Preparation of LSC214 decorated samples *21*

5.3.3 Results of LSC_{214} decorated samples *23*

5.3.3.1 Surface oxygen reduction activity of LSC_{214} decorated $LSCF_{113}$ ($LSC_{214}/LSCF_{113}$) 23

5.3.3.1 Surface stability of pure LSC_{113} film and LSC_{214} film 24

5.4 PROJECT III. LSN_{214} AND LSC_{214} CO-DECORATED LSCF 26

5.4.1 Growth of LSN_{214} films *26*

5.4.1.1 Methodology 26

5.4.1.2 Film characterizations 27

5.4.2 Results of LSFC surface properties with LSN and LSC decoration *29*

5.4.2.1 Surface Exchange Kinetics of LSC_{214}/LNO_{214}-decorated LSCF113 thin films 29

5.5 PROJECT V. GDC DECORATED LSCF FILMS 32

5.5.1 Sample preparation *32*

5.5.2 Oxygen Surface Exchange Kinetics of LSCF-113 thin films with single layer decoration of GDC *35*

5.6 PROJECT VI. $(LA_{1-X}SR_X)_2CUO_{4\pm\Delta}$ SURFACE DECORATION EFFECT 36

5.6.1 Film deposition and characterizations *36*

5.6.2 Surface Exchange Kinetics of $(La_{1-x}Sr_x)_2CuO_{4\pm\delta}$ thin films *37*

5.6.2.1 Electrochemical Impedance Spectroscopy 37

5.6.2.2 Surface Exchange Kinetics of $(La_{1-x}Sr_x)_2CuO_{4\pm\delta}$ thin films 38

5.7 SURFACE ACTIVITY ENHANCEMENT BY COMPOSITE DECORATION FILMS 40

5.7.1 Film deposition *40*

5.7.2 Surface Decoration Effect on the Surface Stability of ABO3 Oxides *43*

5.7.2.1 Surface Stability of LSC113 and LSCF113 with Surface Decoration 43

5.7.2.2 LSCF-113 thin films with single-layer decoration of mixed LSC-214 and LSC-113 44

5.7.2.3 Oxygen Surface Exchange Kinetics of $LSCF_{113}$ thin films with double-layer decoration of stacked LSC_{214} and LSC_{113} 45

6 **THRUST 2: LINEAR AND NON-LINEAR IMPEDANCE SPECTROSCOPY AND ELEMENTARY KINETICS MODELING OF CATHODES** **47**

6.1 IMPEDANCE MEASUREMENTS ON THIN-FILM LSCF-6428 47
6.1.1 Theory *47*
6.1.2 Experimental *48*
6.1.3 Results *49*
6.1.4 Discussion *51*
6.2 IMPEDANCE MEASUREMENTS ON POROUS LSCF-6428 53
6.2.1 Theory *53*
6.2.2 Experimental *55*
6.2.3 Results & Discussion *56*
6.3 LBF AND LBFM ELECTRODE PREPARATION AND CHARACTERIZATION 60
6.3.1 XRD *60*
6.3.2 SEM *61*
6.4 SUMMARY 62

7 THRUST 3: *AB INITIO* CALCULATIONS AND THERMOKINETIC MODELING 63
7.1 TRENDS IN BULK AND SURFACE OXYGEN DEFECT ENERGETICS OF $LA_{2-X}SR_XMO_{4\pm\Delta}$ (M=CO, NI, AND CU) 63
7.1.1 Ab Initio Modeling Approaches *63*
7.1.2 Ab initio bulk oxygen defect formation energies for $La_{2-x}Sr_xMO_4$ (M=Co, Ni, and Cu) *64*
7.1.3 High throughput ab initio oxygen interstitial formation energies for $La_{2-x}Sr_xCoO_4$ *66*
7.1.4 Ab initio surface oxygen adsorption and oxygen vacancy formation energies for $La_{2-x}Sr_xCoO_4$(x=0.5, 1.0, 1.5) and $La_{2-x}Sr_xNiO_4$ (x= 0.0, 0.5, 1.0) (001) AO Surfaces *67*
7.1.5 Summary *70*
7.2 KINETICS OF OXYGEN SURFACE EXCHANGE ON EPITAXIAL RUDDLESDEN-POPPER-TYPE THIN FILMS AND CORRELATIONS TO FIRST-PRINCIPLES DESCRIPTORS 71
7.2.1 Correlation between the bulk and (001) AO surface layer oxygen 2p band centers of $La_{2-x}Sr_xMO_4$ (M=Co, Ni, and Cu) *71*
7.2.2 Correlations between the bulk and (001) AO surface oxygen defect and adsorption energetics vs. bulk oxygen 2p band centers of $La_{2-x}Sr_xMO_4$ (M=Co, Ni, and Cu) *72*
7.2.3 Correlations between the experimentally measured k^q of the (001) oriented thin films vs. bulk oxygen 2p band centers for $La_{2-x}Sr_xMO_4$ (M=Co, Ni, and Cu) *73*
7.2.4 Correlations between the bulk O 2p-band and experimental activation barriers of D and K* for the RP_{214} and SOFC perovskite materials in the literature* *74*
7.2.5 Summary *76*
7.3 *AB INITIO* SURFACE STABILITY ANALYSIS OF $LSCF_{113}$ AND $LASRCOO_{4\pm\Delta}$ 77
7.3.1 Ab Initio Modeling Approaches *77*
7.3.2 Ab Initio Thermodynamic Modeling of $La_{1-x}Sr_xCo_{1-y}Fe_yO_3$ (001) Surface Stability *79*
7.3.2.1 Ab Initio Surface Thermodynamic analysis 79
7.3.2.2 Ab Initio Predictions for LSC_{113} and $LSCF_{113}$ (001) Surface Stability 81
7.3.3 Ab Initio Thermodynamic Analysis of $LaSrCoO_4$ (001) and (100) Surfaces *86*
7.3.3.1 Ab Initio Surface Stability Analysis for LSC_{214} (001) AO and (100) A_2BO_4 Surfaces 86
7.3.3.2 Stability of the $LSCF_{113}$, LSC_{113}, and LSC_{214} at full Sr substitution relative to decomposition 87
7.3.3.3 Stability of LSC_{113} and LSC_{214} Relative to Binary Metal Oxides 88
7.3.3.4 Stability of $LSCF_{113}$ and $LSCF_{214}$ Relative to Binary Metal Oxides 89
7.3.3.5 Summary 90
7.4 *AB INITIO* MODELING OF $LASRCOO_{4\pm\Delta}/LSCF_{113}$ HETEROINTERFACES 91
7.4.1 Ab Initio modeling for Sr substitution in LSC_{214}, $LSCF_{113}$, and the LSC_{214}–$LSCF_{113}$ interfaces *91*

8 REFERENCES 96

1 Executive Summary

This work has focused on understanding the performance of $La_{2-x}Sr_xMO_4$ (M=Co, Ni, and Cu) (LSM_{214}) heterostructures with (La,Sr)CoO_3 (LSC_{113}) and (La,Sr)(Co,Fe)O_3 ($LSCF_{113}$), with a particular goal of extending the enhanced performance seen in LSC_{214}/LSC_{113} vs. LSC_{113} to yield $LSCF_{113}$ based heterostructures with enhanced performance vs. $LSCF_{113}$. These studies had three thrusts. The first thrust (Sec. 5) consisted of synthesis and physical and electrochemical characterization of thin-film electrodes to assess pure phase and heterostructure performance. These studies included LSC_{113}, $LSCF_{113}$, LSC_{214}, $LSCu_{214}$, LSC_{113}/LSC_{214}, LSC_{214}/LSC_{113}, $LSC_{214}/LSCF_{113}$, $LSN_{214}/LSCF_{113}$, $LSCu_{214}/LSCF_{113}$, and $(LSC_{113}+LSC_{214})/ LSCF_{113}$. The major results of these studies were that LSM_{214} did not enhance $LSCF_{113}$ k*, likely due to it being relatively high Sr content and stable already, unlike LSC113. However, $(LSC_{113}+LSC_{214})/ LSCF_{113}$ did yield an ~10× enhancement in k*, perhaps due to forming high-Sr LSC_{113} phase. This result came too late in the project to test in a porous electrode but such a testing is an important future step. Many other results from this very large set of samples are discussed below.

The second thrust (Sec. 6) focused on using Linear and Non-Linear Electrochemical Impedance Spectroscopy (LEIS and NLEIS, respectively) combined with elementary kinetics modeling to determine rate-limiting steps and active mechanisms. The original goal of this work was to help understand and guide optimization of the heterostructured systems. However, the failure of the $LSCF_{113}$ heterostructures to yield enhanced performance until near the end of the project meant that we focused our efforts on more fundamental aspects. In particular, we used this thrust to better understand thin film and porous electrode $LSCF_{113}$, including under ageing conditions for the latter. The major results of this study suggested that $LSCF_{113}$ films and porous electrode electrochemical response could only be explained by invoking models with regions of different electrochemical properties (heterogeneous structures). The different regions are likely due to variation in local Sr content, presumably near the surface. This result is consistent with our previous LSC_{113} studies, and consistent with the understanding obtained from thrust one of k* enhancement being related to control of heterogeneous Sr-enriched surface regions. The ageing studies also suggested that degradation in $LSCF_{113}$ has a component changing the non-linear impedance. These changes are potentially from cation rearrangement near the surface, as changes in surface cations can impact the non-linear response and are expected to take place on the time scale observed. The most likely candidate is segregation/precipitation of Sr and/or changes in the balance of Co and Fe at the surface, which could be further studied by careful time-dependent characterization of surface composition (e.g., with Auger spectroscopy). We have not had time to perform such studies ourselves but they would be a useful focus for future work. It is not clear how to suppress such changes as they are likely due to equilibration under operating conditions, but they potentially might be controlled by changes in the electronic and strain state of the surface, e.g., through doping. However, it should be notes that the dominant changes were in the linear impedance, likely due to changes in surface exchange rate, perhaps from alteration in surface area.

The third thrust (Sec. 7) focused on using ab initio methods to assess hypotheses and suggest mechanisms of surface exchange in the pure and heterostructured systems. These studies found that LSC_{113} and $LSCF_{113}$3 both have strong Sr segregation, but that the former is weaker and less stable vs. Sr segregation into the LSC_{214} phase. These results strongly support the interpretation emerging from the film and NLEIS studies that LSC_{113} and $LSCF_{113}$ have Sr enriched surfaces, and that LSC_{214} can further enrich the LSC_{113}, enhancing its performance, but has little impact on the $LSCF_{113}$, consistent with limited enhancement. The ab initio studies also assessed the stable defects

in the 214 phases and extended the O2p band center descriptor to the 214 phase, demonstrating trends opposite those found in 113. The defects energies and change in slope with O2p band vs. 113 is fully consistent with 214 operating entirely by an interstitial mechanism, and provides strong evidence that these materials are dominated by interstitial carriers under all conditions studied to date.

Together these thrusts have yielded significant new understanding of the structures and mechanisms controlling both pure and heterostructured oxide surface exchange, as well as obtained the goal of providing a new LSCF-based heterostructured material with ~10× enhancement. This work yielded 5 publications (see Sec. 3)

2 Milestone Summary

Below is a summary of all the final milestones and their status. All milestones were completed or altered/removed due to a change in project approach resulting from the poor performance of the original project concept.. Updates to the milestones were made during the project in response to what was learned during the research and a history of all the milestone changes is also included.

Milestone Status Report				
Selected Milestones for Completion in FY 13 (Oct. 1 2012 – Sept. 30 2013) PMP Milestones: 1,2,3,4a,4b,5,6,7,8,9,10,11,12				
Milestone Description	**Planned Completion date**	**Actual Completion Date**	**Verification Method**	**Comments (Progress, Issues, etc.)**
Milestone 1 (MIT): Initial electrode synthesis and characterization: As part of Task 2 we will synthesize and physically characterize at least one LSCF-113 control electrode and at least one LSCF-113 decorated with LSC-214 electrode.	9/30/2013	9/30/2013	Report on results	100%
Milestone 4a (UWi): Single phase ab-initio modeling: As part of Task 4.2 we will perform ab-initio simulations of the LSC-214 and LSCF-113 to understand dopant, defect, and O species energetics and oxygen reduction reaction kinetics.	9/30/2013	09/30/2013	Report on results	100%
Milestone 5 (UWa): Single phase continuum modeling: As part of Task 4.1 we will perform continuum simulations of the LSCF-113 to understand oxygen reduction reaction kinetics.	9/30/2013	6/30/14	Report on results	100%

Selected Milestones for Completion in FY 14 (Oct. 1 2013 – Sept. 30 2014) PMP Milestones: 1,2,3,4a,4b,5,6,7,8,9,10,11,12				
Milestone Description	**Planned Completion date**	**Actual Completion Date**	**Verification Method**	**Comments (Progress, Issues, etc.)**
Milestone 2 (MIT): As part of Task 3.1 we will pattern at least one LSC-214/LSCF-113 and one LNO-214/LSCF-113 electrode and initiate linear electrochemical impedance spectroscopy (EIS) measurements on these electrodes.	09/30/2014	7/30/14	Report on results	100%
Milestone 11 (MIT): Pattern and perform physical and electrochemical characterization on least one LNO-214 and LSCF-113 electrode to assess surface	09/30/2014	Removed	Removed	Removed

stability and activity vs. time.				
Milestone 3 (UWa): As part of Task 3.2 we will initiate nonlinear electrochemical impedance spectroscopy (NLEIS) measurements on LSCF porous electrodes.	09/30/2014	06/30/15	Report on results	100%
Milestone 6 (UWa): As part of Task 5 we will physically characterize sintered mixtures of LSCF-113 and LSC-214 to assess multiphase mixture structure and stability.	09/30/2014	Removed	Removed	Removed
Milestone 4b (UWi): Single-phase ab-initio modeling: As part of Task 4.2 we will complete ab-initio simulations of the LSC-214 defect chemistry.	09/30/2014	7/30/15	Report on results	100%

Selected Milestones for Completion in FY 15 (Oct. 1 2014 – Sept. 30 2015) PMP Milestones: 1,2,3,4a,4b,5,6,7,8,9,10,11,12				
Milestone Description	**Planned Completion date**	**Actual Completion Date**	**Verification Method**	**Comments (Progress, Issues, etc.)**
Milestone 7 (MIT): As part of Task 2 we will complete synthesis and physical characterization of varied initial Sr in (LSC-214+LSC-113)/LSCF-113.	09/30/2015	09/22/2015	Report on results	100%
Milestone 8 (MIT): As part of Task 3.1 we will complete patterning of varied initial Sr in (LSC-214+LSC-113)/LSCF-113 and complete EIS measurements on this electrode.	09/30/2015	09/22/2015	Report on results	100%
Milestone 9 (UWa): As part of Task 3.2 we will perform long-term degradation studies on LSCF porous electrodes with NLEIS.	09/30/2015	TBD	Report on results	100%
Milestone 10 (UWi): As part of Task 4.1 we will perform ab-initio simulations of the surface stability in LSC-214, LSC-113, LSCF-113.	09/30/2015	TBD	Report on results	100%
Milestone 12 (UWa): As part of Task 5 we will we will perform NLEIS studies on LSCF-113 thin film electrodes.	09/30/2015	TBD	Report on results	100%

Milestone modification record:

1. 10/30/13: Milestone 4 was split into Milestone 4a and Milestone 4b to represent initial and final modeling results.
2. 10/30/13: Milestone 11 was added in response to LSC-214/LSCF-113 providing only mild enhancement over LSCF-113. It is focused on the stability of LSC-113 vs. LSCF-114 to understand why LSC-214/LSC-113 provides large enhancement over LSC-113 but LSC-214/LSCF-113 provides only mild enhancement over LSCF-113.
3. 10/30/13: Milestone 2 was updated to include decoration with La2NiO4 to assess if this might provide more enhancement than the LSC-214.
4. 10/30/13: Milestone 3 was updated to include study of just the "most promising" samples from Milestone 2 to avoid doing detailed NLEIS studies on samples with no or very limited enhancement.
5. 7/30/14:
    a. Milestone 2 was clarified at Briggs White's request.
    b. Milestone 11 was removed as testing degradation of LNO-214/LSCF-113 was of limited interest given the absence of enhancement. The effort for this milestone will now be directed to Sr rich LSC-214/LSC-113 in Milestone 7.

c. Milestone 3 was updated to remove focus on LSC-214/LSCF-113 and LNO-214/LSCF-113 films and instead focus on pure LSCF-113 porous electrodes and their long-term stability. This change was made as no activity enhancement from LSC-214/LSCF-113 or LNO-214/LSCF-113 was seen. This is the first step to Milestone 9.
d. Milestone 6 was removed as it focuses on LSC-214/LSCF-113 porous electrodes. Since LSC-214/LSCF-113 gave little performance enhancement in films or infiltrated electrodes in tests from other groups it does not make sense to pursue it further. The effort for this milestone will now be directed to LSCF degradation studies.
e. Milestone 4b (UWi) was updated to focus on just defect chemistry of LSC214. All surface stability studies were integrated into Milestone 10.
f. Milestone 7,8 were altered as LSC-214/LSCF-113 gave little performance enhancement and so it does not make sense to make multiple patterned electrodes from it, test with EIS, or test for stability. However, we have updated these milestones to focus on Sr variation in LSC-113 and LSC-214 to assess how Sr may increase performance of the heterostructure. The present plan is to focus on a range of Sr in LSC113 although variation in LSC-214 initial Sr is also being explored.
g. Milestone 9 was updated to focus on long-term degradation studies of porous electrode LSCF rather then samples from Milestone 8 as these are of limited interest due to limited performance enhancement. There is now a clear pairing of Milestone 3 doing basic NLEIS on LSCF-113 and then Milestone 9 doing long-term degradation studies with NLEIS on LSCF-113.
h. Milestone 10 was updated to remove the focus on LSC-214/LSCF-113 as this gave little performance enhancement and therefore did not make sense to study further with ab initio methods. This milestone now focuses on just the LSC-214, LSC-113, LSCF-113 surface stability, which appears to be critical to their performance and its coupling to the heterointerface.
i. Milestone 12 was updated to focus on NLEIS studies of thin-film LSCF-113 electrodes. These studies will compliment Milestone 3, which performs NLEIS on porous LSCF-113 electrodes. The focus on LSC-214/LSCF-113 interfaces was removed as these gave little performance enhancement.

6. 7/30/15
   a. Milestone 7,8 were modified to focus on coatings of LSC-214 and LSC-113 on LSCF rather than coating on LSC. This change was made as some encouraging initial results were obtained on the LSCF and we believed that a final effort to realize increased performance of the LSCF material was most beneficial for the project.

3 Publications

1. **Kinetics of Oxygen Surface Exchange on Epitaxial Ruddlesden-Popper Phases and Correlations to First-Principles Descriptors**, Y.L. Lee, D. Lee, X.R. Wang, H.N. Lee, D. Morgan, Y. Shao-Horn, J. Phys. Chem. Lett., Just Accepted Manuscript DOI: 10.1021/acs.jpclett.5b02423 (2015)

2. **Ab initio GGA+U Study of Oxygen Evolution and Oxygen Reduction Electrocatalysis on the (001) Surfaces of Lanthanum Transition Metal Perovskites LaBO3 (B=Cr, Mn, Fe, Co and Ni)**, Y.-L. Lee, M. J. Gadre, Y. Shao-Horn, and D. Morgan, Physical Chemistry Chemical Physics **17**, p. 21643-21663 (2015).
3. **Oxygen surface exchange kinetics and stability of (La,Sr)2CoO4+/-[small delta]/La1-xSrxMO3-[small delta] (M = Co and Fe) hetero-interfaces at intermediate temperatures,** D. Lee, Y. -L. Lee, W. T. Hong, M. Biegalski, D. Morgan, and Y. Shao-Horn, Journal of Materials Chemistry A, 2015. **3**(5): p. 2144-2157.
4. **Enhanced Surface Stability and Electrocatalytic Activity on Epitaxial $La_{0.8}Sr_{0.2}CoO_{3-\delta}$ Thin Films by $La_{0.8}Sr_{0.2}MnO_{3-\delta}$ Decoration,** D. Lee, Y. -L. Lee, A. Grimaud, W. T. Hong, M. Biegalski, D. Morgan, and Y. Shao-Horn, *The Journal of Physical Chemistry C,* (2014), 118 (26), 14326.
5. **Anomalous Interface and Surface Strontium Segregation in (La1-ySry)2CoO4±δ/La1-xSrxCoO3-δ Heterostructured Thin Films**, Z. Feng, Y. Yacob, M. J. Gadre, Y.-L. Lee, W. T. Hong, H. Zhou, M. D. Biegalski, H. M. Christen, S. B. Adler, D. Morgan, and Y. Shao-Horn, Journal of Physical Chemistry Letters 5, p. 1027−1034 (2014).

4 Motivation and Scope

This work was motivated by the recent discovery of dramatically enhanced surface exchange (by up to three orders of magnitude) at LSC_{214}/LSC_{113} interfaces compared to LSC_{113} [1-3]. The central question was whether this enhancement could be extended to the more commercially relevant $LSCF_{113}$ material by forming an oxide heterostructure with the $LSCF_{113}$.

Thus the overall objective of the proposed work was to develop $(La,Sr)(Co,Fe)O_3$ ($LSCF_{113}$) based Solid Oxide Fuel Cell (SOFC) Cathodes *with enhanced oxygen reduction activity and/or durability* through decoration with $(La,Sr)MO_4$ (LSM_{214}) phase or related materials, and to understand how this enhancement occurs. This overall objective was approached through three thrusts:

1. Thrust 1: Grow physically and electrochemically well-characterized thin film electrodes with controlled $LSM_{214}/LSCF_{113}$ interfaces of varying length and under varying synthesis conditions. Characterize these
2. Thrust 2: Measure the electrochemical characteristics of films and porous pure and heterostructured electrodes with linear and non-linear impedance spectroscopy, model these electrochemical responses with elementary reaction kinetics, and use these studies to determine catalytic performance, mechanisms, and the origin of electrocatalytic enhancement at interfaces.
3. Thrust 3: Calculate defect, Sr segregation, and catalytic properties of pure and heterostructured oxides using ab initio methods in order to identify active mechanisms and guide design of active heterostructures.

Pursuing these goals has facilitated extensive understanding of the enhancement from oxide heterostructures, developed a thin film heterostructured electrode with enhanced performance and

durability based on the $LSCF_{113}$ platform, and we hope will support extension to a porous $LSCF_{113}$ based SOFC electrode with enhanced performance.

5 Thrust 1: Cathode Film Growth and Physical and Electrochemical Characterization

5.1 Methodology

5.1.1 Target Synthesis

Various targets were prepared generally by the Pechini methods. Generally, depending on target materials, $La(NO_3)_3 \bullet 6H_2O$, $Co(NO_3)_3 \bullet 6H_2O$, $Sr(NO_3)_2$ or $Fe(NO_3)_3 \bullet 9H_2O$ were dissolved in de-ionized water with ethylene glycol, and citric acid (Sigma-Aldrich, USA) mixture to synthesize powder. After esterification at 100 ºC, the resin was charred at 400 ºC and finally calcined at 850 ºC in air for 10 hours. Pulsed laser deposition (PLD) target pellets with 25 mm diameter were subsequently fabricated by uniaxial pressing at 50 MPa. The pellets were fully sintered for typically 6 to 10 hours in 1200 to 1300 ºC. Exact details for different materials will be described in each sections.

5.1.2 Film Deposition

Pulsed laser deposition was utilized to deposit the epitaxial films or decorated films on Y_2O_3-stabilized ZrO_2 (YSZ) with gadolinium-doped ceria (GDC, 20 mol % Gd) as the buffer layer with thickness ~ 5 nm. Single crystal 9.5 mol% YSZ wafers with (001) orientation and dimensions of 10 × 5 × 0.5 mm (MTI corporation, USA) were used as the substrate. Prior to film deposition, platinum ink (Pt) (#6082, BASF, USA) counter electrodes were painted on one side of the YSZ and dried at 900 ºC in air for 1 hour. The YSZ wafer was affixed to the PLD substrate holder using a small amount of silver paint (Leitsilber 200, Ted Pella, USA) for thermal contact. PLD was performed using a KrF excimer laser at λ = 248 nm, 10 Hz pulse rate and 45 mJ pulse energy under an oxygen partial pressure, $p(O_2)$ of 6.6×10^{-5} atm (50 mTorr) with GDC (~5 nm) at 550 °C. Then, films were deposited on GDC. The utilization of reflection high-energy electron diffraction (RHEED) enabled an in-situ monitoring of the film growth. After completing the deposition, the samples were cooled down to room temperature in the PLD chamber for ~1 hour under a $p(O_2)$ of 6.6×10^{-5} atm (50 mTorr).

5.1.3 Structure and roughness characterizations

Oxide phase purity and orientation of the thin film systems were investigated via high resolution X-ray diffraction (HRXRD) using a four-circle diffractometer (Panalytical, USA and Bruker D8, Germany). Measurements were performed in normal and off-normal configurations. The in-plane lattice parameter (*a* lattice parameter) was determined from the off-normal $(103)_{pc}$ peak position, respectively and the *c* lattice parameter normal to the film surface was determined from the $(002)_{pc}$ peak positions. Surface morphology was examined by optical microscopy (Carl Zeiss, Germany) and atomic force microscopy (AFM) (Veeco, USA).

5.1.4 Electrochemical impedance spectroscopy (EIS)

In situ electrochemical impedance spectroscopy (EIS) measurements of microelectrodes ~200 µm in diameter were performed using a microprobe station (Karl Süss, Germany) connected to a frequency response analyzer (Solartron 1260, USA) and dielectric interface (Solartron 1296, USA). Temperature was controlled at 550 °C using a heating stage (Linkam TS1500, UK) and data were collected between 1 MHz to 1 mHz using a voltage amplitude of 10 mV. EIS testing temperature was calibrated with a thermocouple contacting the thin film surface and deviation of ± 5 °C was observed. EIS experiments were performed as a function of $p(O_2)$ between 10^{-3} and 1 atm. Multiple electrodes (at least three) of all films were measured by EIS at each temperature and $p(O_2)$ to ensure that the EIS results were reproducible and representative. EIS data of all samples used in this study were found to show nearly perfect semicircle impedances, and typical features in the Nyquist plots are shown in the schematic. Figure 1 shows a representative structure used during EIS measurement. In this case, the sample with stacking layers of $LaSrCoO_{4\pm\delta}$ (LSC_{214}), $La_{0.6}Sr_{0.4}Co_{0.2}Fe_{0.8}O_{3-\delta}$ ($LSCF_{113}$), GDC, YSZ(001) and porous Pt. EIS data were analyzed using an equivalent circuit, where the high-frequency intercept corresponds to the oxygen ion conduction resistance in YSZ and the mid-frequency feature is believed to result from the interface between YSZ and GDC as reported previously.

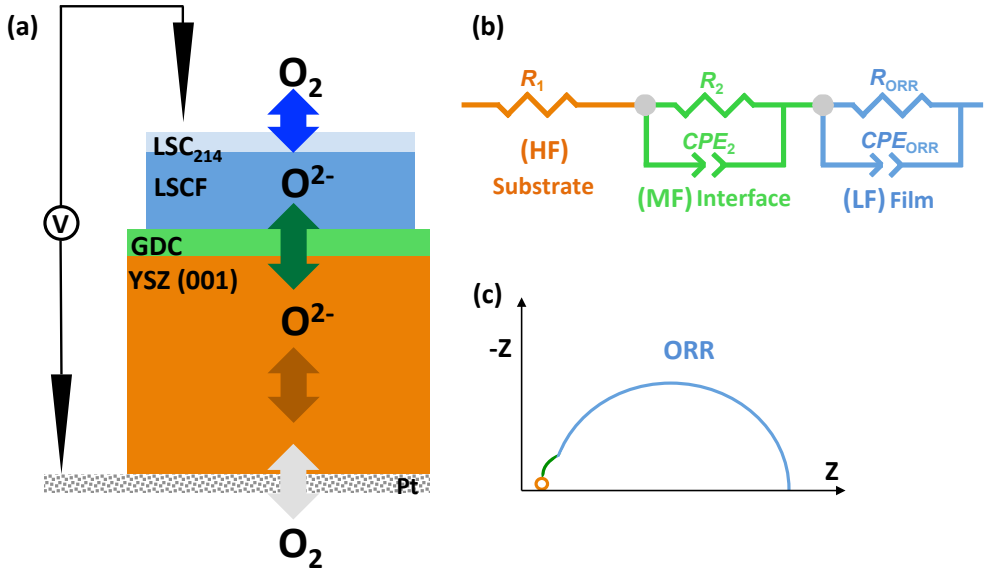

Figure 1. (a) Schematic of a LSC_{214}/$LSCF_{113}$/GDC/YSZ(001)/porous Pt sample and electrochemical testing configuration (not drawn to scale; dimensions provided in the Experimental Methods), (b) equivalent circuit (R_1 = YSZ electrolyte resistance, R_2 = electrode/electrolyte interface resistance, R_{ORR} = oxygen reduction reaction (ORR) resistance, CPE = constant phase element) used to extract ORR kinetics, and (c) characteristic Nyquist plot schematic (color key: red = YSZ/bulk transport, green = GDC/interface, blue = LSCF/ORR).

5.1.5 Ex situ Auger electron spectroscopy (AES)

Ex situ Auger electron spectroscopy (AES) was conducted to analyze the surface chemistry change of LSNO films after annealing on a Physical Electronics 700 Scanning Auger Nanoprobe (PHI, USA) operating at an accelerating voltage of 10 kV. The films were annealed at 550 °C for 6 hours in an oxygen partial pressure of 1 atm before AES data were collected. The AES data were collected from three different areas (10 μm × 10 μm) selected on a sample in an ultra high vacuum chamber.

5.2 Project I. LSC_{113} decorated LSC_{214} films

5.2.1 Sample fabrication

Both LSC_{113} and LSC_{214} were prepared by the Pechini methods. $La(NO_3)_3 \bullet 6H_2O$, $Co(NO_3)_3 \bullet 6H_2O$, $Sr(NO_3)_2$, and separately $La(NO_3)_3 \bullet 6H_2O$, $Co(NO_3)_3 \bullet 6H_2O$, $Sr(NO_3)_2$ were dissolved in de-ionized water with ethylene glycol, and citric acid (Sigma-Aldrich, USA) mixture to synthesize LSC_{113} and LSC_{214} respectively. After esterification at 100 ºC, the resin was charred at 400 ºC and finally calcined at 850 ^{o}C in air for 10 hours. Pulsed laser deposition (PLD) target pellets with 25 mm diameter were subsequently fabricated by uniaxial pressing at 50 MPa. The LSC_{113} and LSC_{214} pellets were fully sintered at 1,200 ºC in air for 6 hours and 1,300 ºC in air for 10 hours, respectively.

Epitaxial thin films of LSC_{214} (15,000 pulses) were prepared by pulsed laser deposition (PLD) on yttria-stabilized zirconia (YSZ(001)) single crystals with gadolinium-doped ceria (GDC) as the buffer layer. A surface decoration with LSC_{113} having different thicknesses, from partial to full coverage (100, 500, 15,000 pulses), was deposited subsequently on top of LSC_{214} (15,000 pulses)/GDC/YSZ(001).

Oxide phase purity and orientation of the thin film systems were investigated via HRXRD using a four-circle diffractometer (Panalytical, USA and Bruker D8, Germany). Measurements were performed in normal and off-normal configurations. The LSC_{214} in-plane lattice parameter (*a* lattice parameter) was determined from the off-normal $(103)_{pc}$ peak position, respectively and the *c* lattice parameter of LSC_{214} normal to the film surface was determined from the $(002)_{pc}$ peak positions. Surface morphology was examined by optical microscopy (Carl Zeiss, Germany) and atomic force microscopy (AFM) (Veeco, USA).

Normal XRD data (Figure 2(a)) clearly show the presence of the $(00l)_{tetragonal}$ (l is integer) peaks of LSC_{214} or $(00l)_{cubic}$ (l is even) peaks of GDC, and YSZ, which indicates $(00l)_{tetragonal}LSC_{214}//(00l)_{cubic}GDC//(00l)_{cubic}YSZ$. Off-normal phi-scan analysis (Figure 2(b)) of the samples allowed us to identify the in-plane crystallographic relationships between GDC and YSZ (a cube-on-cube alignment), LSC_{214} and GDC (a 45^{O} rotation having $[103]_{tetragonal}LSC_{214}//[202]_{cubic}GDC//[202]_{cubic}YSZ$). The constrained lattice parameters of the LSC_{214} decorated with LSC_{113} films were found to be constant as LSC_{113} decoration thickness increases (Figure 3).

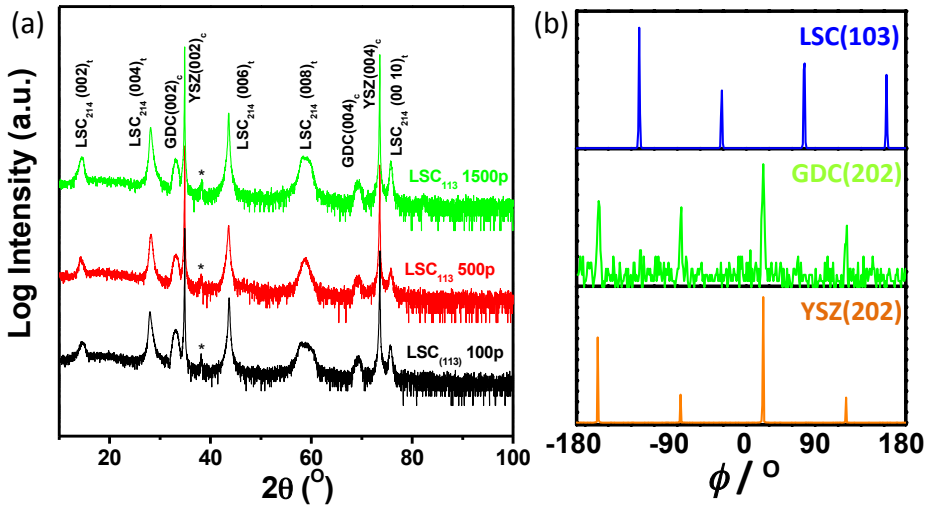

Figure 2. X-ray diffraction analysis. (a) Normal XRD of epitaxial LSC_{214} (~ 15k) decorated with LSC_{113} thin films and (b) Off-normal XRD of epitaxial LSC_{214} (~ 15k) decorated with LSC_{113} thin films, GDC, and YSZ

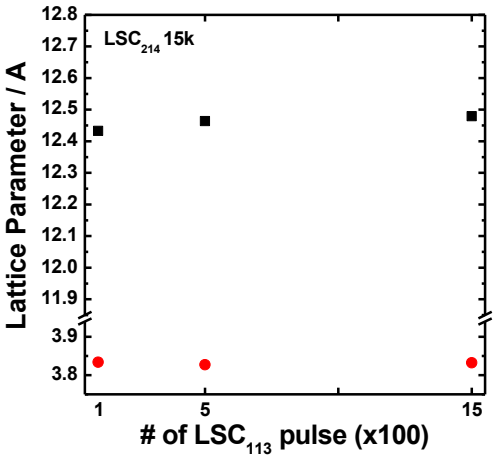

Figure 3. Constrained lattice parameters of LSC_{214} decorated with LSC_{113}

5.2.2 Results on Surface oxygen reduction activity and surface chemistry

5.2.2.1 Surface oxygen reduction activity of LSC_{214} decorated with LSC_{113} (LSC_{113}/LSC_{214})

Figure 4 represents the surface exchange rate of LSC_{214} decorated with LSC_{113}, pure LSC_{214}, and pure LSC_{113} thin films. Interestingly, LSC_{214} decorated with LSC_{113} thin films shows no catalytic enhancement relative to pure LSC_{214}. In the case of LSC_{113} decorated with LSC_{214}, we have already shown that the surface oxygen reduction activity of LSC_{113} decorated with LSC_{214} films can enhance an order of magnitude higher than that of pure LSC_{113} [4]. Han et al.,[5] have proposed the mechanism for enhanced surface oxygen reduction activity of LSC_{214} decorated on LSC_{113}, which is

mainly due to the anisotropic oxygen incorporation of LSC_{214} and the interface strain between LSC_{214} and LSC_{113}. However, the surface activity behavior of LSC_{113}/LSC_{214} cannot be fully explained by the proposed mechanism. Therefore, the surface chemistry of both LSC_{113}/LSC_{214} and LSC_{214}/LSC_{113} was investigated using AES.

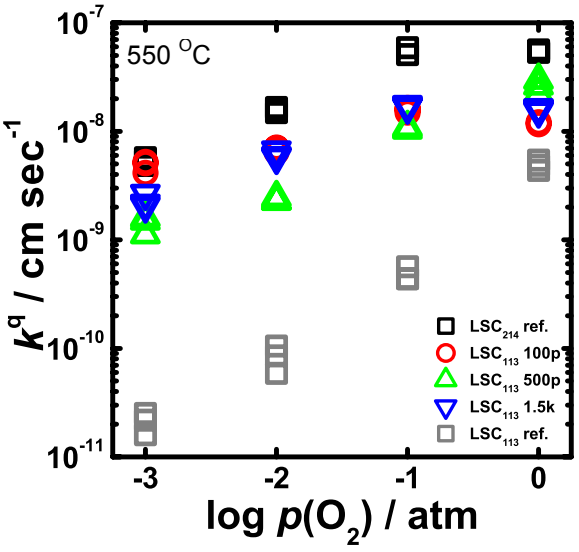

Figure 4. Oxygen partial pressure dependency of the surface exchange coefficients k^q of LSC_{113}/LSC_{214} (○△▽), pure LSC_{214} (□), and pure LSC_{113} (□) thin films.

5.2.2.2 Surface chemistry of both LSC_{113}/LSC_{214} and LSC_{214}/LSC_{113}

The surface chemistry change of pure LSC_{113} thin films before and after annealing at 550 °C for 6 hours in pure oxygen flow is shown in Figure 5(a). No particles were found on the as-deposited LSC_{113} surface, which had a Sr/(La+Sr) ratio comparable to the nominal value (0.2). After annealing, discrete particles were noted on the LSC_{113} surface. AES data of the annealed LSC_{113} film show that the particles formed on the surface had higher Sr/(La+Sr) atomic ratios of ~0.4 than the rest of the surface (~0.1) and the as-deposited LSC_{113} surface (~0.2). In contrast, pure LSC_{214} was found to have no particle formation after annealing (Figure 5(b)). This can be interpreted that the surface of pure LSC_{214} is more stable than that of pure LSC_{113}.

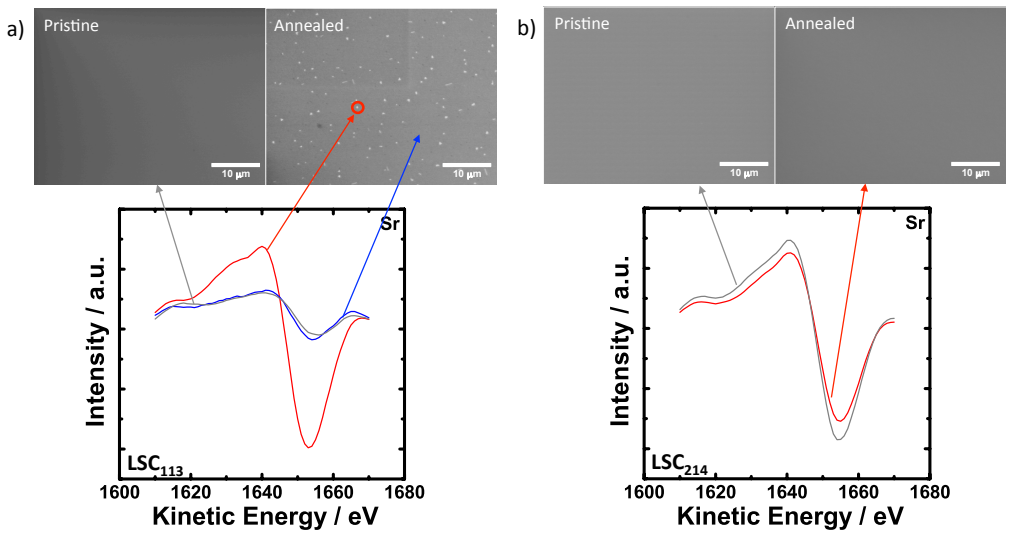

Figure 5. SEM images and Sr peaks before and after annealing at 550 °C for 6 hours in pure oxygen flow of (a) pure LSC_{113} and (b) pure LSC_{214}.

Figure 6 shows the surface chemistry change of LSC_{214}/LSC_{113} that can enhance the surface exchange rate relative to pure LSC_{113} before and after annealing at 550 °C for 6 hours in pure oxygen flow. Compared to the pure LSC_{113} thin film after annealing at the same condition, the density of discrete particles is significantly reduced on annealed LSC_{214}/LSC_{113}. In contrast, annealed LSC_{113}/LSC_{214} shows discrete particles that were not observed on annealed LSC_{214} surface. This can be interpreted that LSC_{113} decoration can lead to the formation of Sr-enrich particles. It is speculated that the surface chemistry may be related to the surface oxygen reduction activity. However, these effects are still not completely understood with just current results. Moreover, the critical thickness of pure LSC_{214} has not been reported, and therefore LSC_{113}/LSC_{214} may be influenced by diffusion limitation because the base film of LSC_{113}/LC_{214} is approximately 250 nm. Thus, in future work we will prepare thin LSC_{214} base films (~ 37nm) decorated with LSC_{113} and further investigate the LSC_{113} decoration effect on LSC_{214} thin film.

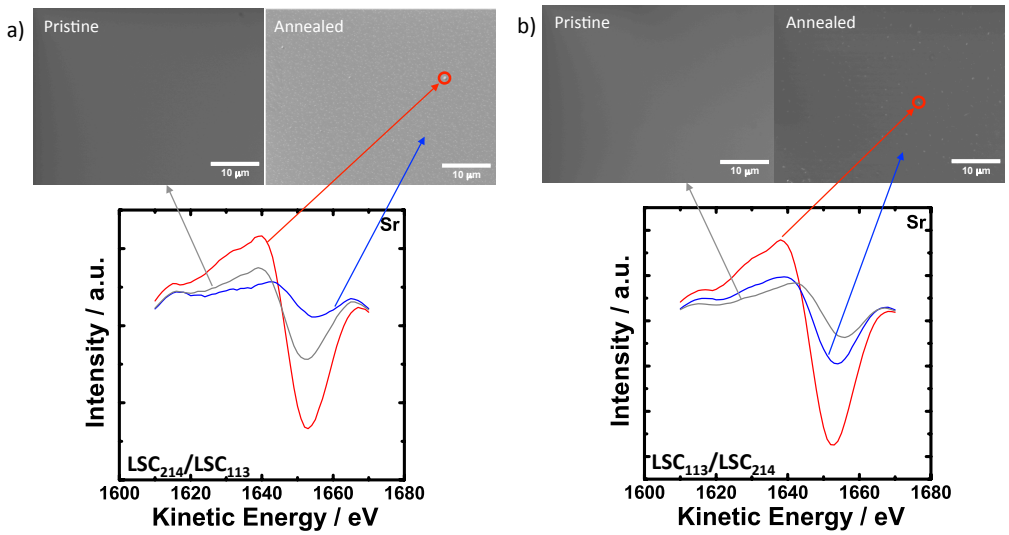

Figure 6. SEM images and Sr peaks before and after annealing at 550 °C for 6 hours in pure oxygen flow of (a) LSC_{214}/LSC_{113} and (b) LSC_{113}/LSC_{214}.

5.3 Project II. LSC_{214} decoration effect on $LSCF_{113}$ film and on LSC_{113} films

5.3.1 Thickness dependent growth on base film LSCF

$La_{0.6}Sr_{0.4}Co_{0.2}Fe_{0.8}O_{3-\delta}$ was prepared by the Pechini methods. $La(NO_3)_3 \bullet 6H_2O$, $Co(NO_3)_3 \bullet 6H_2O$, $Sr(NO_3)_2$ were dissolved in de-ionized water with ethylene glycol, and citric acid (Sigma-Aldrich, USA) mixture to synthesize LSCF and LSC_{214} respectively. After esterification at 100 ºC, the resin was charred at 400 ºC and finally calcined at 850 ^{o}C in air for 10 hours. Pulsed laser deposition target pellets with 25 mm diameter were subsequently fabricated by uniaxial pressing at 50 MPa. The LSCF and LSC_{214} pellets were fully sintered at 1,300 ºC in air for 6 hours and 1,300 ºC in air for 10 hours, respectively.

Epitaxial thin films of LSCF (2,000, 5,000, 15,000, 25,000, and 35,000 pulses) were prepared by PLD on YSZ(001) single crystals with GDC as the buffer layer. A surface decoration with LSC_{214} having different thicknesses, from partial to full coverage (10, 50, 150, 500, 1,000, and 2,500 pulses), was deposited subsequently on top of LSCF (15,000 pulses)/GDC/YSZ(001). Atomic force microscopy images showed that the LSCF reference and LSC_{214} surface decorated films were dense, having low surface roughness of ~ 0.4 nm as shown in Figure 7.

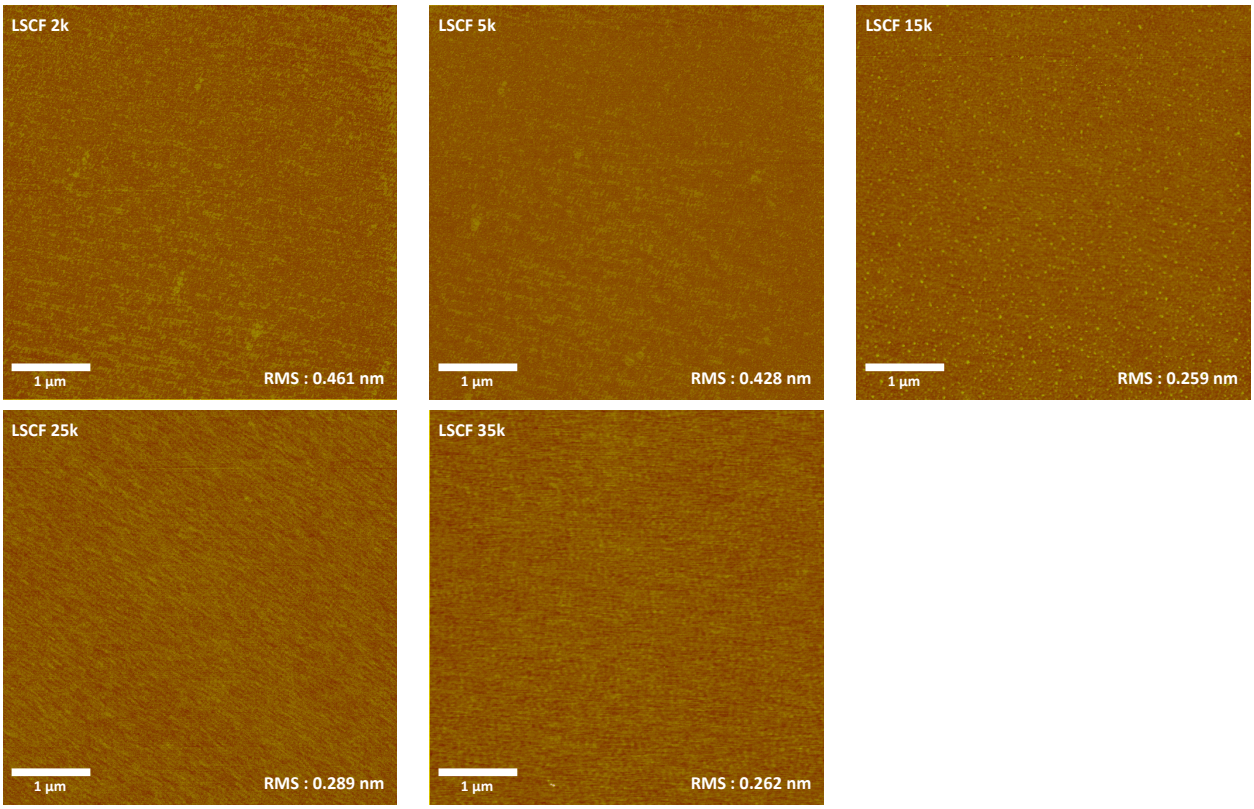

Figure 7. Atomic force microscopy (AFM) images of the LSCF with different thicknesses.

Normal XRD data (Figure 8(a)) clearly show the presence of the $(00l)_{pc}$ (l is integer) or $(00l)_{cubic}$ (l is even) peaks of LSCF, GDC, and YSZ, which indicates

$(00l)_{pc}$LSCF//$(00l)_{cubic}$GDC//$(00l)_{cubic}$YSZ. The subscript "pc" denotes the pseudocubic notation. Off-normal phi-scan analysis (Figure 8(b)) of the samples allowed us to identify the in-plane crystallographic relationships between GDC and YSZ (a cube-on-cube alignment), LSCF and GDC (a 45^{O} rotation having $[100]_{pc}$LSCF//$[110]_{cubic}$GDC// $[110]_{cubic}$YSZ). The relaxed lattice parameters of the LSCF films were found to be ~ 3.9 Å. In-plane and out-of-plane strains were found to be no change at room temperature, as shown in Table 1.

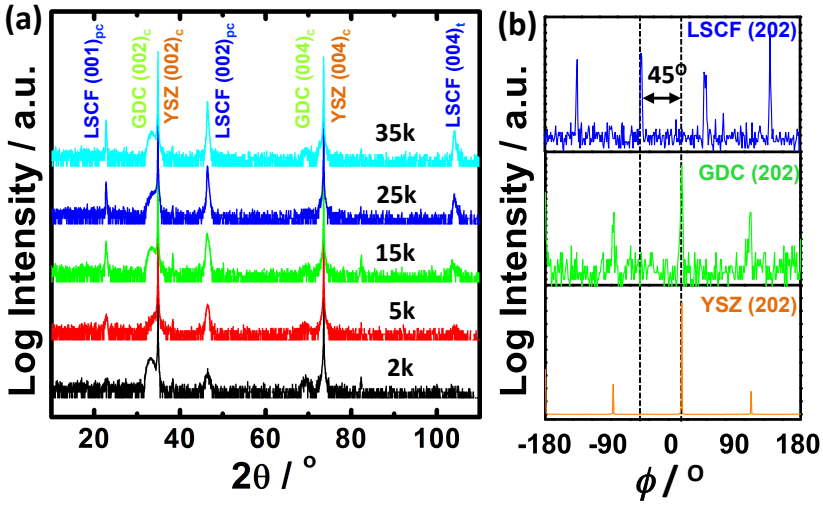

Figure 8. X-ray diffraction analysis. (a) Normal XRD of epitaxial LSCF thin films and (b) Off-normal XRD of epitaxial LSCF thin films (~ 15k), GDC, and YSZ.

Film (pulse)	Constrained normal lattice parameter a (Å)	Constrained in-plane lattice parameter c (Å)	Relaxed film lattice parameter $\hat{a}$ (Å)	Normal strain $\varepsilon_{aa} = \frac{(a-\hat{a})}{\hat{a}}$	In-plane strain $\varepsilon_{cc} = \frac{(c-\hat{c})}{\hat{c}}$
2,000	3.90	3.91	3.90	-0.002 %	0.001 %
5,000	3.90	3.90	3.90	-0.00005 %	0.00003 %
15,000	3.89	3.91	3.90	-0.002 %	0.002 %
25,000	3.91	3.91	3.91	0.0003 %	- 0.0002 %
35,000	3.91	3.91	3.91	-0.0002 %	**1.01**

Table 1. Constrained and relaxed lattice parameters of the LSCF thin films extracted from normal and off-normal HRXRD data at room temperature. The constrained normal and in-plane lattice parameters of the LSCF thin films were calculated from combining the interplanar distances of the $(002)_{pc}$ and $(202)_{pc}$ peaks. For determining the relaxed film lattice parameter $\hat{a}$ and $\hat{c}$, we used the equation: $\frac{(c-\hat{c})}{\hat{c}} = \frac{-2\nu}{1-\nu}\frac{(a-\hat{a})}{\hat{a}}$, assuming $\hat{a} \approx \hat{c}$ and $\nu = 0.25$.

5.3.2 Preparation of LSC214 decorated samples

Epitaxial thin films of $LSCF_{113}$ (~ 62.4 nm) were prepared by PLD on YSZ(001) single crystals with GDC as the buffer layer. A surface decoration with LSC_{214} having different thicknesses, from partial to full coverage (~ 0.1, 0.3, 0.8, 2.4, 5.2 nm), was deposited subsequently on top of $LSCF_{113}$ (~ 62.4 nm)/GDC/YSZ(001). Atomic force microscopy (Veeco, USA) images showed that the $LSCF_{113}$ reference and LSC_{214} surface decorated films were dense, having low surface roughness of ~1 nm as shown in Figure 9.

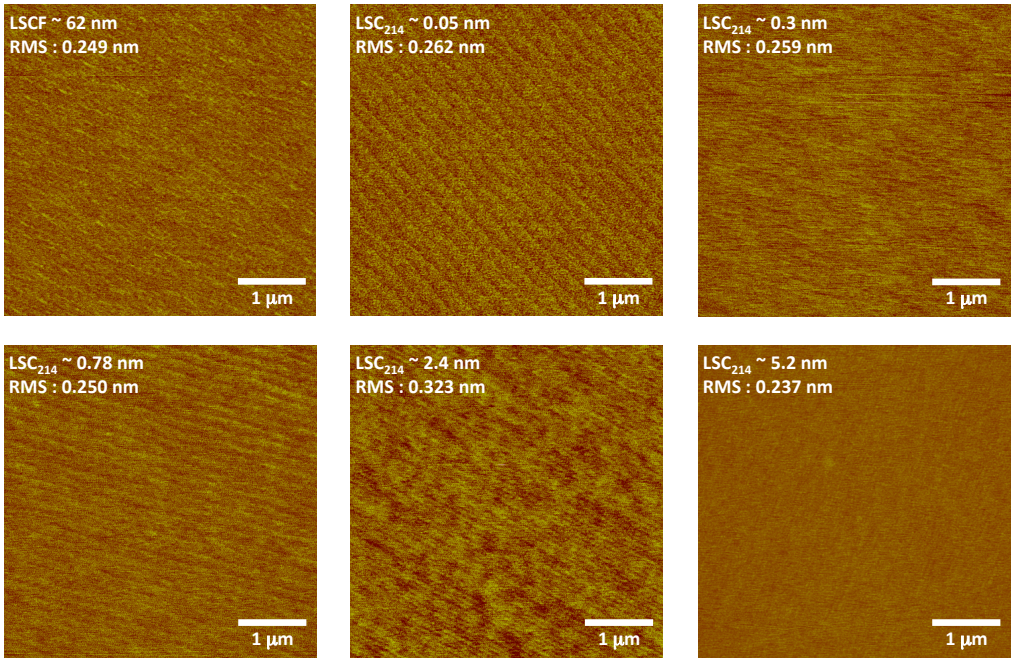

Figure 9. AFM Images of LSC_{214} decorated LSCF (As-deposited). All films show low surface roughness. (RMS < 0.5 nm).

Normal XRD data (Figure 10(a)) clearly show the presence of the $(00l)_{pc}$ (l is integer) peaks of $LSCF_{113}$ or $(00l)_{cubic}$ (l is even) peaks of GDC, and YSZ, which indicates $(00l)_{pc}LSCF_{113}//(00l)_{cubic}GDC//(00l)_{cubic}YSZ$. The subscript "pc" denotes the pseudocubic notation. Off-normal phi-scan analysis (Figure 10(b)) of the samples allowed us to identify the in-plane crystallographic relationships between GDC and YSZ (a cube-on-cube alignment) and LSC_{214}, $LSCF_{113}$ and GDC (a 45^{O} rotation having $[103]_{tetragonal}$ $LSC_{214}/[202]_{pc}LSCF_{113}//[202]_{cubic}GDC//[202]_{cubic}YSZ$).

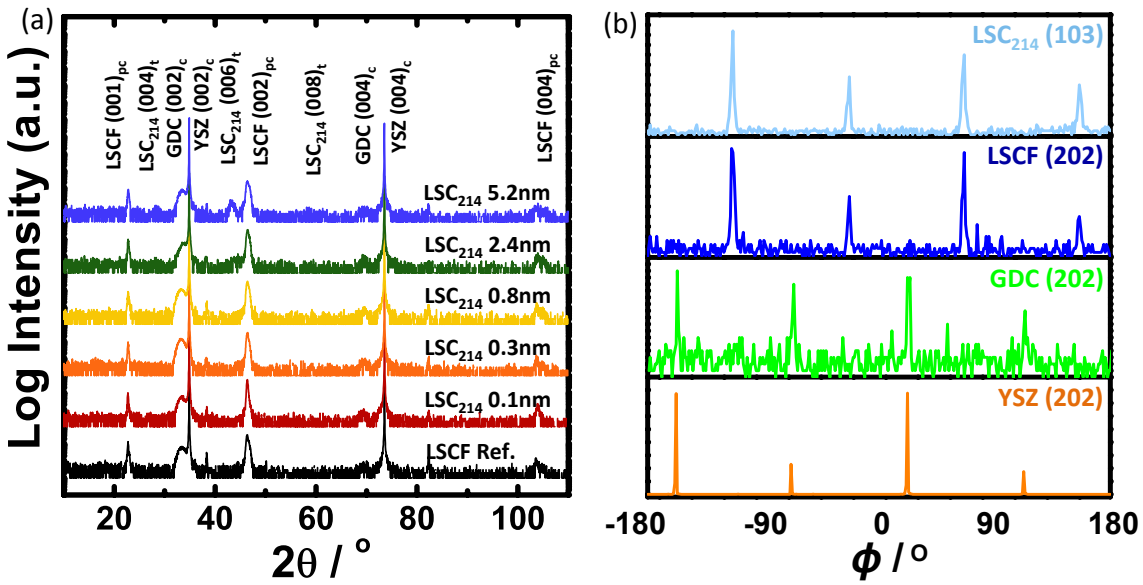

Figure 10. X-ray diffraction (XRD) analysis. (a) Normal XRD of epitaxial $LSCF_{113}$ (~ 62.4 nm) decorated with LSC_{214} thin films and (b) Off-normal XRD of epitaxial $LSCF_{113}$ (~ 62.4 nm) decorated with LSC_{214} thin films, GDC, and YSZ.

The relaxed lattice parameters of the LSC_{214} decorated with $LSCF_{113}$ films were found to be constant as LSC_{214} decoration thickness increases (Figure 11).

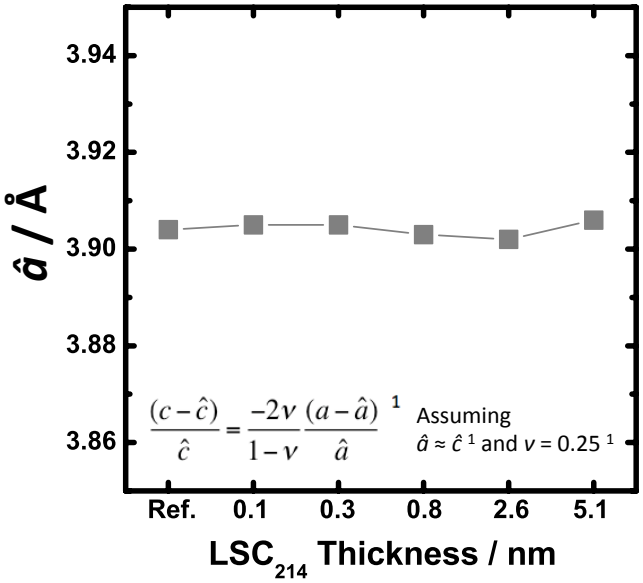

Figure 11. Relaxed lattice parameters of $LSCF_{113}$ decorated with LSC_{214} thin films as a function of LSC_{214} decoration film thickness.

5.3.3 Results of LSC_{214} decorated samples

5.3.3.1 Surface oxygen reduction activity of LSC_{214} decorated $LSCF_{113}$ ($LSC_{214}/LSCF_{113}$)

The predominant semicircle (assigned to ORR impedance) was found to increase with decreasing $p(O_2)$. Representative EIS data collected at 550 ^{O}C in an oxygen partial pressure of 1 atm are shown in Figure 12(a). Figure 12(b) details the equivalent circuit and corresponding Nyquist plot for this experimental system. EIS data of all samples used in this study were found to be very similar in shape, and typical features in the Nyquist plots are shown in the schematic in Figure 12(c). All films with LSC_{214} surface decoration were found to have slightly smaller real impedance relative to the $LSCF_{113}$ reference film of this study. The EIS data were fitted using a standard resistor (R_1) for *HF* and resistors (R_2) in parallel with a constant phase elements (CPE_2) for *MF* and *LF* (R_1-(R_2/CPE_2)-(R_{ORR}/CPE_{ORR})). The HF feature was found unchanged with $p(O_2)$. The MF feature, which was found to have a $p(O_2)$ independent was attributed to interfacial transport of oxygen ions between the LSCF decorated with LSC_{214} film and the GDC layer. We obtained values for R_{ORR}; and knowing the area of the microelectrode ($A_{electrode} = 0.25\ \pi\ d_{electrode}^2$) we can determine the ORR area specific resistance ($ASR_{ORR} = R_{ORR} \cdot A_{electrode}$). The electrical surface exchange coefficient (k^q), which is comparable to k^*[6] was determined using the expression,

$$k^q = RT / 4F^2 R_{ORR} A_{electrode} c_o$$

where R is the universal gas constant (8.314 J mol^{-1} K^{-1}), T is the absolute temperature, F is the Faraday's constant (96,500 C mol^{-1}), and c_o is the lattice oxygen concentration in LSCF,

$$c_o = (3-\delta)/V_m,$$

where V_m is the molar volume of LSCF at room temperature. In this study, c_o was calculated with δ extracted from previous reported values[7].

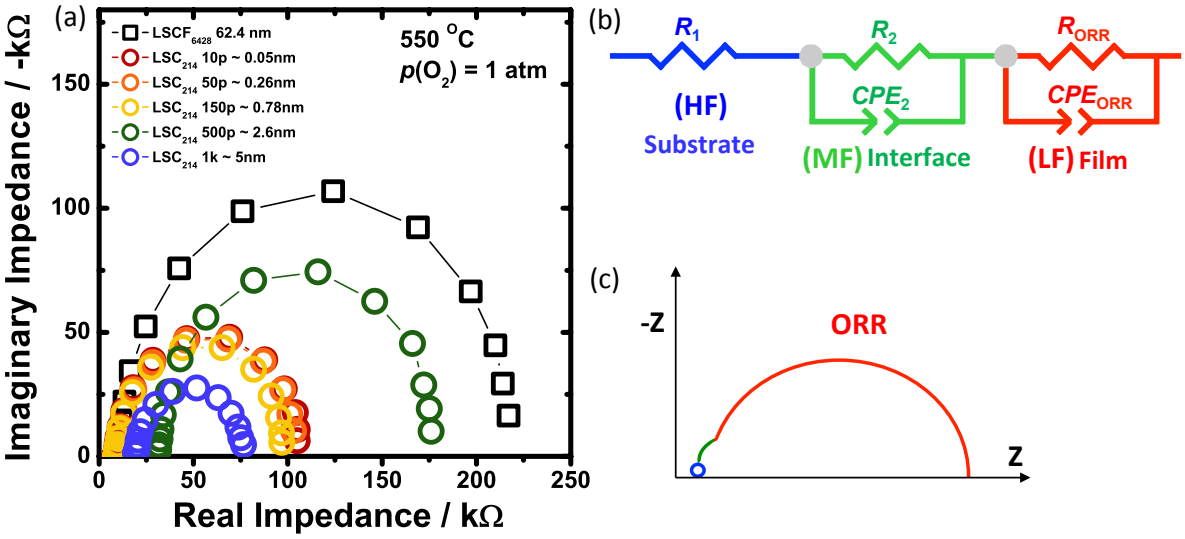

Figure 12. Electrochemical impedance spectroscopy (EIS) results of microelectrodes for LSC_{214} decorated $LSCF_{113}$ thin films at 550 ^{O}C (a) Nyquist plot of the $LSC_{214}/LSCF_{113}$ films in 1 atm. (b) equivalent circuit (R_1 = YSZ electrolyte resistance, R_2 = electrode/electrolyte interface resistance, R_{ORR} = ORR resistance, CPE = constant phase element) used to extract ORR kinetics, and (c) characteristic Nyquist plot schematic (color key: blue = YSZ/bulk transport, green = GDC/interface, red = LSCF/ORR).

Figure 13(a) represents the surface exchange rate (k^q) of LSC_{214} decorated with $LSCF_{113}$, LSCF113 reference, LSC_{214} decorated with LSC_{113}, and LSC_{113} reference thin films. As shown in Figure 13(a), all of the LSC_{214} decorated films showed slightly enhanced k^q values compared to the $LSCF_{113}$ reference while LSC_{113} decorated with LSC_{214} thin film was found to have an order of magnitude higher surface activity than that of pure LSC_{113}[8]. Recently, Han *et al.*[5] have proposed the mechanism for enhanced surface oxygen reduction activity of LSC_{214} decorated on LSC_{113}, which is mainly due to the anisotropic oxygen incorporation of LSC214 and the interface strain between LSC_{214} and LSC_{113}. However, the in-plane and normal strains of $LSC_{214}/LSCF_{113}$ thin films were found to be very similar to that of LSC_{214}/LSC113 thin film. In addition, both $LSC_{214}/LSCF_{113}$ and LSC_{214}/LSC_{113} have the same anisotropic feature of LSC_{214}. Thus, the surface activity behavior of LSC214/LSCF113 cannot be explained by the proposed mechanism. The volume specific capacitances (VSCs) extracted from EIS data using the expression, $VSC = [1/(A_{electrode} \times \text{thickness})]((R_{ORR})1\text{-}nQ)1/n$ (Q is the non-ideal "capacitance", and n is the non-ideality factor of CPE) of the $LSC_{214}/LSCF_{113}$ thin films, corresponding to the change in oxygen nonstoichiometry (δ) induced by the change in the electrical potential, were found to be constant as a function of LSC_{214} decoration thickness. This indicates that the observed kq values of the LSC214/LSCF113 and LSC214/LSC113 might not be contributed by a bulk oxygen content.

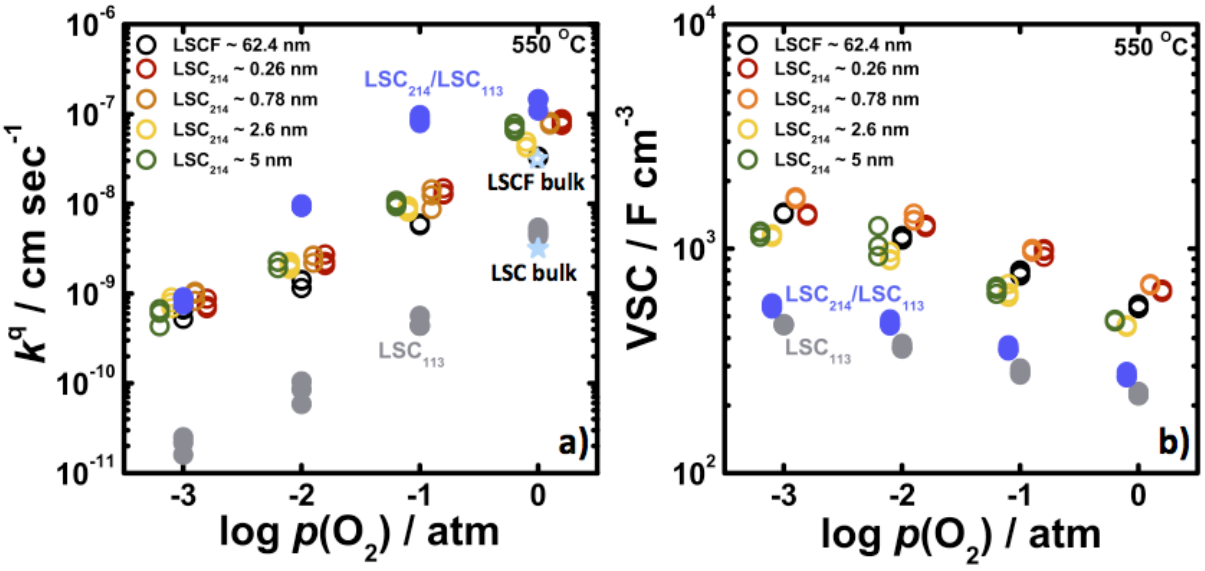

Figure 13. (a) Oxygen partial pressure dependency of the surface exchange coefficients, k^q of $LSC_{214}/LSCF_{113}$ thin films calculated from EIS spectra collected at 550 ^{O}C. Extrapolated bulk k* (approximately equivalent to k^q) values obtained from previous data [6, 7] (b) Oxygen partial pressure dependency of volume specific capacitance (*VSC*) of $LSC_{214}/LSCF_{113}$ thin films calculated from EIS spectra collected at 550 °C.

5.3.3.1 Surface stability of pure LSC_{113} film and LSC_{214} film

The surface chemistry change of pure LSC_{113} thin films before and after annealing at 550 °C for 6 hours in pure oxygen flow is shown in Figure 14(a). No particles were found on the as-deposited LSC_{113} surface, which had a Sr/(La+Sr) ratio comparable to the nominal value (0.2). After

annealing, discrete particles were noted on the LSC_{113} surface. Auger electron spectroscopy data of the annealed LSC_{113} film show that the particles formed on the surface had higher Sr/(La+Sr) atomic ratios of ~ 0.4 than the rest of the surface (~ 0.1) and the as-deposited LSC_{113} surface (~ 0.2). In contrast, pure LSC_{214} was found to have no particle formation after annealing (Figure 14). This can be interpreted that the surface of pure LSC_{214} is more stable than that of pure LSC_{113}.

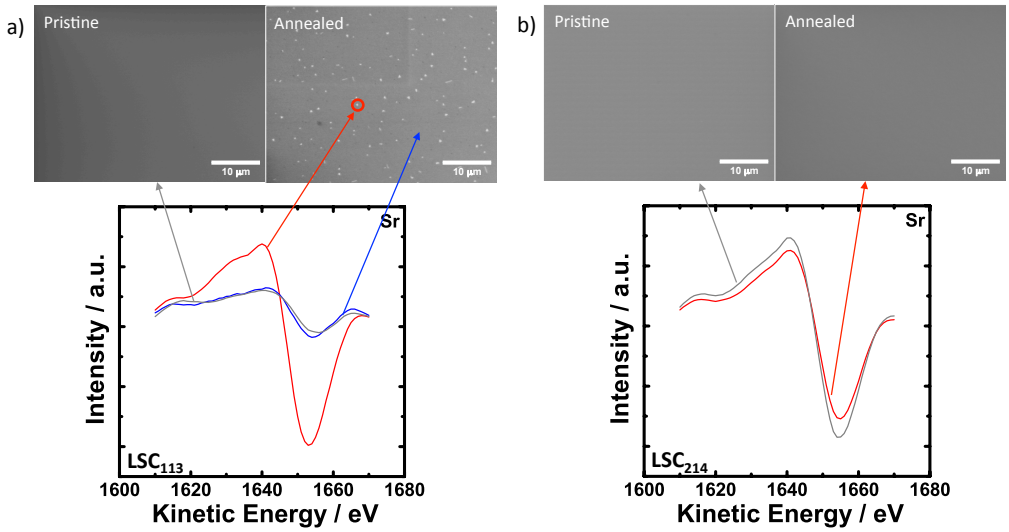

Figure 14. SEM images and Sr peaks from auger electron spectroscopy (AES) before and after annealing at 550 °C for 6 hours in pure oxygen flow of (a) pure LSC_{113} and (b) pure LSC_{214}.

Figure 15 shows the change in the surface exchange rate of LSC_{113} thin film over time. The surface exchange rate was found to reduce significantly after annealing for 5 days. As shown in Figure 14, LSC_{113} can form Sr-enriched particles after annealing, which could influence on the surface exchange rate. Recently, Kubicek *et al.*[9] have reported that Sr-enriched particles can be formed on the surface of $La_{0.6}Sr_{0.4}CoO_{3-\delta}$ after annealing, which can degrade the surface activity. Thus, significantly degraded surface exchange rate of LSC_{113} thin film might be associated with the surface stability of LSC_{113} thin film. In the case of LSC_{214}/LSC_{113}, Feng *et al.*[10] showed that the surface is relatively stable after heat treatment compared to LSC_{113} thin film. This can be interpreted that LSC_{214} decoration might lead to increase in the surface stability of LSC_{113}. However, LSCF is relatively stable compared to LSC_{113}. Therefore, LSC_{214} may not increase in the surface stability of $LSCF_{113}$, which may be the reason for only a slight enhancement of the surface activity.

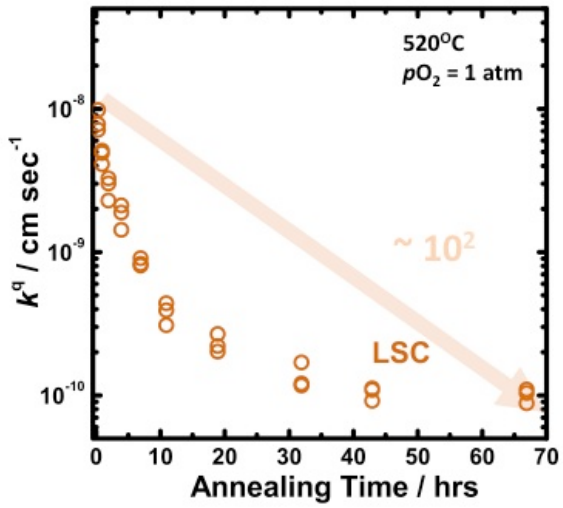

Figure 15. Annealing time dependency of the surface exchange coefficients, k^q of LSC_{113} thin films calculated from EIS spectra collected at 520 ^{O}C.

5.4 Project III. LSN_{214} and LSC_{214} co-decorated LSCF

5.4.1 Growth of LSN_{214} films

5.4.1.1 Methodology

Both $LSCF_{113}$ and $LaNiO_{4\pm\delta}$ (LNO_{214}) were prepared by the Pechini methods. $La(NO_3)_3$•$6H_2O$, $Co(NO_3)_3$•$6H_2O$, $Fe(NO_3)_3$•$9H_2O$, $Sr(NO_3)_2$, and separately $La(NO_3)_3$•$6H_2O$ and $Ni(NO_3)_2$•$6H_2O$ were dissolved in de-ionized water with ethylene glycol, and citric acid (Sigma-Aldrich, USA) mixture to synthesize $LSCF_{113}$ and LNO_{214} respectively. After esterification at 100 ºC, the resin was charred at 400 ºC and finally calcined at 850 ^{o}C in air for 10 hours. Pulsed laser deposition target pellets with 25 mm diameter were subsequently fabricated by uniaxial pressing at 50 MPa. The $LSCF_{113}$ and LNO_{214} pellets were fully sintered at 1,300 ºC in air for 6 hours and 1,300 ºC in air for 10 hours, respectively.

Pulsed laser deposition was utilized to deposit the epitaxial $LSCF_{113}$ decorated with LNO_{214} thin films on YSZ with GDC as the buffer layer with thickness ~ 5 nm. Single crystal 9.5 mol% YSZ wafers with (001) orientation and dimensions of 10 × 5 × 0.5 mm (MTI corporation, USA) were used as the substrate. Prior to $LSCF_{113}$ and GDC deposition, platinum ink (Pt) (#6082, BASF, USA) counter electrodes were painted on one side of the YSZ and dried at 900 ºC in air for 1 hour. The YSZ wafer was affixed to the PLD substrate holder using a small amount of silver paint (Leitsilber 200, Ted Pella, USA) for thermal contact. PLD was performed using a KrF excimer laser at λ = 248 nm, 10 Hz pulse rate and 45 mJ pulse energy under an oxygen partial pressure, $p(O_2)$ of 6.6 × 10^{-5} atm (50 mTorr) with GDC (~5 nm) at 550 °C. Then, $LSCF_{113}$ (10,000 pulses) were deposited on GDC. A surface decoration with LNO_{214} having different thicknesses (50, 150, 500, 1,000 pulses), was deposited subsequently on the top of $LSCF_{113}$/GDC/YSZ(001). The utilization of reflection high-energy electron diffraction (RHEED) enabled an in-situ monitoring of the $LSCF_{113}$ decorated with LNO_{214} film growth. After completing the $LSCF_{113}$ decorated with LNO_{214} deposition, the

samples were cooled down to room temperature in the PLD chamber for ~1 hour under a $p(O_2)$ of 6.6×10^{-5} atm (50 mTorr).

Oxide phase purity and orientation of the thin film systems were investigated via HRXRD using a four-circle diffractometer (PANalytical, USA and Bruker D8, Germany). Measurements were performed in normal and off-normal configurations. The $LSCF_{113}$ in-plane lattice parameter (***a*** lattice parameter) was determined from the off-normal $(202)_{pc}$ peak position (where "pc" denotes the pseudocubic notation) and the ***c*** lattice parameter of $LSCF_{113}$ normal to the film surface was determined from the $(002)_{pc}$ peak position. Surface morphology was examined by optical microscopy (Carl Zeiss, Germany) and AFM (Veeco, USA).

5.4.1.2 Film characterizations

AFM images of as-deposited $LSCF_{113}$ and LNO_{214}-decorated $LSCF_{113}$ films revealed the root-mean-square (RMS) roughness values of 0.613 – 0.791 nm, as shown in Figure 16. The RMS roughness value was found to increase with LNO_{214} film up to 150 pulses, then decreased with increasing LNO_{214} thickness up to 1,000 pluses. Considering that the surface coverage is dependent on the thickness of the film decoration[4], this RMS roughness indicates that thinner thicknesses of LNO_{214} decoration (50 and 150 pulses) result in a partial surface coverage, whereas thicker thicknesses (500 and 1,000 pulses) correspond to full surface coverage.

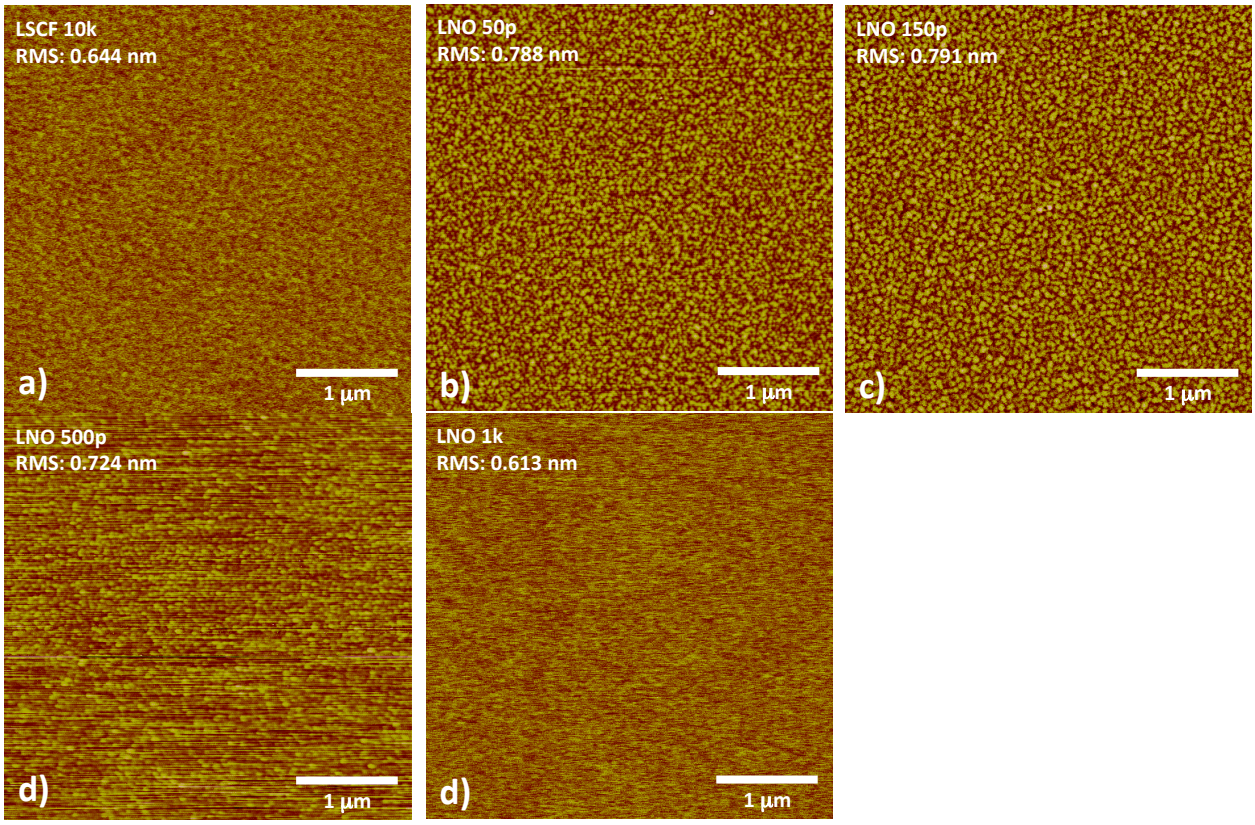

Figure 16. AFM images of (a) as-deposited bare $LSCF_{113}$ 10k, (b) $LSCF_{113}$ with 50p (p=pulses) LNO_{214}, (c) $LSCF_{113}$ with 150p LNO_{214}, (d) $LSCF_{113}$ with 500p LNO_{214}, and (e) $LSCF_{113}$ with 1,000p LNO_{214}. RMS roughness values ranged from 0.613 – 0.791 nm and depend on the thickness of the LNO_{214} decoration.

Normal XRD data (Figure 17(a)) of the undecorated $LSCF_{113}$ and LNO_{214}-decorated $LSCF_{113}$ films clearly show the presence of the $(00l)_{pc}$ (l is integer) peaks of $LSCF_{113}$ and $(00l)_{cubic}$ (l is even) peaks of GDC and YSZ, indicating that the $LSCF_{113}$ film grew epitaxially with the following epitaxial relationships: $(001)_{pc}$ $LSCF_{113}$ // $(001)_{cubic}$GDC // $(001)_{cubic}$YSZ. With LNO_{214} coverage equal to 500 pulses, the $(00l)_{pc}$ (l is integer) peaks of LNO_{214} become visible, which represents $(001)_{tetra.}$ LNO_{214} // $(001)_{pc}$ $LSCF_{113}$ // $(001)_{cubic}$ GDC // $(001)_{cubic}$ YSZ. Off-normal phi-scan analysis of the undecorated $LSCF_{113}$ and LNO_{214}-decorated $LSCF_{113}$ films shows that LNO_{214} $\{103\}_{tetra.}$, $LSCF_{113}$ $\{101\}_{pc}$, GDC $\{202\}_{cubic}$ and YSZ $\{202\}_{cubic}$ have strong peaks with 4-fold cubic symmetry (Figure 17(b)), which reveals the in-plane crystallographic relationships between GDC and YSZ (a cube-on-cube alignment), $LSCF_{113}$ and GDC (an in-plane 45° rotation with $[100]_{pc}$ $LSCF_{113}$ // $[110]_{cubic}$ GDC // $[110]_{cubic}$ YSZ), and $LSCF_{113}$ and LNO_{214} (no rotation with $[100]_{pc}$ $LSCF_{113}$ // $[100]_{pc}$ LNO_{214}), as shown in Figure 17(c).

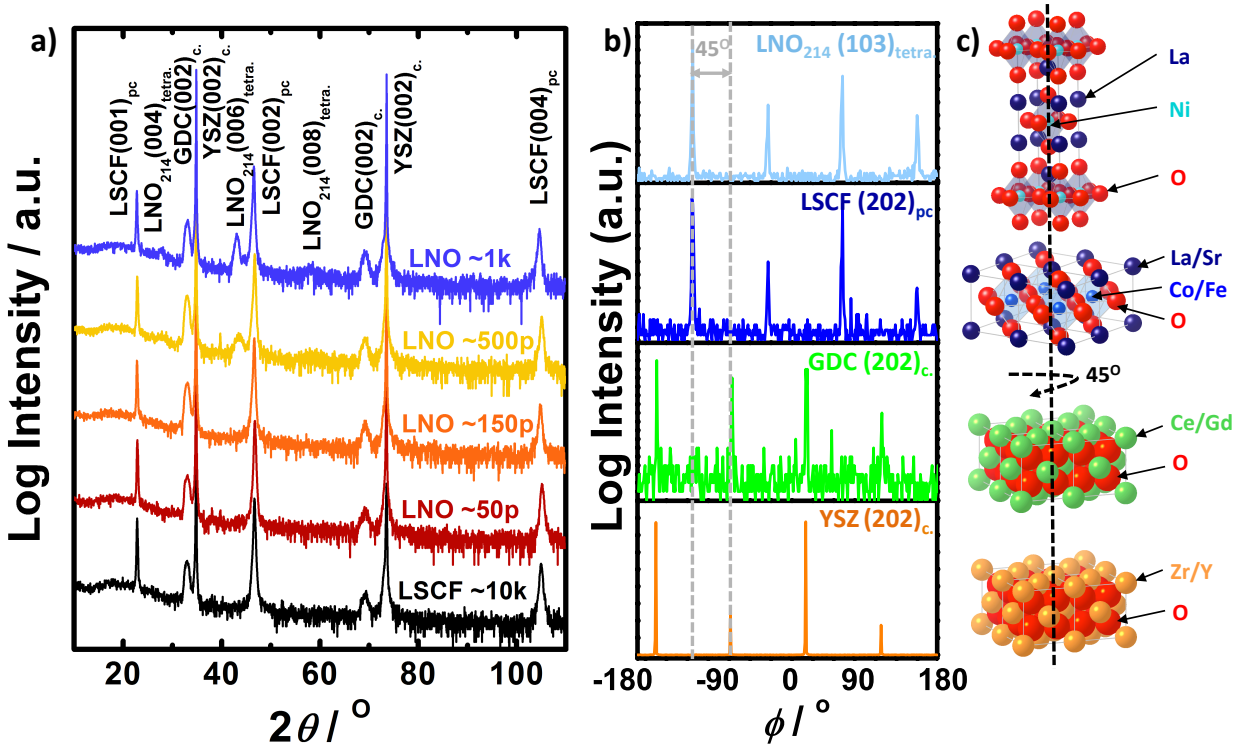

Figure 17. X-ray diffraction (XRD) analysis. (a) Normal XRD of epitaxial $LSCF_{113}$ (10,000 pulses) decorated with LSN_{214} thin films, (b) Off-normal XRD of epitaxial $LSCF_{113}$ (10,000 pulses) decorated with LNO_{214} thin films, GDC, and YSZ, and (c) schematic of the crystallographic rotational relationships among the $LNO_{214}(001)_{tetragonal}$, $LSCF_{113}(001)_{pc}$, $GDC(001)_{cubic}$, and $YSZ(001)_{cubic}$.

The relaxed lattice parameters, $\hat{a}$ of the epitaxial $LSCF_{113}$ films with and without LNO_{214} surface decoration in this study at room temperature did not change significantly with different LNO_{214}

decoration thicknesses, ranging from 3.893 − 3.897 Å, as shown in Table 2. For determining the relaxed film lattice parameter $\hat{a}$ ($LSCF_{113}$), we used the equation: $\frac{(c-\hat{c})}{\hat{c}} = \frac{-2\nu}{1-\nu}\frac{(a-\hat{a})}{\hat{a}}$, assuming $\hat{a} = \hat{c}$ and ν = 0.25[11]. The in-plane strain is given by: $\varepsilon_{cc} = \frac{(c-\hat{c})}{\hat{c}}$ and the out of plane strain by: $\varepsilon_{aa} = \frac{(a-\hat{a})}{\hat{a}}$. In order to compare the lattice parameters and the lattice strains in $LSCF_{113}$ decorated with LNO_{214} samples, relaxed lattice parameters and lattice strains of $LSCF_{113}$ films were also extracted from normal and off-normal HRXRD data.

Table 2: Constrained and relaxed lattice parameters of $LSCF_{113}$ and LNO_{214}-decorated $LSCF_{113}$ films extracted from normal and off-normal XRD data at room temperature. Constrained normal and in-plane lattice parameters of all films were calculated from combining the inter-planar distance of the $LSCF(002)_{pc}$ and $LSCF(202)_{pc}$ peaks.

Samples	Constrained in-plane a / Å	Constrained normal c / Å	Relaxed lattice parameter $\hat{a}$ / Å	In-plane strain $\varepsilon_{aa} = \frac{(a-\hat{a})}{\hat{a}}$ / %	Normal strain $\varepsilon_{cc} = \frac{(c-\hat{a})}{\hat{a}}$ / %
LSCF ref.	3.905	3.884	3.893	0.003	-0.002
LNO 50p	3.912	3.881	3.893	0.005	-0.003
LNO 150p	3.904	3.887	3.894	0.003	-0.002
LNO 500p	3.909	3.882	3.893	0.004	-0.003
LNO 1k	3.900	3.894	3.897	0.001	-0.001

5.4.2 Results of LSFC surface properties with LSN and LSC decoration

5.4.2.1 Surface Exchange Kinetics of LSC_{214}/LNO_{214}-decorated LSCF113 thin films

EIS data of all samples used in this study were found to be very similar in shape, and typical features in the Nyquist plots are shown in the schematic in Figure 18(c). Figure 18(b) details the equivalent circuit and corresponding Nyquist plot for this experimental system. The EIS data were fitted using a standard resistor (R_1) for high-frequency (*HF)* and resistors (R_2) in parallel with a constant phase elements (CPE_2) for middle-frequency (*MF*) and low-frequency (*LF*) *(R_1-(R_2/CPE_2)-(R_{ORR}/CPE_{ORR}))*. Based on the $p(O_2)$ dependence of the three features, physical or chemical process with regard to each frequency range can be determined. The *HF* feature (10^4 – 10^5 Hz) was found unchanged with $p(O_2)$, and its magnitude and activation energy (~1.15 eV) were comparable to those of oxygen ion conduction in YSZ reported previously [12]. The *MF* feature (10^3 – 10^4 Hz), which was found to have a $p(O_2)$ independent feature, was attributed to interfacial transport of oxygen ions between the LSCF film and the GDC layer. In addition, the magnitude of its capacitance was relatively small (~10^{-6} F) compared to the *LF* feature (~10^{-3} F). The *LF* feature (10^{-2} – 10^3 Hz) was found to have a strong $p(O_2)$ dependence. The resistance of the *LF* feature drastically increases as oxygen partial pressure decreases. In the case of thin film samples, the

magnitude of capacitance is due to the oxygen content change in the films. Therefore, the electrode oxygen surface reaction corresponds with the *LF* feature. We obtained values for R_{ORR}; and knowing the area of the microelectrode ($A_{electrode} = 0.25\ \pi\ d_{electrode}^2$) we can determine the ORR area specific resistance ($ASR_{ORR} = R_{ORR} \cdot A_{electrode}$). The electrical surface exchange coefficient (k^q), which is comparable to k^* [13] was determined using the expression,

$$k^q = RT / 4F^2 R_{ORR} A_{electrode} c_o \qquad \textbf{Eqn. 1}$$

where R is the universal gas constant (8.314 J mol^{-1} K^{-1}), T is the absolute temperature, F is the Faraday's constant (96,500 C mol^{-1}), and c_o is the lattice oxygen concentration in LSCF,

$$c_o = (3-\delta)/V_m \qquad \textbf{Eqn. 2}$$

where V_m is the molar volume of LSCF at room temperature. In this study, c_o was calculated with δ extracted from previous reported values.

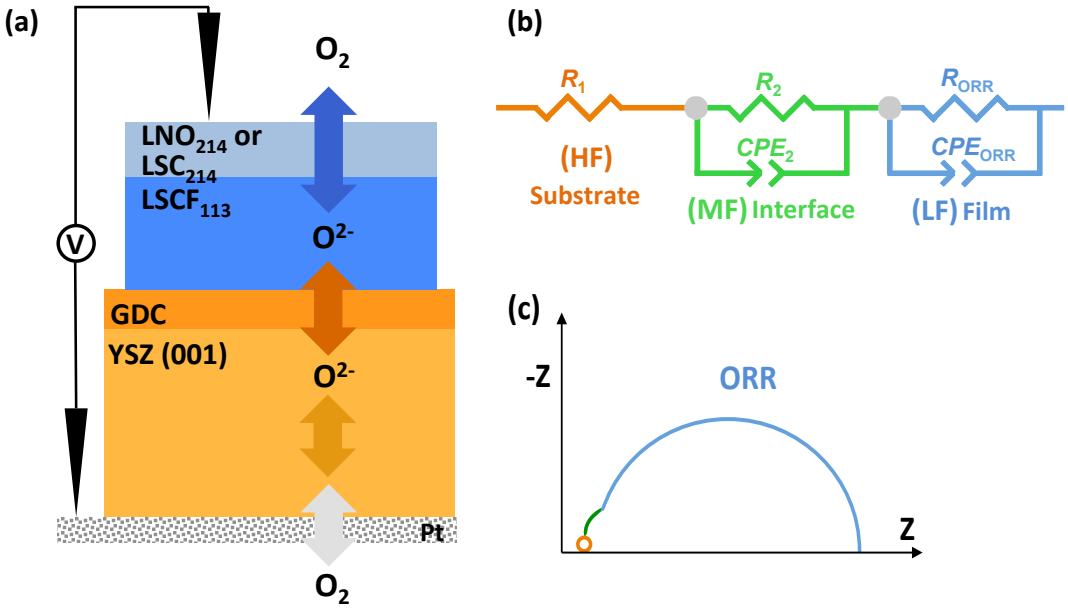

Figure 18. (a) Schematic of a LNO_{214} or $LSC_{214}/LSCF_{113}$/GDC/YSZ(001)/porous Pt sample and electrochemical testing configuration (not drawn to scale; dimensions provided in the Experimental Methods), (b) equivalent circuit (R_1 = YSZ electrolyte resistance, R_2 = electrode/electrolyte interface resistance, R_{ORR} = ORR resistance, CPE = constant phase element) used to extract ORR kinetics, and (c) characteristic Nyquist plot schematic (color key: red = YSZ/bulk transport, green = GDC/interface, blue = LSCF/ORR).

EIS data collected from the undecorated $LSCF_{113}$, LNO_{214}-decorated $LSCF_{113}$, and LSC_{214}-decorated $LSCF_{113}$ thin films at an oxygen partial pressure ($p(O_2)$) of 1 atm and T = 550 °C are shown in Figure 19. Both LNO_{214} and LSC_{214}-decorated $LSCF_{113}$ films were found to have slightly smaller real impedance relative to the undecorated $LSCF_{113}$ reference film of this study.

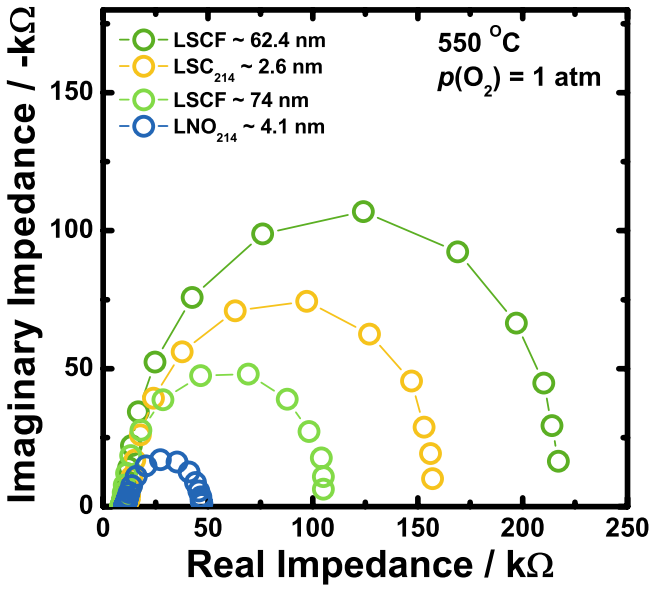

Figure 19. Electrochemical impedance spectroscopy (EIS) results of microelectrodes for LSCF decorated with LNO_{214} or LSC_{214} thin films at 550 ^{O}C.

The k^q values of the undecorated $LSCF_{113}$ and LNO_{214}-decorated $LSCF_{113}$ films are shown in Figure 20(a). Interestingly, the k^q values of the LNO_{214}-decorated $LSCF_{113}$ were found to be similar to those of the undecorated $LSCF_{113}$. As shown in Figure 20(b), LSC_{214} decoration also did not enhance the k^q of $LSCF_{113}$. It should be noted that LNO_{214} or LSC_{214} coverage led to only 1 – 2 times enhancement of the k^q values of the $LSCF_{113}$ thin films while the k^q of LSC_{113} with LSC_{214} coverage was found to be nearly 2 orders of magnitude higher than that of the undecorated LSC_{113}, as reported previously [4]. As shown in Table 2, LNO_{214} or LSC_{214} decoration had no influence on the strains of $LSCF_{113}$. In addition, different decoration materials of LNO_{214} (~4.1 nm) and LSC_{214} (~2.6 nm) resulted in similar enhancement of the surface exchange kinetics of $LSCF_{113}$. Therefore, our observation cannot be explained by the difference of Ruddlesden-Popper (RP) phase oxides and the strains at the interface. Further studies are needed to elucidate the mechanism of the surface exchange kinetics of $LSCF_{113}$ with RP phase decoration. Indeed, other possible decoration materials are needed to investigate to improve the surface activity of $LSCF_{113}$.

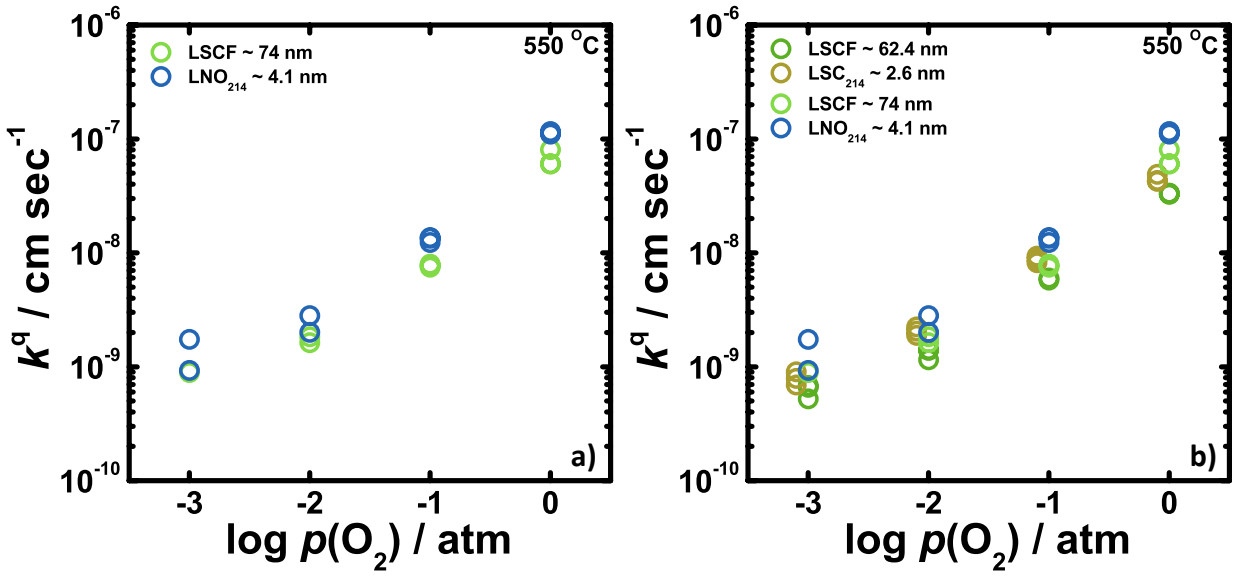

Figure 20. Oxygen partial pressure dependency of the surface exchange coefficients, k^q of (a) $LSCF_{113}$ with (light blue) and without (light green) LNO_{214} decoration thin films, and (b) $LSCF_{113}$ with (green) and without (dark yellow) LSC_{214} decoration thin films, calculated from EIS spectra collected at 550 ^{O}C.

5.5 Project V. GDC decorated LSCF films

5.5.1 Sample preparation

Pulsed laser deposition was utilized to deposit the epitaxial $LSCF_{113}$ decorated with GDC thin films on YSZ with GDC as the buffer layer with thickness ~ 5 nm. Single crystal YSZ wafers with (001) orientation and dimensions of 10 × 5 × 0.5 mm (MTI corporation, USA) were used as the substrate. Prior to $LSCF_{113}$ and GDC deposition, platinum ink (Pt) (#6082, BASF, USA) counter electrodes were painted on one side of the YSZ and dried at 900 ºC in air for 1 hour. The YSZ wafer was affixed to the PLD substrate holder using a small amount of silver paint (Leitsilber 200, Ted Pella, USA) for thermal contact. PLD was performed using a KrF excimer laser at λ = 248 nm, 10 Hz pulse rate and 50 mJ pulse energy under an oxygen partial pressure, $p(O_2)$ of 6.6 × 10^{-5} atm (50 mTorr) with GDC (~5 nm) at 550 °C. Then, $LSCF_{113}$ (~15,000 pulses) were deposited on GDC. A surface decoration with GDC with various thicknesses (~50, ~100, ~500, and ~10,000 pulses) was deposited subsequently on the top of $LSCF_{113}$/GDC/YSZ(001). The utilization of RHEED enabled an in-situ monitoring of the film growth. After completing the deposition, the samples were cooled down to room temperature in the PLD chamber for ~1 hour under a $p(O_2)$ of 6.6 × 10^{-5} atm (50 mTorr).

Surface morphology was examined by optical microscopy (Carl Zeiss, Germany) and AFM (Veeco, USA). As shown in Figure 21, all atomic force microscopy (AFM) images of as-deposited $LSCF_{113}$ and GDC-decorated $LSCF_{113}$ films revealed that the surfaces were smooth with the RMS roughness values of 0.24 ~ 0.34 nm.

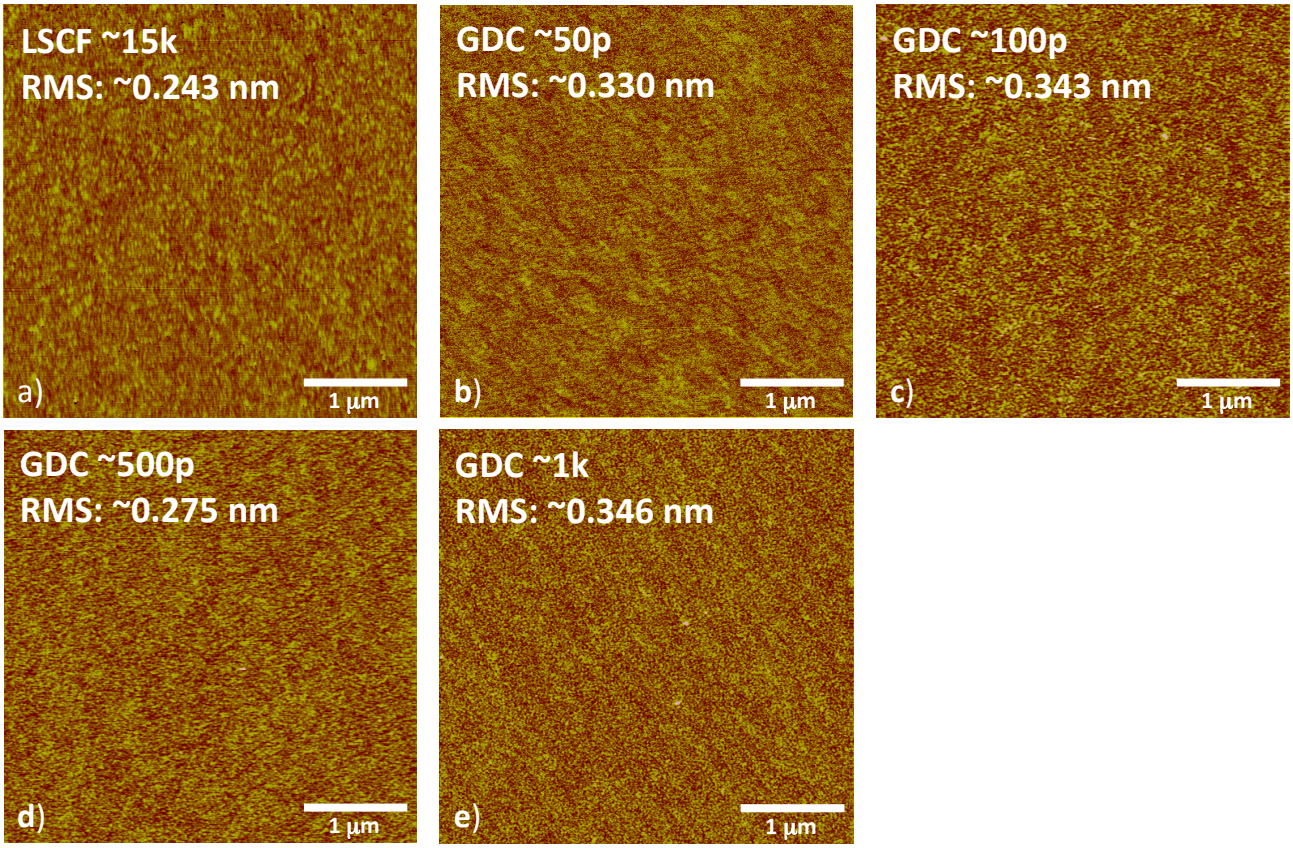

Figure 21. AFM images of (a) as-deposited bare $LSCF_{113}$ ~15,000 pulses, (b) $LSCF_{113}$ with ~50 pulses GDC, (c) $LSCF_{113}$ with ~100 pulses GDC, (d) $LSCF_{113}$ with ~500 pulses GDC, and (e) $LSCF_{113}$ with ~1,000 pulses GDC. RMS roughness values ranged from 0.24 – 0.34 nm are comparable across all surfaces.

Oxide phase purity and orientation of the thin film systems were investigated via HRXRD using a four-circle diffractometer (PANalytical, USA and Bruker D8, Germany). Measurements were performed in normal and off-normal configurations. The in-plane lattice parameters (***a*** lattice parameter) of $LSCF_{113}$ was determined from the off-normal $(202)_{pc}$ peak position (where "pc" denotes the pseudocubic notation) and the ***c*** lattice parameter of $LSCF_{113}$ normal to the film surface was determined from the $(002)_{pc}$ peak position. Normal XRD data (Figure 22(a)) of the undecorated $LSCF_{113}$ and GDC-decorated $LSCF_{113}$ films clearly show the presence of the $(00l)_{pc}$ (l is integer) peaks of $LSCF_{113}$ and $(00l)_{cubic}$ (l is even) peaks of GDC and YSZ, indicating that the GDC-decorated $LSCF_{113}$ film grew epitaxially. In Figure 22(b), off-normal phi-scan analysis of the undecorated $LSCF_{113}$ and GDC-decorated $LSCF_{113}$ films shows that GDC $\{202\}_{cubic.}$, LSC_{113} $\{202\}_{pc}$, GDC $\{202\}_{cubic}$ and YSZ $\{202\}_{cubic}$ have strong peaks with 4-fold cubic symmetry, which reveal the in-plane crystallographic relationships between GDC and YSZ (a cube-on-cube alignment), $LSCF_{113}$ and GDC (an in-plane 45º rotation with $[100]_{pc}LSCF_{113}$ // $[110]_{cubic}$GDC // $[110]_{cubic}$YSZ), and $LSCF_{113}$ and GDC (an in-plane 45º rotation with $[100]_{pc}LSCF_{113}$ // $[11o]_{cubic}$GDC), as shown in Figure 22(c).

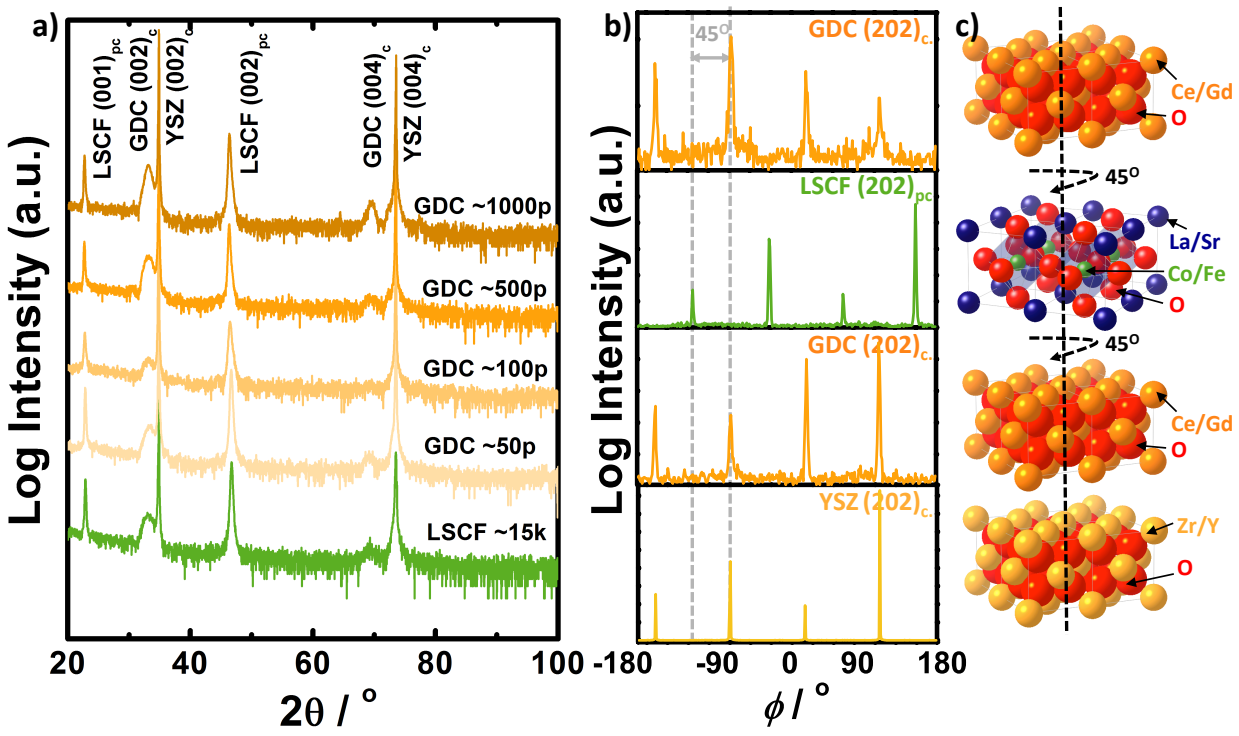

Figure 22. X-ray diffraction (Cu K_α) analysis at room temperature. (a) Normal XRD of the epitaxial $LSCF_{113}$ reference and the GDC-decorated $LSCF_{113}$ films, (b) off-normal XRD of a similarly prepared sample with a thicker (~1,000 pulses) GDC coverage, and (c) schematic of the crystallographic rotational relationships among the $GDC(001)_{cubic}$, $LSCF_{113}(001)_{pc}$, $GDC(001)_{cubic}$, and $YSZ(001)_{cubic}$.

The relaxed lattice parameters, $\hat{a}$ of the epitaxial $LSCF_{113}$ films in this study at room temperature did not change significantly with a decoration materials (GDC), as shown in Table 3. For determining the relaxed film lattice parameter $\hat{a}$ ($LSCF_{113}$), we used the equation: $\frac{(c-\hat{c})}{\hat{c}} = \frac{-2\nu}{1-\nu}\frac{(a-\hat{a})}{\hat{a}}$, assuming $\hat{a} = \hat{c}$ and $\nu = 0.25$. The in-plane strain is given by: $\varepsilon_{cc} = \frac{(c-\hat{c})}{\hat{c}}$ and the out of plane strain by: $\varepsilon_{aa} = \frac{(a-\hat{a})}{\hat{a}}$. In order to compare the lattice parameters and the lattice strains in $LSCF_{113}$ decorated with GDC, relaxed lattice parameters and lattice strains of $LSCF_{113}$ films were also extracted from normal and off-normal HRXRD data.

Table 3: Constrained and relaxed lattice parameters of $LSCF_{113}$ and GDC-decorated $LSCF_{113}$ films extracted from normal and off-normal XRD data at room temperature. Constrained normal and in-plane lattice parameters of all films were calculated from combining the inter-planar distance of the $LSCF(002)_{pc}$ and $LSCF(202)_{pc}$ peaks.

Samples	Constrained in-plane a / Å	Constrained normal c / Å	Relaxed lattice parameter $\hat{a}$ / Å	In-plane strain $\varepsilon_{aa} = \frac{(a-\hat{a})}{\hat{a}}$ / %	Normal strain $\varepsilon_{cc} = \frac{(c-\hat{a})}{\hat{a}}$ / %
LSCF ~15k	3.895	3.899	3.898	-0.073	0.049
GDC ~50p	3.901	3.904	3.903	-0.046	0.031
GDC ~100p	3.907	3.901	3.903	-0.087	-0.058
GDC ~500p	3.892	3.913	3.904	-0.032	0.022
GDC ~1k	3.898	3.910	3.905	-0.019	0.012

5.5.2 Oxygen Surface Exchange Kinetics of LSCF-113 thin films with single layer decoration of GDC

Murray *et al.*[14] have shown enhanced electrochemical performance of $LSCF_{113}$ and GDC composite materials, which may be attributed to higher ionic conductivity of GDC. However, the enhanced electrode performance produced by the GDC addition is not well understood. As shown in Figure 23(a), GDC was utilized as a decorating film on $LSCF_{113}$ thin film to enhance the surface exchange kinetics of the $LSCF_{113}$. Interestingly, the k^q values of the $LSCF_{113}$ were found to significantly increase (~1.3 orders of magnitude) with a GDC decoration. However, only GDC 400p showed a dramatic enhancement of the k^q of $LSCF_{113}$ (Figure 23(b)). This may result from an ability of GDC to enhance the oxygen transport related to the surface activity of $LSCF_{113}$. It may also enhance the stability due to an increase in solubility of SrO, which can hamper the surface exchange kinetics. Further studies are required to understand the origin of the enhancement with GDC and verify the thickness-dependent k^q of $LSCF_{113}$ thin films.

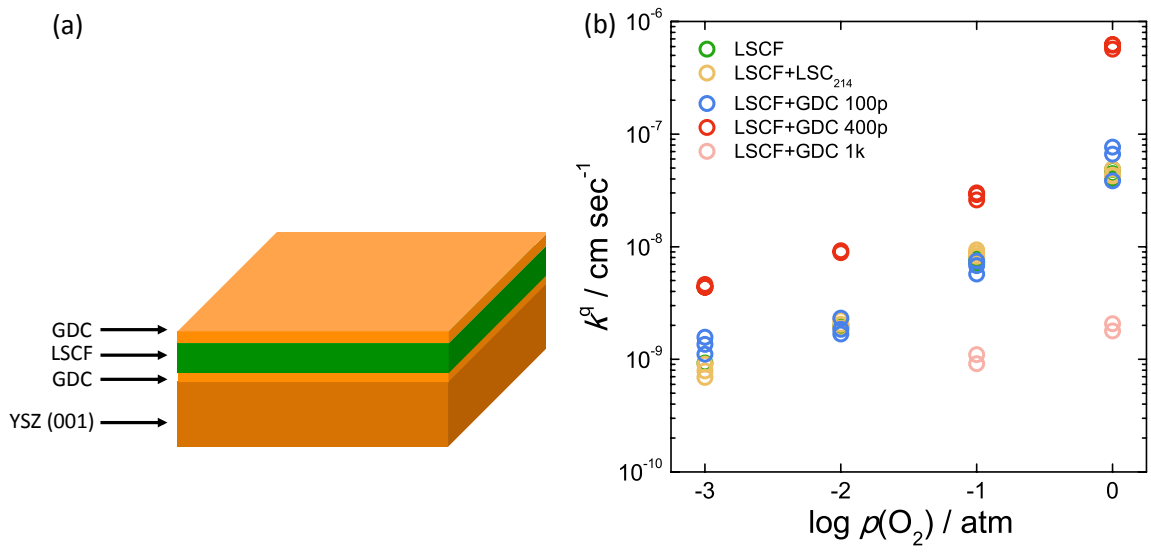

Figure 23. (a) Schematic of the $LSCF_{113}$ thin films with GDC decoration, and (b) oxygen partial pressure dependency of the surface exchange coefficients (k^q) of the $LSCF_{113}$, LSC_{214}-decorated $LSCF_{113}$, and GDC-decorated $LSCF_{113}$ thin films calculated from EIS spectra collected at 550 ^{O}C.

5.6 Project VI. $(La_{1-x}Sr_x)_2CuO_{4\pm\delta}$ surface decoration effect

5.6.1 Film deposition and characterizations

Pulsed laser deposition was utilized to deposit the epitaxial $(La_{1-x}Sr_x)_2CuO_{4\pm\delta}$ (x= 0, 0.15, and 0.4) thin films on YSZ with GDC as the buffer layer with thickness ~ 5 nm. Single crystal YSZ wafers with (001) orientation and dimensions of 10 × 5 × 0.5 mm (MTI corporation, USA) were used as the substrate. Prior to $(La_{1-x}Sr_x)_2CuO_{4\pm\delta}$ deposition, platinum ink (Pt) (#6082, BASF, USA) counter electrodes were painted on one side of the YSZ and dried at 900 ºC in air for 1 hour. The YSZ wafer was affixed to the PLD substrate holder using a small amount of silver paint (Leitsilber 200, Ted Pella, USA) for thermal contact. PLD was performed using a KrF excimer laser at λ = 248 nm, 10 Hz pulse rate and 50 mJ pulse energy under an oxygen partial pressure, $p(O_2)$ of 6.6 × 10^{-5} atm (50 mTorr) with GDC (~5 nm) at 600 °C. Then, both $(La_{1-x}Sr_x)_2CuO_{4\pm\delta}$ (~10,000 pulses) were deposited on GDC. After completing the deposition, the samples were cooled down to room temperature in the PLD chamber for ~1 hour under a $p(O_2)$ of 6.6 × 10^{-5} atm (50 mTorr). The oxide phase purity and the thin film orientations were investigated via high-resolution X-ray diffraction (HRXRD) using a four-circle diffractometer (PANalytical, USA). Recently, Lee *et al.* [15] has reported that the $(La_{1-x}Sr_x)_2NiO_{4\pm\delta}$ (LSNO) film orientation can be changed gradually from the $(100)_{tetra.}$ (in-plane) to the $(001)_{tetra.}$ (out-of-plane) orientation in the RP structure with increasing Sr contents via high resolution X-ray diffraction. It is noted that the orientation of the $(La_{1-x}Sr_x)_2CuO_{4\pm\delta}$ thin films showed $(001)_{tetra.}$ (out-of-plane) orientation regardless of Sr content.

5.6.2 Surface Exchange Kinetics of $(La_{1-x}Sr_x)_2CuO_{4\pm\delta}$ thin films

5.6.2.1 Electrochemical Impedance Spectroscopy

EIS data of all samples used in this study were found to be very similar in shape, and typical features in the Nyquist plots are shown in the schematic in Figure 24(c). Figure 24(b) details the equivalent circuit and corresponding Nyquist plot for this experimental system. The EIS data were fitted using a standard resistor (R_1) for *HF* and resistors (R_2) in parallel with CPE_2 for *MF* and *LF* (R_1-(R_2/CPE_2)-(R_{ORR}/CPE_{ORR})). Based on the $p(O_2)$ dependence of the three features, physical or chemical process with regard to each frequency range can be determined. The *HF* feature (10^4 – 10^5 Hz) was found unchanged with $p(O_2)$, and its magnitude and activation energy (~1.15 eV) were comparable to those of oxygen ion conduction in YSZ reported previously [12]. The *MF* feature (10^3 – 10^4 Hz), which was found to have a $p(O_2)$ independent feature, was attributed to interfacial transport of oxygen ions between the $(La_{1-x}Sr_x)_2CuO_{4\pm\delta}$ film and the GDC layer. In addition, the magnitude of its capacitance was relatively small (~10^{-6} F) compared to the *LF* feature (~10^{-3} F). The *LF* feature (10^{-2} – 10^3 Hz) was found to have a strong $p(O_2)$ dependence. The resistance of the *LF* feature drastically increases as oxygen partial pressure decreases. In the case of thin film samples, the magnitude of capacitance is due to the oxygen content change in the films. Therefore, the electrode oxygen surface reaction corresponds with the *LF* feature. We obtained values for R_{ORR}; and knowing the area of the microelectrode ($A_{electrode} = 0.25\ \pi\ d_{electrode}^2$) we can determine the ORR area specific resistance ($ASR_{ORR} = R_{ORR} \cdot A_{electrode}$). The electrical surface exchange coefficient (k^q), which is comparable to k^* [13] was determined using the expression,

$$k^q = RT / 4F^2 R_{ORR} A_{electrode} c_o \qquad \textbf{Eqn. 3}$$

where R is the universal gas constant (8.314 J mol^{-1} K^{-1}), T is the absolute temperature, F is the Faraday's constant (96,500 C mol^{-1}), and c_o is the lattice oxygen concentration in $(La_{1-x}Sr_x)_2CuO_{4\pm\delta}$,

$$c_o = (4\pm\delta)/V_m \qquad \textbf{Eqn. 4}$$

where V_m is the molar volume of $(La_{1-x}Sr_x)_2CuO_{4\pm\delta}$ at room temperature. In this study, c_o was calculated with δ extracted from previous reported values.

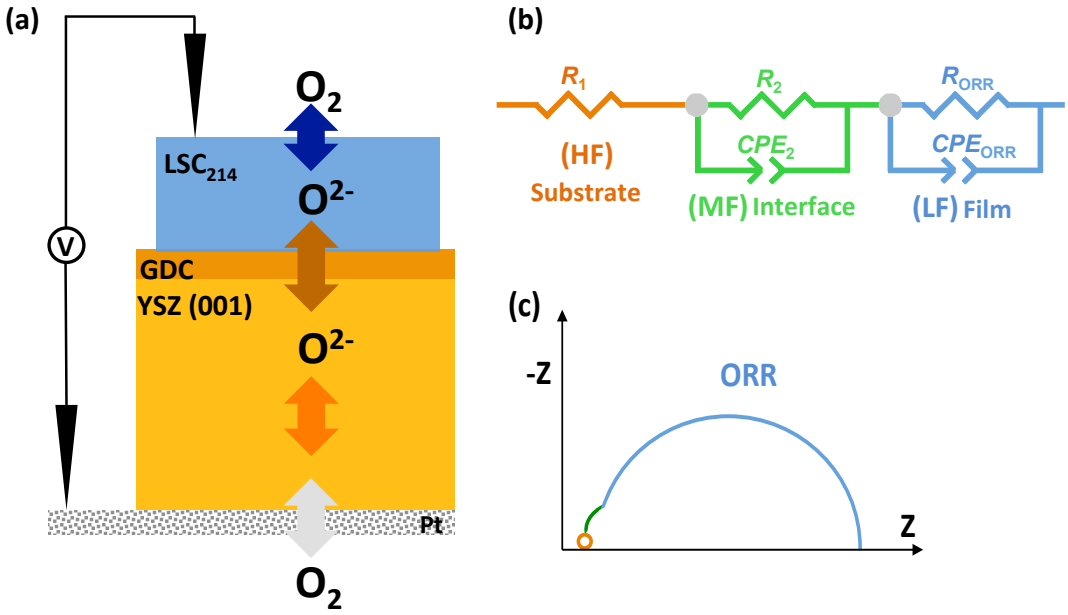

Figure 24. (a) Schematic of a $(La_{1-x}Sr_x)_2CuO_{4\pm\delta}$/GDC/YSZ(001)/porous Pt sample and electrochemical testing configuration (not drawn to scale; dimensions provided in the Experimental Methods), (b) equivalent circuit (R_1 = YSZ electrolyte resistance, R_2 = electrode/electrolyte interface resistance, R_{ORR} = ORR resistance, CPE = constant phase element) used to extract ORR kinetics, and (c) characteristic Nyquist plot schematic (color key: red = YSZ/bulk transport, green = GDC/interface, blue = LSC_{214}/ORR).

5.6.2.2 Surface Exchange Kinetics of $(La_{1-x}Sr_x)_2CuO_{4\pm\delta}$ thin films

Representative oxygen surface exchange coefficient (k^q) values of the $(La_{1-x}Sr_x)_2CuO_{4\pm\delta}$ thin films as a function of the Sr content obtained at $p(O_2)$ = 1 atm and T = 550 °C are shown in Figure 25. Interestingly, the k^q values of the $La_2CuO_{4\pm\delta}$ (Sr=0) were found to be an order of magnitude higher than those of $La_{1.85}Sr_{0.15}CuO_{4\pm\delta}$ and $La_{1.6}Sr_{0.4}CuO_{4\pm\delta}$ thin films. However, the k^q values of $La_{1.85}Sr_{0.15}CuO_{4\pm\delta}$ films were found to be comparable with those of $La_{1.6}Sr_{0.4}CuO_{4\pm\delta}$ films. It has been shown that the k^q values of LSNO thin films can be strongly influenced by Sr content [15]. The k^q values of the $\boldsymbol{a}_{tetra.}$-axis-oriented LNO (x_{Sr} = 0.0) are two orders of magnitude higher than those of the $\boldsymbol{c}_{tetra.}$-axis-oriented LSNO (x_{Sr} = 1.0), where the k^q values of the LSNO thin films decreased with increasing orientation having the $\boldsymbol{c}_{tetra.}$-axis perpendicular to the film surface with increasing Sr. In the case of $(La_{1-x}Sr_x)_2CuO_{4\pm\delta}$ thin films, however, the film orientation was not changed by adding Sr content. Therefore, our observation cannot be explained by the orientation change observed in LSNO system.

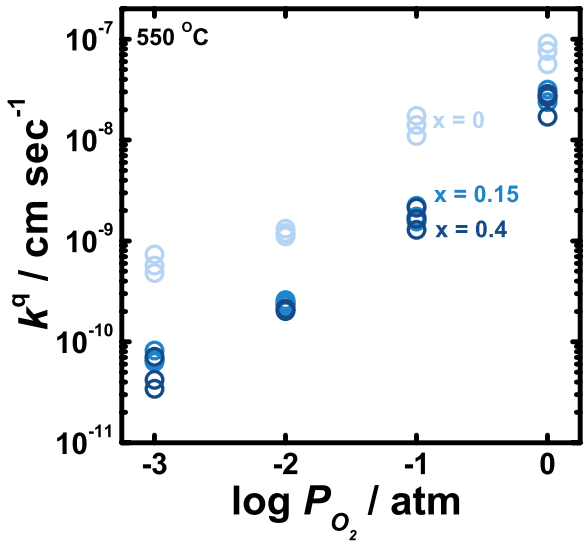

Figure 25. Oxygen partial pressure dependency of the surface exchange coefficients, k^q of (a) $La_2CuO_{4\pm\delta}$ (light blue), $La_{1.85}Sr_{0.15}CuO_{4\pm\delta}$ (blue) and $La_{1.6}Sr_{0.4}CuO_{4\pm\delta}$ (dark blue) thin films, and (b) $LSCF_{113}$ with (green) and without (dark yellow) LSC_{214} decoration thin films, calculated from EIS spectra collected at 550 ^{O}C.

Figure 26 shows the surface exchange kinetics of Ruddlesden-Popper (RP) thin films as a function of Sr content. All RP thin films are c-axis oriented films and therefore the orientation effect on the surface exchange kinetics can be ruled out. The k^q values of RP thin films were found to decrease with increasing Sr content except $LaSrCoO_{4\pm\delta}$ thin films. In the case of ABO_3 perovskite oxides, such as $La_{1-x}Sr_xCoO_{3-\delta}$ and $Sm_{1-x}Sr_xCoO_{3-\delta}$, the surface exchange kinetics can be enhanced by increasing Sr content, where increased number of oxygen vacancies induced by more Sr may be responsible for the enhancement of the surface exchange kinetics.[16, 17] In contrast to ABO_3 oxides, RP thin films show the opposite trend, although more Sr can increase more oxygen vacancies. This is perhaps due to the dominance of interstitials in the RP surface exchange mechanisms. Further studies are needed to elucidate the influence of the Sr on the surface exchange kinetics of RP phase.

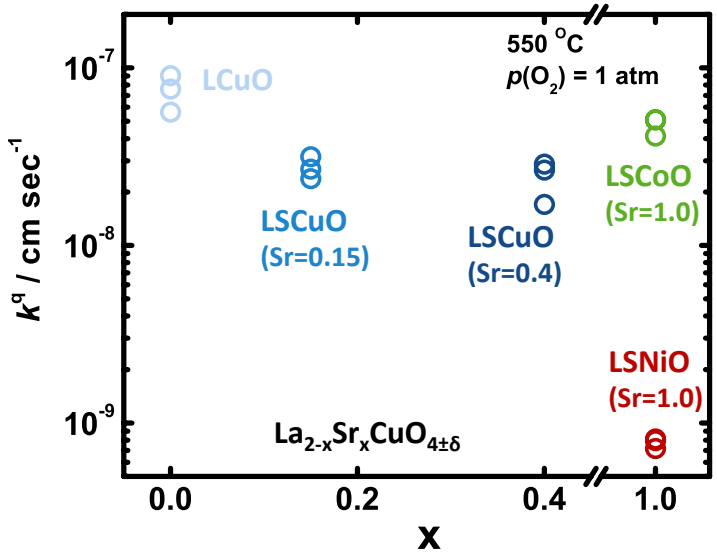

Figure 26. Surface exchange coefficients, k^q of A_2BO_4 thin films as a function of Sr contents, calculated from EIS spectra collected at 550 ^{O}C.

5.7 Surface Activity Enhancement by composite decoration films

This part we focused on the Sr influence on the surface exchange kinetics in A_2BO_4 thin films, such as $(La_{1-x}Sr_x)_2CoO_{4\pm\delta}$, making varied Sr content LSC_{214} on LSC_{113} films.

5.7.1 Film deposition

Pulsed laser deposition was utilized to deposit the epitaxial $LSCF_{113}$ decorated with LSC_{214} and $La_{1-x}Sr_xCoO_{3-\delta}$ (LSC_{113}, x= 0.2, 0.4, and 0.6) thin films on YSZ with GDC as the buffer layer with thickness ~ 5 nm. Single crystal YSZ wafers with (001) orientation and dimensions of 10 × 5 × 0.5 mm (MTI corporation, USA) were used as the substrate. Prior to $LSCF_{113}$ and GDC deposition, platinum ink (Pt) (#6082, BASF, USA) counter electrodes were painted on one side of the YSZ and dried at 900 ºC in air for 1 hour. The YSZ wafer was affixed to the PLD substrate holder using a small amount of silver paint (Leitsilber 200, Ted Pella, USA) for thermal contact. PLD was performed using a KrF excimer laser at λ = 248 nm, 10 Hz pulse rate and 50 mJ pulse energy under an oxygen partial pressure, $p(O_2)$ of 6.6 × 10^{-5} atm (50 mTorr) with GDC (~5 nm) at 550 °C. Then, $LSCF_{113}$ (~15,000 pulses) were deposited on GDC. A surface decoration with LSC_{214} and LSC_{113} was deposited on the top of $LSCF_{113}$/GDC/YSZ(001). First, LSC_{214} ~2 pulses were applied, and then LSC_{113} ~2 pulses were deposited. In order to deposit ~400 pulses composite decoration films, a total number of ~100 pulses was performed for each material. The utilization of RHEED enabled an in-situ monitoring of the film growth. After completing the deposition, the samples were cooled down to room temperature in the PLD chamber for ~1 hour under a $p(O_2)$ of 6.6 × 10^{-5} atm (50 mTorr).

Surface morphology was examined by optical microscopy (Carl Zeiss, Germany) and AFM (Veeco, USA). As shown in Figure 27, all atomic force microscopy (AFM) images of as-deposited $LSCF_{113}$ and LSC_{214}-LSC_{113}-decorated $LSCF_{113}$ films revealed that the surfaces were smooth with the root-mean-square (RMS) roughness values of 0.21 ~ 0.37 nm.

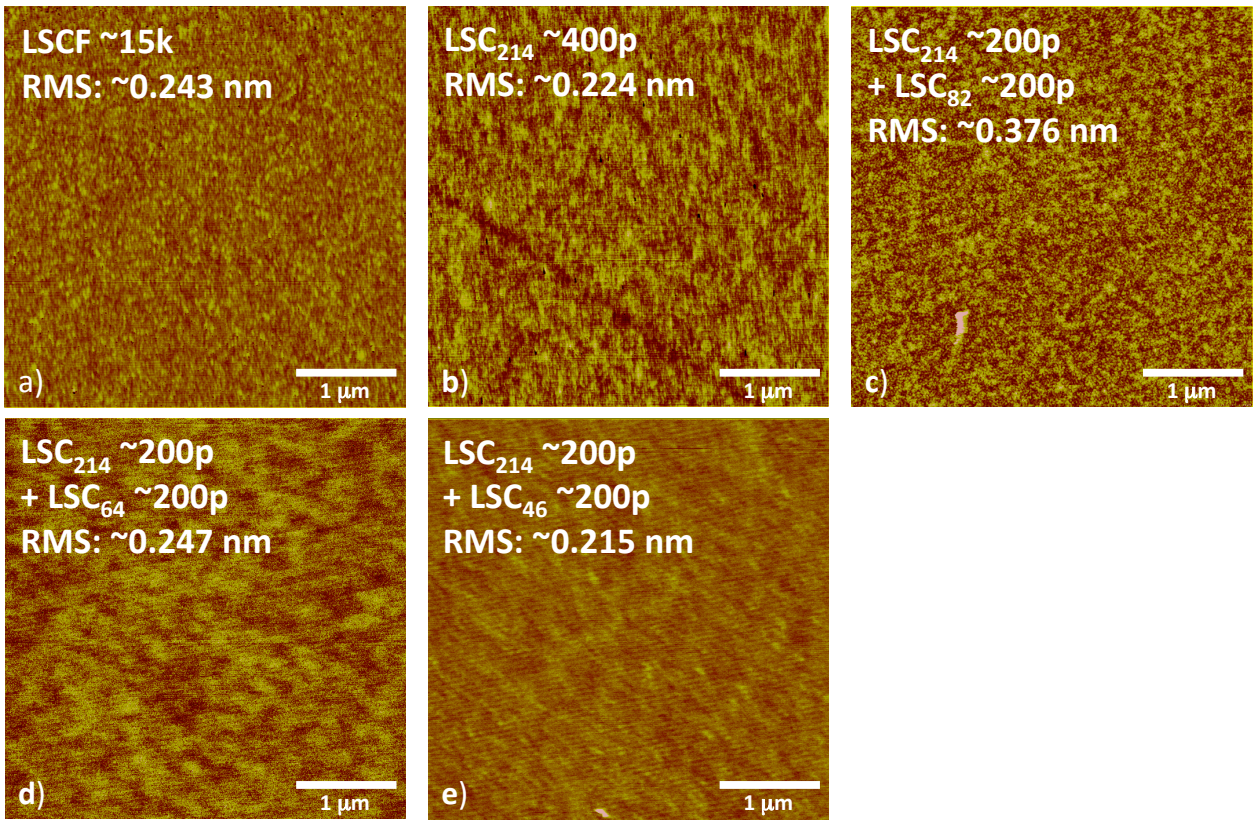

Figure 27. AFM images of (a) as-deposited bare $LSCF_{113}$ ~15,000 pulses, (b) $LSCF_{113}$ with ~400 pulses LSC_{214}, (c) $LSCF_{113}$ with ~200 pulses LSC_{214} and ~200 pulses LSC_{113} (Sr=20%), (d) $LSCF_{113}$ with ~200 pulses LSC_{214} and ~200 pulses LSC_{113} (Sr=40%), and (e) $LSCF_{113}$ with ~200 pulses LSC_{214} and ~200 pulses LSC_{113} (Sr=60%). RMS roughness values ranged from 0.21 – 0.37 nm are comparable across all surfaces.

Oxide phase purity and orientation of the thin film systems were investigated HRXRD using a four-circle diffractometer (PANalytical, USA and Bruker D8, Germany). Measurements were performed in normal and off-normal configurations. The in-plane lattice parameters (***a*** lattice parameter) of $LSCF_{113}$ was determined from the off-normal $(202)_{pc}$ peak position (where "pc" denotes the pseudocubic notation) and the ***c*** lattice parameter of $LSCF_{113}$ normal to the film surface was determined from the $(002)_{pc}$ peak position. Normal XRD data (Figure 28(a)) of the undecorated $LSCF_{113}$ and LSC_{214}-LSC_{113}-decorated $LSCF_{113}$ films clearly show the presence of the $(00l)_{pc}$ (l is integer) peaks of $LSCF_{113}$ and $(00l)_{cubic}$ (l is even) peaks of GDC and YSZ, indicating that the LSC_{214}-LSC_{113}-decroated $LSCF_{113}$ film grew epitaxially.

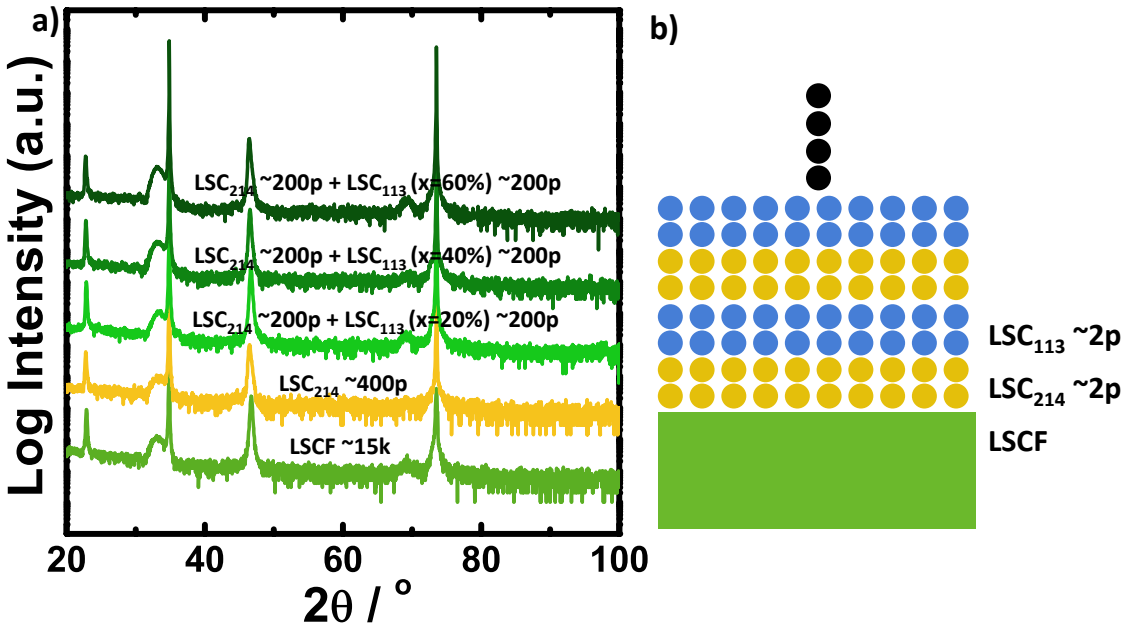

Figure 28. X-ray diffraction (Cu K_α) analysis at room temperature. (a) Normal XRD of the epitaxial $LSCF_{113}$ reference and the LSC_{214}-LSC_{113}-decorated $LSCF_{113}$ films, and (b) the schematic of the $LSCF_{113}$ thin film with composite decoration films.

The relaxed lattice parameters, $\hat{a}$ of the epitaxial $LSCF_{113}$ films in this study at room temperature did not change significantly with a decoration materials (GDC), as shown in Table 4. For determining the relaxed film lattice parameter $\hat{a}$ ($LSCF_{113}$), we used the equation: $\frac{(c-\hat{c})}{\hat{c}} = \frac{-2\nu}{1-\nu}\frac{(a-\hat{a})}{\hat{a}}$, assuming $\hat{a} = \hat{c}$ and $\nu = 0.25$. The in-plane strain is given by: $\varepsilon_{cc} = \frac{(c-\hat{c})}{\hat{c}}$ and the out of plane strain by: $\varepsilon_{aa} = \frac{(a-\hat{a})}{\hat{a}}$. In order to compare the lattice parameters and the lattice strains in $LSCF_{113}$ decorated with LSC_{214}-LSC_{113} composition, relaxed lattice parameters and lattice strains of $LSCF_{113}$ films were also extracted from normal and off-normal HRXRD data.

Table 4: Constrained and relaxed lattice parameters of $LSCF_{113}$ and GDC-decorated $LSCF_{113}$ films extracted from normal and off-normal XRD data at room temperature. Constrained normal and in-plane lattice parameters of all films were calculated from combining the inter-planar distance of the $LSCF(002)_{pc}$ and $LSCF(202)_{pc}$ peaks.

Samples	Constrained in-plane a / Å	Constrained normal c / Å	Relaxed lattice parameter $\hat{a}$ / Å	In-plane strain $\varepsilon_{aa} = \frac{(a-\hat{a})}{\hat{a}}$ / %	Normal strain $\varepsilon_{cc} = \frac{(c-\hat{a})}{\hat{a}}$ / %
LSCF ~15k	3.895	3.899	3.898	-0.073	0.049
LSC_{214} ~400p	3.897	3.903	3.900	-0.077	0.051
LSC_{214} ~200p LSC_{82} ~200p	3.899	3.888	3.893	0.017	-0.012
LSC_{214} ~200p LSC_{64} ~200p	3.893	3.898	3.896	-0.068	0.045
LSC_{214} ~200p LSC_{46} ~200p	3.891	3.906	3.900	-0.024	0.016

5.7.2 Surface Decoration Effect on the Surface Stability of ABO3 Oxides

Our recent study using Coherent Brag Rod Analysis (COBRA) has revealed the atomic structure and concentrations of the (001)-oriented LSC_{113} thin film on a $SrTiO_3$ (STO) substrate, which shows strontium (Sr) segregation toward the LSC_{113} surface and Sr depletion near the interface between LSC_{113} and STO[18]. More recently, COBRA has also revealed the markedly enhanced Sr concentration at the interface of LSC_{113} and LSC_{214} and near the surface of LSC_{214}, proposing that the increased Sr content at the interface may contribute the enhanced catalytic activity resulting in higher oxygen vacancy concentration. In addition, heating the (001)-oriented LSC_{113} surface leads to the formation of surface Sr-enriched particles upon annealing while the LSC_{214}-decorated LSC_{113} surface chemistry is stable upon heating[10]. These observations have suggested that the surface decoration can modulate the surface Sr segregation and the surface phase stability, which can greatly influence the oxygen surface exchange kinetics and the surface stability in LSC_{113} and $LSCF_{113}$.

5.7.2.1 Surface Stability of LSC113 and LSCF113 with Surface Decoration

Figure 29 shows the surface stability change of LSC_{113} reference, LSM_{113}/LSC_{113}, LSC_{214}/LSC_{113}, $LSCF_{113}$ reference, and $LSC_{214}/LSCF_{113}$ thin films before and after annealing at 550 °C for 6 hours in pure oxygen flow. In the case of LSC_{113} reference, discrete particles were noted on the LSC_{113} surface after annealing (Figure 29(c)). The intensity of Sr cation spectra from AES was found to significantly increase after annealing (Figure 29(a)). In contrast, no particles were found on the as-deposited LSC_{113} surface (Figure 29(b)), which had a Sr cation spectra comparable to the LSC_{113} pristine sample. It should be noted that the LSC_{214} decorated LSC_{113} thin film was found to have no particle formation after annealing (Figure 29(i)). AES data also support that the Sr cation spectra did not change before and after annealing. This can be interpreted that the LSC_{214} decoration can lead to stabilization of the LSC_{113} surface after annealing, which can result in significantly enhanced surface activity with LSC_{214} decoration. In addition, $La_{0.8}Sr_{0.2}MnO_{3-\delta}$ (LSM_{113}) decoration can also lead to the stable surface of LSC_{113} after heat treatment, as shown in Figure 29(f). AES data also showed similar Sr cation spectra as LSC_{214} decorated LSC_{113} showed. (Figure 29(d)). This represents that the LSC_{113} surface can be stabilized by not only LSC_{214} but also LSM_{113}, which has the same perovskite structure. Moreover, it is expected that LSM_{113} decoration may also enhance the surface exchange kinetics of LSC_{113}.

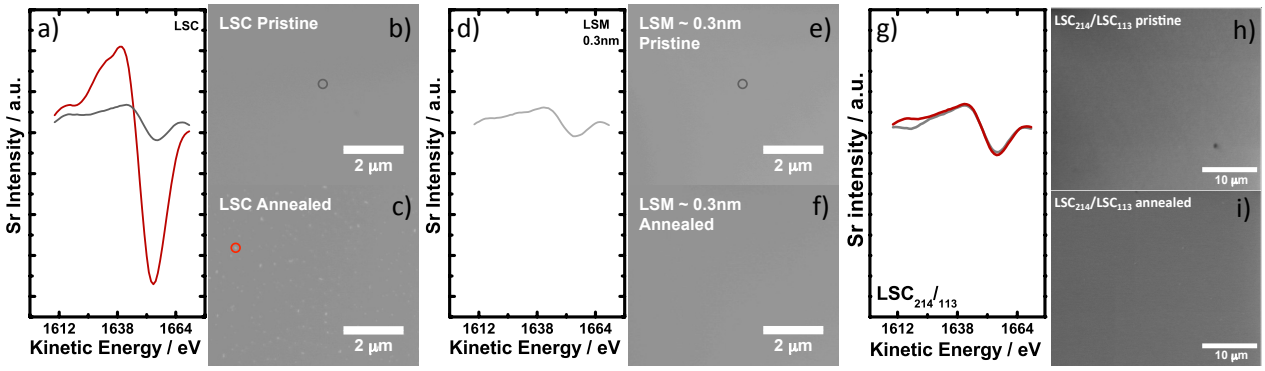

Figure 29. Auger electron spectroscopy (AES) Sr cation spectra of (a) LSC_{113} before and after annealing, (d) LSM_{113}/LSC_{113} before and after annealing, (g) LSC_{214}/LSC_{113} before and after annealing, and SEM images of LSC_{113} before (b) and after (c) annealing, LSM_{113}/LSC_{113} before (e) and after (f) annealing, and LSC_{214}/LSC_{113} before (h) and after (i) annealing. All annealing conditions were at 550 °C for 6 hours in pure oxygen flow.

However, $LSCF_{113}$ thin film showed no significant change in surface morphology after annealing (Figure 30(b) and (c)). Indeed, the intensity of Sr cation spectra for $LSCF_{113}$ thin films was found to have no significant change before and after annealing (Figure 30(a)). This indicates that $LSCF_{113}$ thin film is more stable than LSC_{113} thin film. LSC_{214} decoration on $LSCF_{113}$ was found to be no change in the surface morphology and the surface chemistry of $LSCF_{113}$ (Figure 30(e) and (f)), which can be considered as the reason for relatively small enhancement of the $LSCF_{113}$ surface activity.

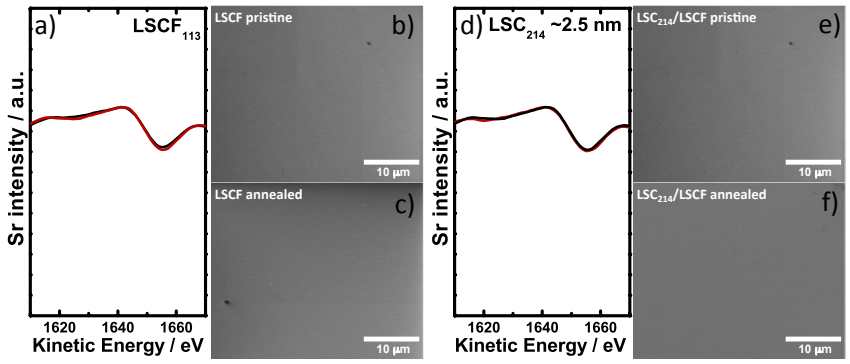

Figure 30. Auger electron spectroscopy (AES) Sr cation spectra of (a) $LSCF_{113}$ before and after annealing, (d) LSC_{214}/LSC_{113} before and after annealing, and SEM images of $LSCF_{113}$ before (b) and after (c) annealing, and LSC_{214}/LSC_{113} before (e) and after (f) annealing. All annealing conditions were at 550 °C for 6 hours in pure oxygen flow.

5.7.2.2 LSCF-113 thin films with single-layer decoration of mixed LSC-214 and LSC-113

Electrochemical impedance spectroscopy measurements of microelectrodes ~ 200 µm in diameter were performed using a microprobe station (Karl Süss, Germany) connected to a frequency response analyzer (Solartron 1260, USA) and dielectric interface (Solartron 1296, USA). Temperature was controlled at 550 ° C with heating stage (Linkam TS1500, UK), and data were collected between 1 MHz and 1 mHz using a voltage amplitude of 10 mV. EIS testing temperature was calibrated with a thermocouple contacting the thin film surface, and deviation of ± 5 °C was observed. EIS experiments were completed between $p(O_2)$ of 10^{-3} and 1 atm. EIS data were analyzed using an equivalent circuit, from which the ORR resistance (R_{ORR}) and surface oxygen exchange rate were obtained. EIS data of all samples used in this study were found to be very similar in semicircle shape.

Figure 31(a) shows the schematic of the $LSCF_{113}$ thin films with single-layer decoration of mixed LSC_{214} and LSC_{113}. Recently, we have shown that LSC_{214} decoration on the (001)-oriented $LSCF_{113}$ thin films does not greatly enhance the surface oxygen exchange kinetics, where a thermodynamic driving force for Sr interdiffusion from $LSCF_{113}$ to LSC_{214} is lower relative to that from LSC_{113} to LSC_{214}.[19] To increase the Sr content in the decoration of LSC_{214}, the mixture of LSC_{214} and

LSC_{113} was introduced with the same LSC_{214} and LSC_{113} ratio. Representative EIS data collected from the $LSCF_{113}$ film with single-layer decoration of mixed LSC_{214} and LSC_{113}, LSC_{214}, and LSC_{113} measured from ~200 mm microelectrodes at 550 °C as a function of $p(O_2)$ are shown in Figure 31(b). Considering the fact that the film thicknesses are much smaller than the critical thickness for bulk transport limitation (estimated to 3.28 mm for the bulk $LSCF_{113}$ at 550 °C[20], the oxygen reduction reaction (ORR) kinetics are limited by surface oxygen exchange but not by oxygen ion diffusion. The oxygen surface exchange coefficient (k^q) of $LSCF_{113}$ was found to be similar to that of LSC_{214}-decorated $LSCF_{113}$, which is in good agreement with our previous results. Interestingly, the k^q values of the $LSCF_{113}$ thin films with single-layer decoration of mixed LSC_{214} and LSC_{113} was found to be ~7 times higher than those of the LSC_{214}-decorated $LSCF_{113}$, which may be attributed to the higher Sr content in the mixture of LSC_{214} and LSC_{113}.

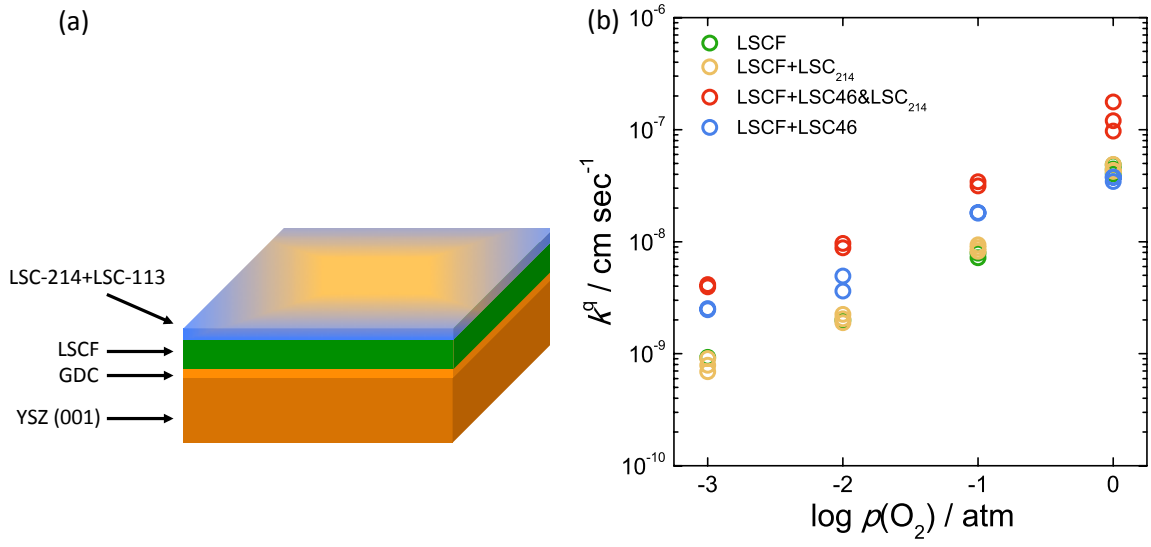

Figure 31. (a) Schematic of the $LSCF_{113}$ thin films with single-layer decoration of mixed LSC_{214} and LSC_{113}, and (b) oxygen partial pressure dependency of the surface exchange coefficients (k^q) of the $LSCF_{113}$, LSC_{113} and LSC_{214}-decorated $LSCF_{113}$, and mixed LSC_{214} and LSC_{113}-decorated $LSCF_{113}$ films calculated from EIS spectra collected at 550 ^{O}C.

5.7.2.3 Oxygen Surface Exchange Kinetics of $LSCF_{113}$ thin films with double-layer decoration of stacked LSC_{214} and LSC_{113}

To synthesize the double-layer decoration of stacked LSC_{214} and LSC_{113}, first, LSC_{113} (Sr= 0.2, 0.4, and 0.6) 50 pulses were applied, and then LSC 1k pulses were deposited in contrast to a single layer decoration of mixed LSC_{214} and LSC_{113}, as shown in Figure 32(a). Figure 32(b) represents the k^q values of the $LSCF_{113}$, LSC_{214}-decorated $LSCF_{113}$, and $LSCF_{113}$ with double-layer decoration. The double-layers of LSC_{214} and LSC_{113} with Sr= 0.2 and 0.4 were not found to change the k^q of $LSCF_{113}$. However, the double-layer decoration of LSC_{214} and LSC_{113} with Sr= 0.4 led to ~1.5 orders of magnitude enhancement of the surface exchange kinetics of the $LSCF_{113}$. It is hypothesized that the interface between higher Sr content LSC_{113} and LSC_{214} can lead to higher thermodynamic driving force to move a Sr into LSC_{214}, and thus results in higher surface exchange kinetics. Further density functional theory (DFT) study is needed to investigate the difference in the

thermodynamic driving force as a function of Sr content. Indeed, long-term stability also needs to be investigated as higher Sr content can cause lower stability.

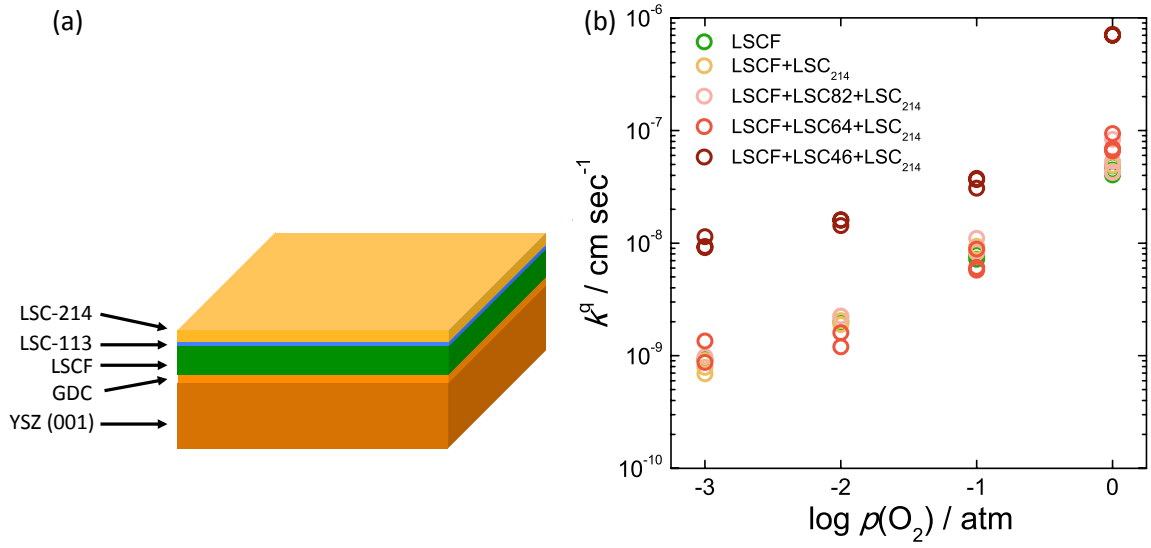

Figure 32. (a) Schematic of the $LSCF_{113}$ thin films with double-layer decoration of stacked LSC_{214} and LSC_{113}, and (b) oxygen partial pressure dependency of the surface exchange coefficients (k^q) of the $LSCF_{113}$, LSC_{214}-decorated $LSCF_{113}$, and double-layer decoration of stacked LSC_{214} and LSC_{113} (Sr= 0.2, 0.4, 0.6) thin films calculated from EIS spectra collected at 550 ^{O}C.

6 Thrust 2: Linear and Non-Linear Impedance Spectroscopy and Elementary Kinetics Modeling of Cathodes

6.1 Impedance Measurements on Thin-Film LSCF-6428

6.1.1 Theory

Interpretation of thin-film impedance measurements requires a model describing the thermodynamic relationship between bulk lattice defects and the surrounding oxygen environment, described by the half-cell reaction below, and how the surface reaction rate scales with these defects.

$$\frac{1}{2}\mathrm{O}_2(g) + V_O^{\bullet\bullet} + 2\mathrm{e}' \rightleftharpoons O_O^x$$

Eqn. 5

Independent thermogravimetry and coulometric titration measurements of bulk, non-thin-film $La_{0.6}Sr_{0.4}Co_{0.2}Fe_{0.8}O_{3-\delta}$ (LSCF-6428) provide the foundation for this thermodynamic relationship. In the limit of high iron content (>0.6), workers typically interpret the measured δ-p_{O2} relationship using a p-type point-defect model, where electrons are localized on iron centers and defects are considered dilute[21].

Figure 33 compares oxygen stoichiometry data collected by Kuhn *et al.* to the best fits for metallic and p-type models. At $p_{O2} < 10^{-4}$, the p-type model yields better agreement, yet neither perfectly captures both the slope and magnitude at the oxidizing conditions of interest ($p_{O2} > 10^{-3}$, 500-700°C). Due to the sensitivity of NLEIS to these features, we instead adopt an empirical relationship between δ and p_{O2}.

$$\ln[\delta] = -c_1 - c_2\ln[f_{O2}] - c_3\ln[f_{O2}]^2$$

Eqn. 6

$$c_j(T) = c_{j0}Exp[\frac{e_j}{T(K)}]$$

Eqn. 7

The parameters, c_j, are fit to Kuhn's measurements at 600-800°C assuming an Arrhenius temperature dependence. Figure 33 shows the best fits of the empirical model.

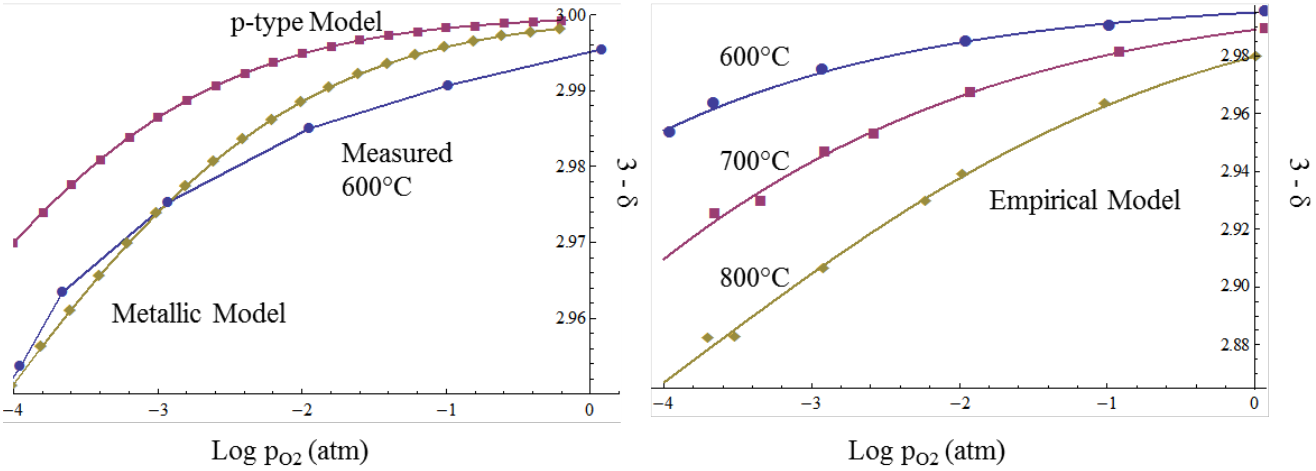

Figure 33. Comparison of Kuhn *et al's* TGA data to (left) p-type and metallic models, and (right) the empirical thermodynamic model used in this work[21].

This relationship between defect chemistry and p_{O2}/temperature allows the prediction of the volume-specific capacitance (VSC, F/cm^3) for thin films of the oxide with molar volume V_m [2].

$$VSC = \frac{8\,F^2}{R\,T\,V_m}\delta_0(c_2 + 2c_3\ln[p_{O2}])$$

Eqn. 8

For the surface kinetics, we assume a forward equilibrium exchange rate that scales with $p_{O2}\delta^n$, where n is a fitting parameter assumed independent of temperature and p_{O2}. A material balance of oxygen vacancies in the thin film using the empirical thermodynamic model above along with the surface rate law and Faraday's law as boundary conditions establishes the current-voltage relationship for an impedance experiment, allowing modeling of the linear and nonlinear impedance spectra with a single adjustable parameter, n. This model assumes a film with uniform thermodynamic behavior dictated by the independent measurements summarized in Figure 33.

6.1.2 Experimental

In October 2014, we collected linear and nonlinear electrochemical impedance spectroscopy (EIS, NLEIS) data at the Shao-Horn Lab (MIT) for undecorated epitaxial $La_{0.6}Sr_{0.4}Co_{0.2}Fe_{0.8}O_{3-\delta}$ (LSCF) thin film microelectrodes. The impedance test setup, shown in Figure 34, consisted of multiple arrays of LSCF microelectrodes of varying diameter (50 to 200 µm) deposited on a protective GDC interlayer. The cells were exposed to 1%, 10%, and 100% O_2 (bal. Ar) and temperatures between 550 and 650°C. Both bare and Pt-coated tungsten carbide tips were used as current collectors, showing no differences in electrochemical response. Current collector contact was observed as a lateral tip deflection using an optical microscope. All presented data originate from a single 200 µm diameter microelectrode on a single cell with a 20 nm electrode thickness (~5k pulses) at 600°C and a bare tungsten carbide current collector unless otherwise stated.

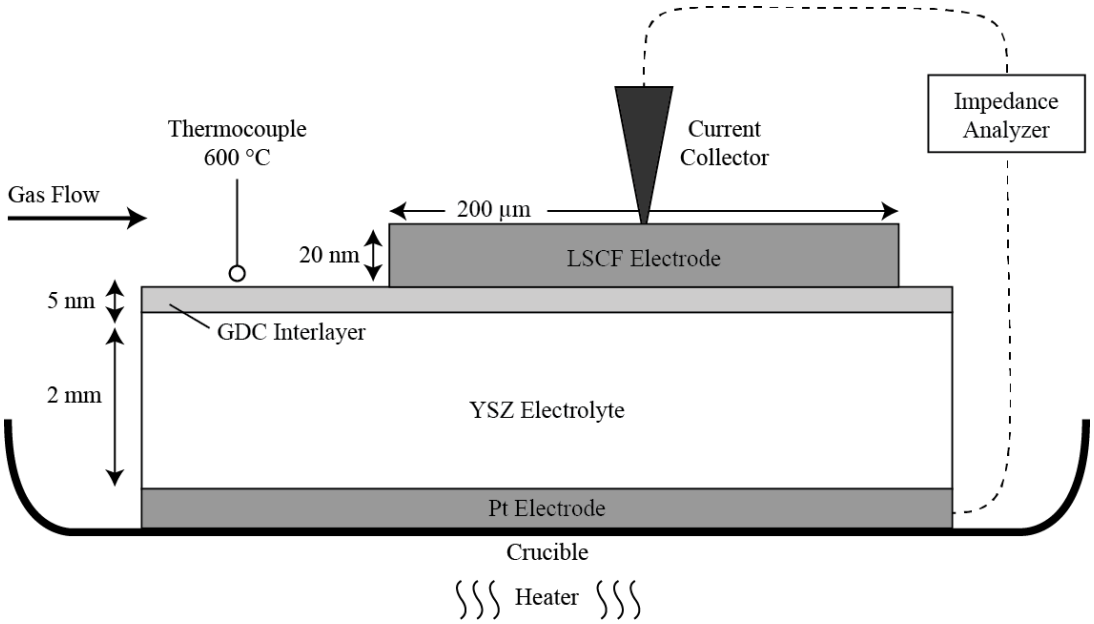

Figure 34. Microelectrode test setup.

6.1.3 Results

Figure 35(left) illustrates the instability of the characteristic EIS resistance ("arc height") of a 200 µm diameter thin-film electrode at 600°C measured over the course of ~100 hours and different O2/Ar blends, complicating interpretation of the surface kinetics. Despite this fluctuation in cell resistance and time constant ("peak frequency"), the volume-specific capacitance (VSC) remained stable at a given p_{O2} (Figure 35, right).

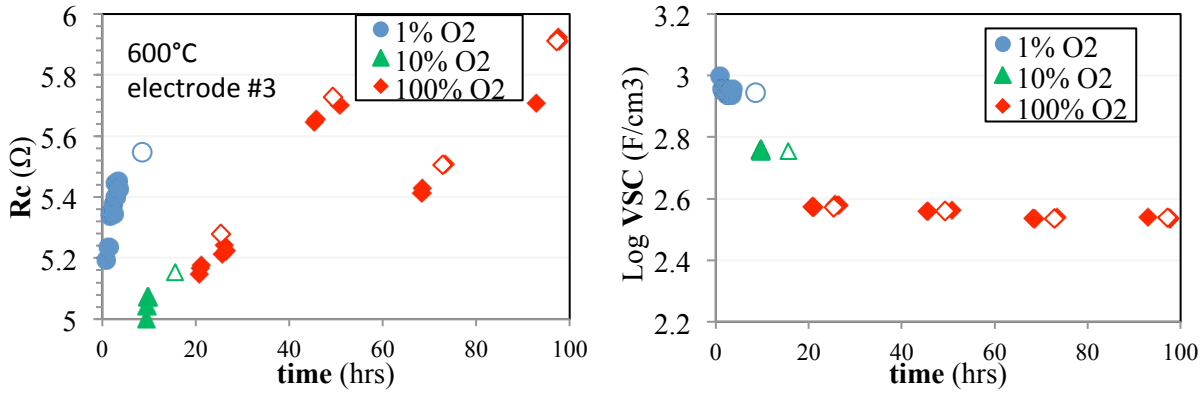

Figure 35. EIS results of a single 200 µm diameter electrode at 600°C, showing (left) characteristic resistance, and (right) volume-specific capacitance over a 100-hour period. Open symbols represent the linear portion of an NLEIS run at the end of the NLEIS sweep.

Interspersed between the EIS measurements shown in Figure 35, several NLEIS measurements, each lasting between 4 and 10 hours, were conducted. Figure 36a shows the linear portion of three NLEIS spectra. In order to account for the performance drift during each NLEIS measurement, the linear response of Figure 36a was fit to an RC equivalent circuit with fixed capacitance and ohmic resistance (taken from Figure 35b) and varying $R_c(t)$, resulting in Figure 36b. Figure 36c & d show

the second- and third-order nonlinear responses after scaling to the drift-corrected characteristic resistances and time constants.

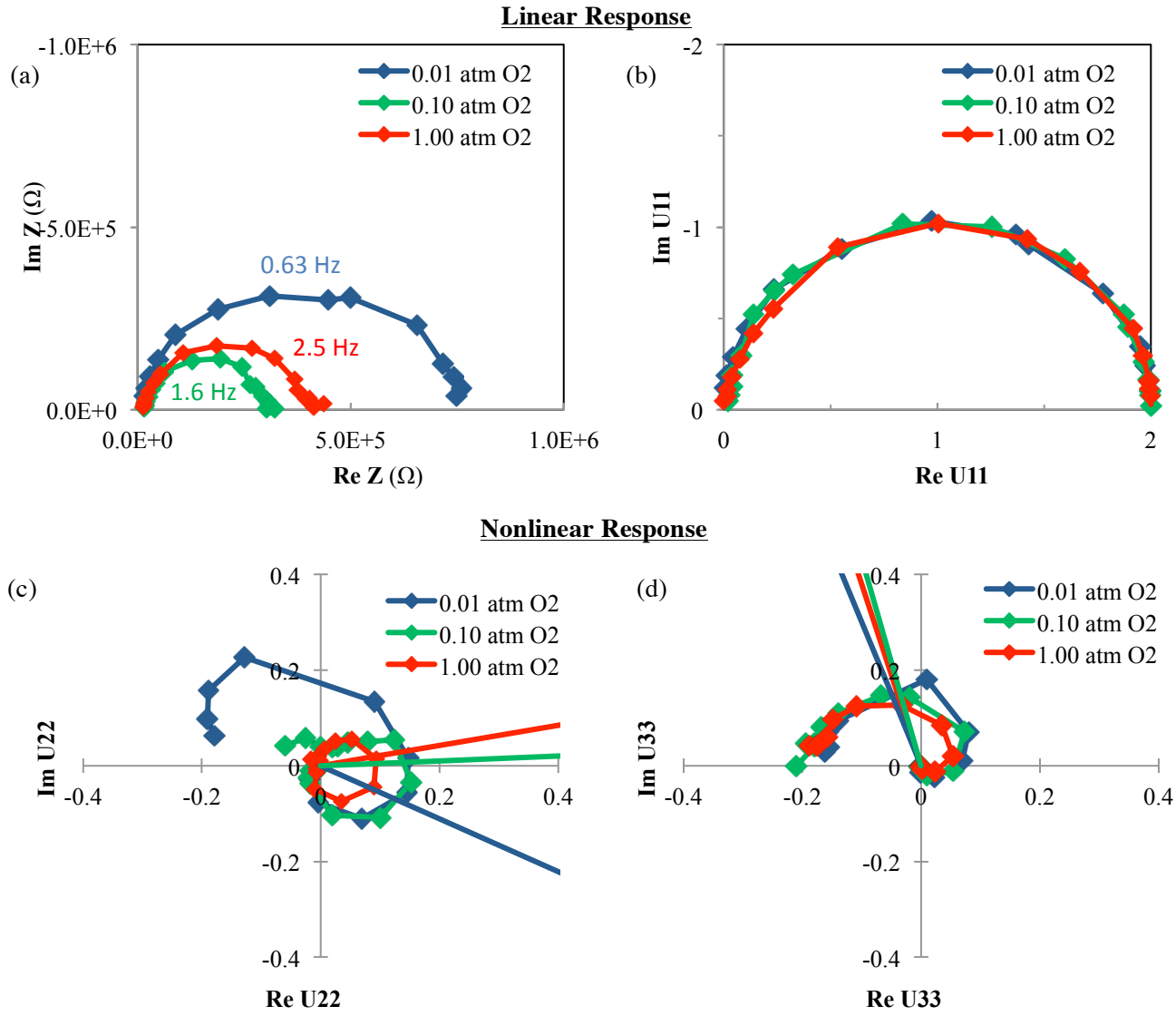

Figure 36. The linear portion of the NLEIS response is shown (a) before and (b) after correcting for performance drift and scaling to characteristic resistance and time constant. The (c) second (d) third-order nonlinear response is shown for a 600°C LSCF electrode.

Figure 37 shows how the nonlinear response of the cell changes in a single gas environment over a hundred-hour period. While U_{33} remains constant, U_{22} cycles between a circular (25, 73 hrs) and semicircular (49, 97 hours) shape, roughly corresponding to the lower and higher values of R_c, respectively, shown in Figure 35. The final third harmonic response (97 hours) could not be resolved and was therefore omitted. These changes in U_{22} represent shifts in the time constant of any second-order physics affecting electrode performance. While the linear response is changing with time (R_c), this implies that purely linear phenomena alone cannot explain the cell's transient behavior.

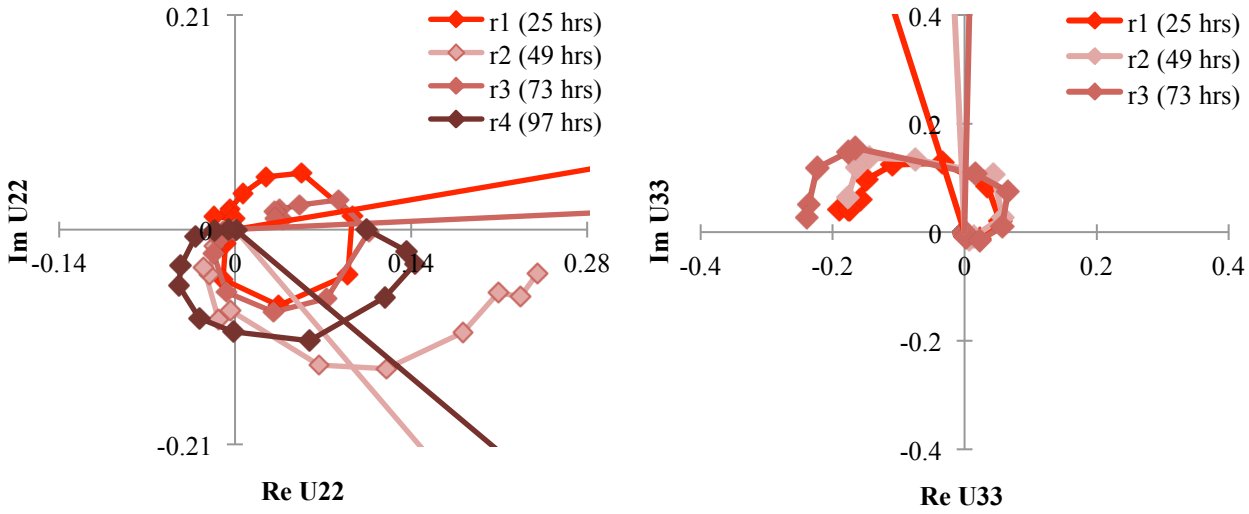

Figure 37. NLEIS spectra in 100% O2 and 600°C measured over a 100 hour period.

Huber *et al.* suggest that the current collector tip may act as a heat sink, cooling a portion of the asymmetrically heated electrode[22]. To assess the severity of this possibility, we measured EIS on an array of microelectrodes of varying diameter. Figure 38 shows the area-specific resistance (ASR) of the electrodes as a function of diameter. At small area, the ASR deviates from the expected area-independence. We fit this trend to a model assuming a 56 µm diameter central portion of each electrode was inactivated due to a tip-cooling effect. For a 200 µm diameter electrode, this only accounts for 8% of the surface area. The ASR approaches area-independence at 200 µm, therefore our model does not incorporate temperature inhomogeneity.

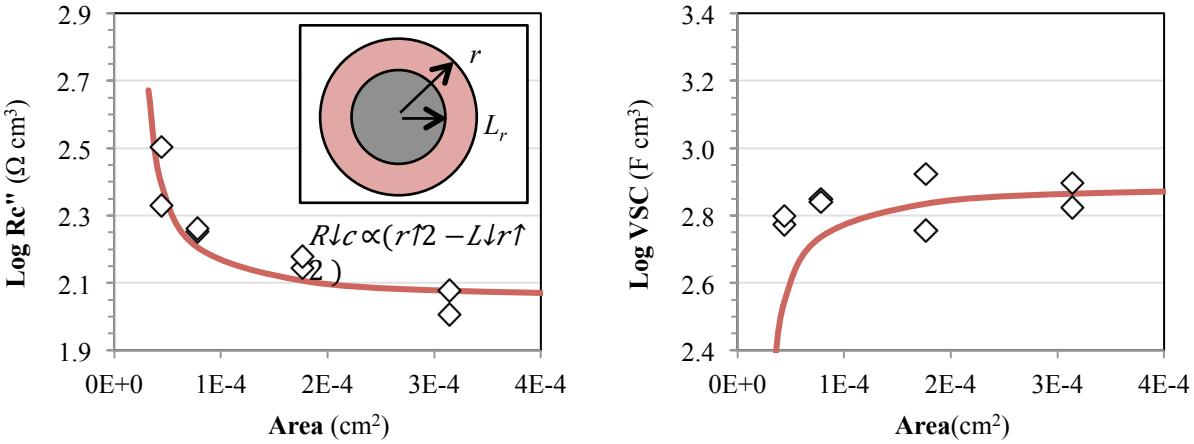

Figure 38. The ASR and VSC of identical microelectrodes of varying diameter are compared to model assuming a 56 µm diameter circle is completely inactive.

6.1.4 Discussion

Figure 39 compares the measured VSC to the predicted chemical capacitance produced by changes in oxygen nonstoichiometry using the p-type and empirical thermodynamic models previously described for LSCF[23]. While the measured and predicted VSC are of similar magnitude, the p-type model predicts a steeper slope than observed; the empirical model captures both the magnitude and slope of the VSC. This suggests that the LSCF thin film of this study and the bulk LSCF measured by Kuhn *et al.* share similar thermodynamic properties.

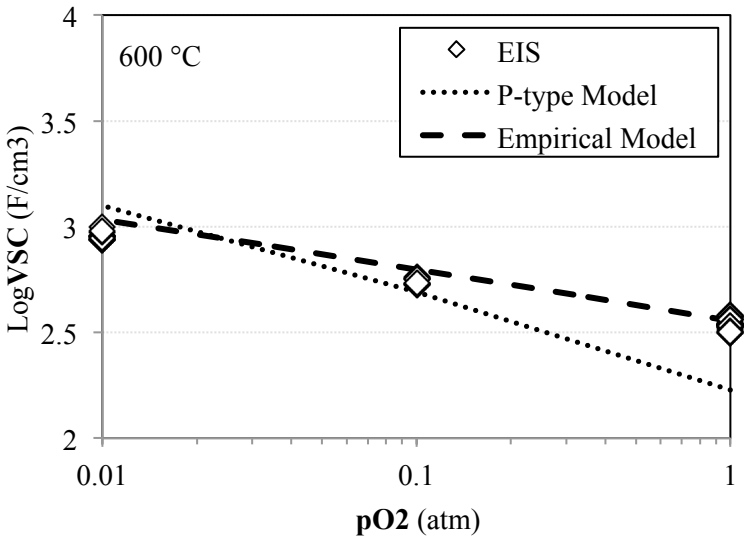

Figure 39. The VSC of an LSCF-6428 electrode at 600°C measured over a 100-hr period is compared to that predicted by models for bulk LSCF oxygen nonstoichiometry[23].

Comparing the first three NLEIS measurements (1%, 10%, 100% O_2) to modeled nonlinear responses highlights the technique's sensitivity to the thin films thermodynamic behavior and surface kinetics. Using a p-type model, no value of n in the empirical rate law ($\propto p_{O2}\delta^n$) could fit the NLEIS spectra. Only by assuming a non-uniform distribution of p-type materials of varying reducibility could one achieve suitable agreement. Conversely, using the empirical thermodynamic model, Figure 40 shows that n = 1.8 captures the observed nonlinear response. Any deviations of the surface reducibility from the bulk (not considered in this model) could skew n from an integer value. The deviation of LSCF at high p_{O2} and low temperatures from a p-type semiconductor model corresponds to a dispersion of free energies of oxidation. One may interpret this dispersion as a physical distribution of non-uniform material (*i.e.* separate volumes of varying reducibility) or conversely a uniform material not fully described by a traditional p-type point-defect model.

Due to the adequate agreement of the spectra to a uniform-thermodynamics model, more refined models considering gradients in thermodynamics would likely be indistinguishable from the present model.

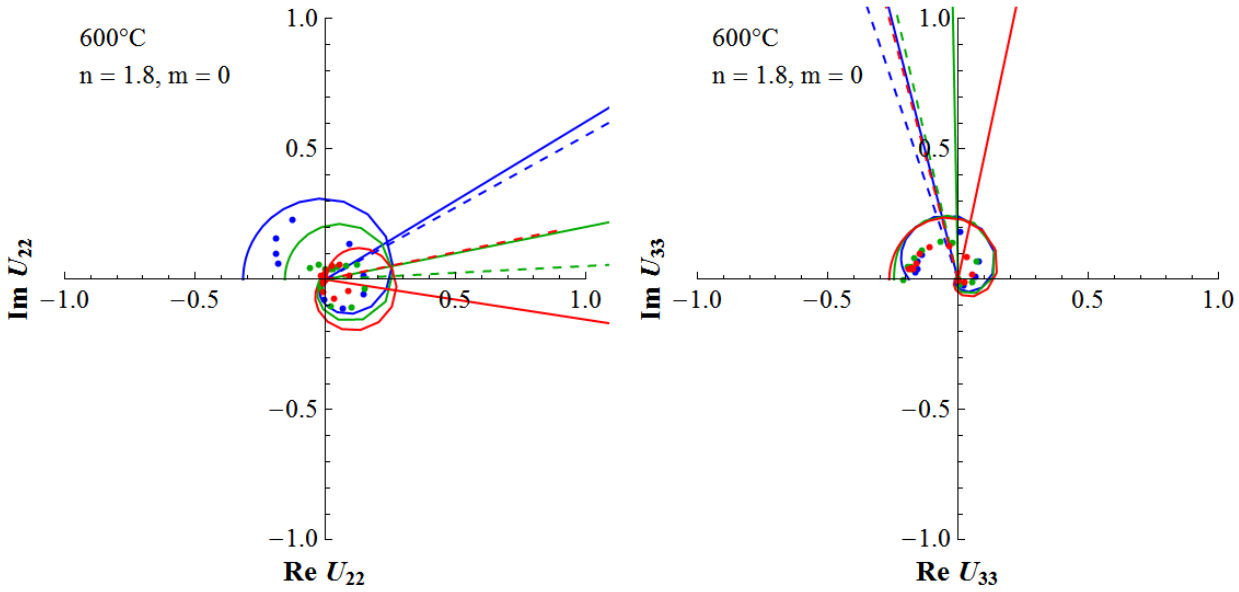

Figure 40. Best fit of the thin film model assuming a uniform material described by the empirical thermodynamic model; *n* is the only adjustable parameter.

The final 100-hour measurement period in a single gas environment showed fluctuations in R_c while VSC remained nearly constant. The constant VSC implies changes in the electrode behavior must be confined to regions of negligible volume—likely gas-solid or solid-solid interfaces. Variations in impedance of concurrently measured microelectrodes on the same electrolyte substrate did not share same R_c trends, ruling out environmental oscillations (temperature, p_{O2}, etc.). Furthermore, the variation in U_{22} implies the changing physics cannot be purely linear (e.g. changing surface rate constant, interfacial resistance, etc.). The best fits for a circular (n = 1.8) and semi-circular (n = 2) U_{22} show that slight changes in the surface reducibility could account for this variation. However, the seemingly cyclical nature of the changes is at odds with a simple surface re-equilibration process.

6.2 Impedance Measurements on Porous LSCF-6428

6.2.1 Theory

We use a one-dimensional macrohomogeneous model as a first approximation of a porous electrode, shown in Figure 41. This model treats the electrode thermodynamics and surface kinetics in the same manner as the thin film model. We assume a uniform distribution of microstructural features (porosity, tortuosity, surface area, *etc.*), and assume the characteristic bulk diffusion length is large relative to a single particle diameter (~ 0.5 μm). Under these conditions, a model considering only bulk transport normal to the electrode-electrolyte interface (z-direction) is sufficient, described by Fick's equation for moderately-dilute species, N_δ ($\frac{mol}{cm^2 s}$) is the molar vacancy flux, D_v($\frac{cm^2}{s}$) the vacancy diffusivity, and c_o($\frac{mol}{cm^3}$) is the concentration of oxygen lattice sites.

$$N_\delta = \frac{1}{2} c_O D_v \delta \frac{\mathrm{d}\ln f_{O2}}{\mathrm{dz}}$$

Eqn. 9

Surface transport, compositional gradients in the electrode, gradients in the electrochemical potential of electrons, and the electrode-electrolyte charge-transfer resistance are assumed to be negligible.

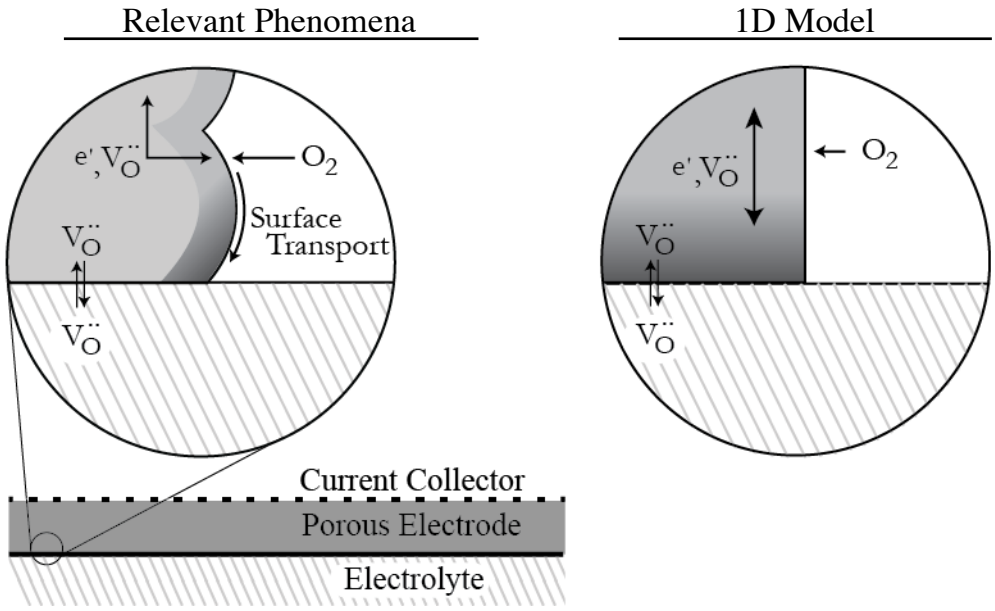

Figure 41. One-dimensional macrohomogeneous model approximation.

6.2.2 Experimental

Powders of $Ce_{0.9}Gd_{0.1}O_2$ (GDC, Praxair, 7.08 m2/g) were uniaxially pressed in a cylindrical die at 6,000 psi for 3 minutes, then fired at 1500°C for 4 hours, ramping at 2°C/min to produce a dense electrolyte pellet. $La_{0.6}Sr_{0.4}Co_{0.2}Fe_{0.8}O_{3-\delta}$ powder (Praxair, 6 m2/g) was micronized for 30 minutes to break up agglomerates before mixing with an organic solution (91.5 wt% α-terpineol, 0.5% oleic acid, 8% ethyl cellulose), producing an ink with 50% solids loading. A three-roll mill with 127 µm spacing was used to ensure an even distribution of solids in the ink. The ink was screen-printed onto both faces of the GDC electrolyte and a reference electrode was hand-painted along the perimeter of the pellet. Figure 42 shows the LSCF|GDC cell after sintering at 1050°C in air for 2 hours, ramping at 2°C/min.

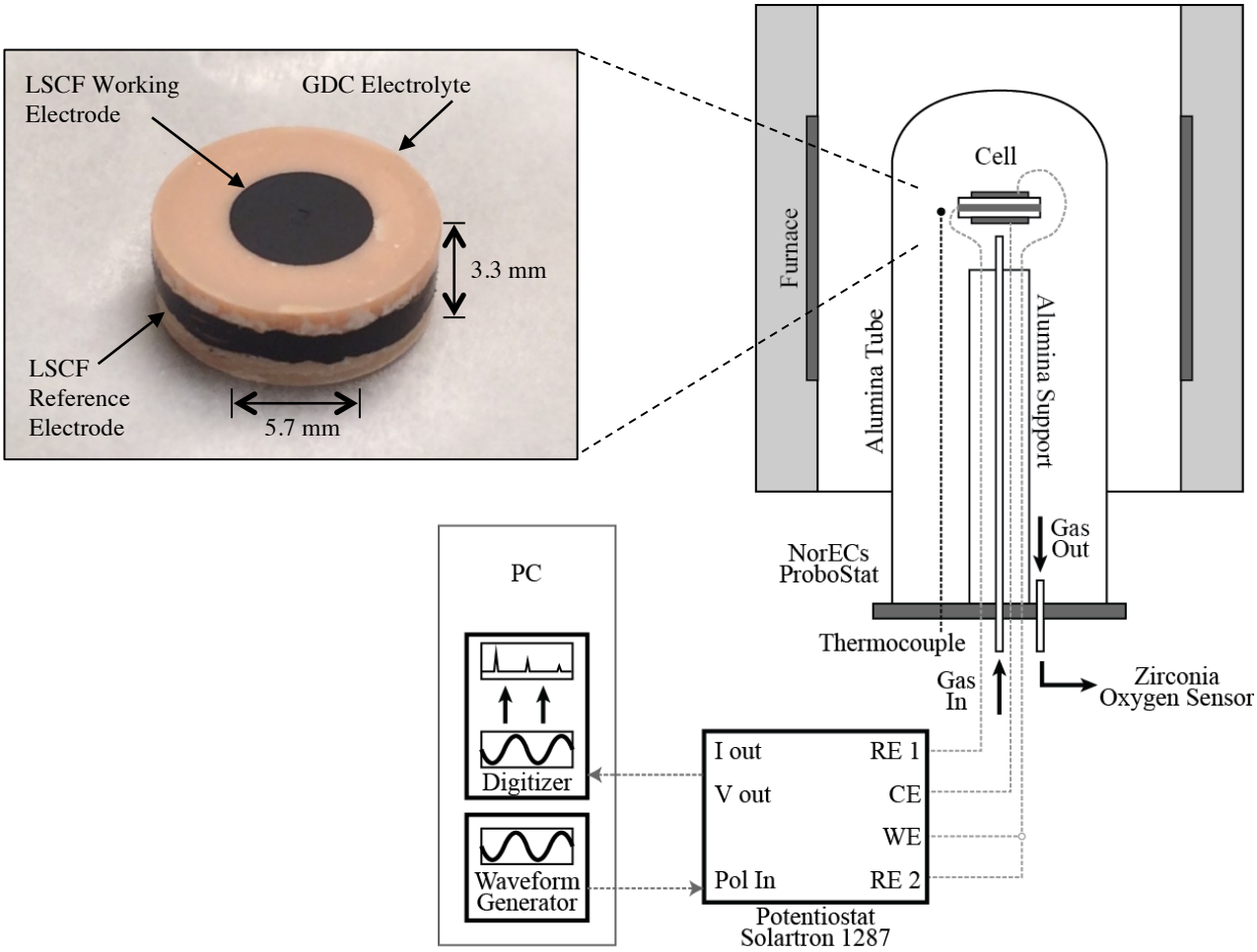

Figure 42. Porous electrode impedance test setup.

Linear and nonlinear electrochemical impedance spectroscopy (EIS, NLEIS) were performed in 1%, 10%, and 100% oxygen (balance nitrogen) environments at 550, 600, and 650°C. All presented spectra correspond to single-chamber half-cell measurements. Galvanostatic zero-bias AC perturbations producing half-cell voltage response amplitudes between 10 mV (most linear) and 160 mV (most nonlinear) and perturbation frequencies ranging from 100 MHz to 5 mHz were performed once the system was allowed to equilibrate with the new gas and temperature environment for at least 48 hours. A full amplitude (20) and frequency (10/decade) sweep at a single temperature and p_{O2} lasted between 6 and 12 hours.

6.2.3 Results & Discussion

Figure 43 summarizes the EIS spectra for the initial temperature and p_{O2} sweep within the cell's first 13 days of operation. The half-tear drop Gerischer shape suggests a co-limitation of kinetics and diffusion[24]. At higher temperature and p_{O2}, the arcs show minor flattening from this ideal shape, previously interpreted as an increased role of surface diffusion [25].

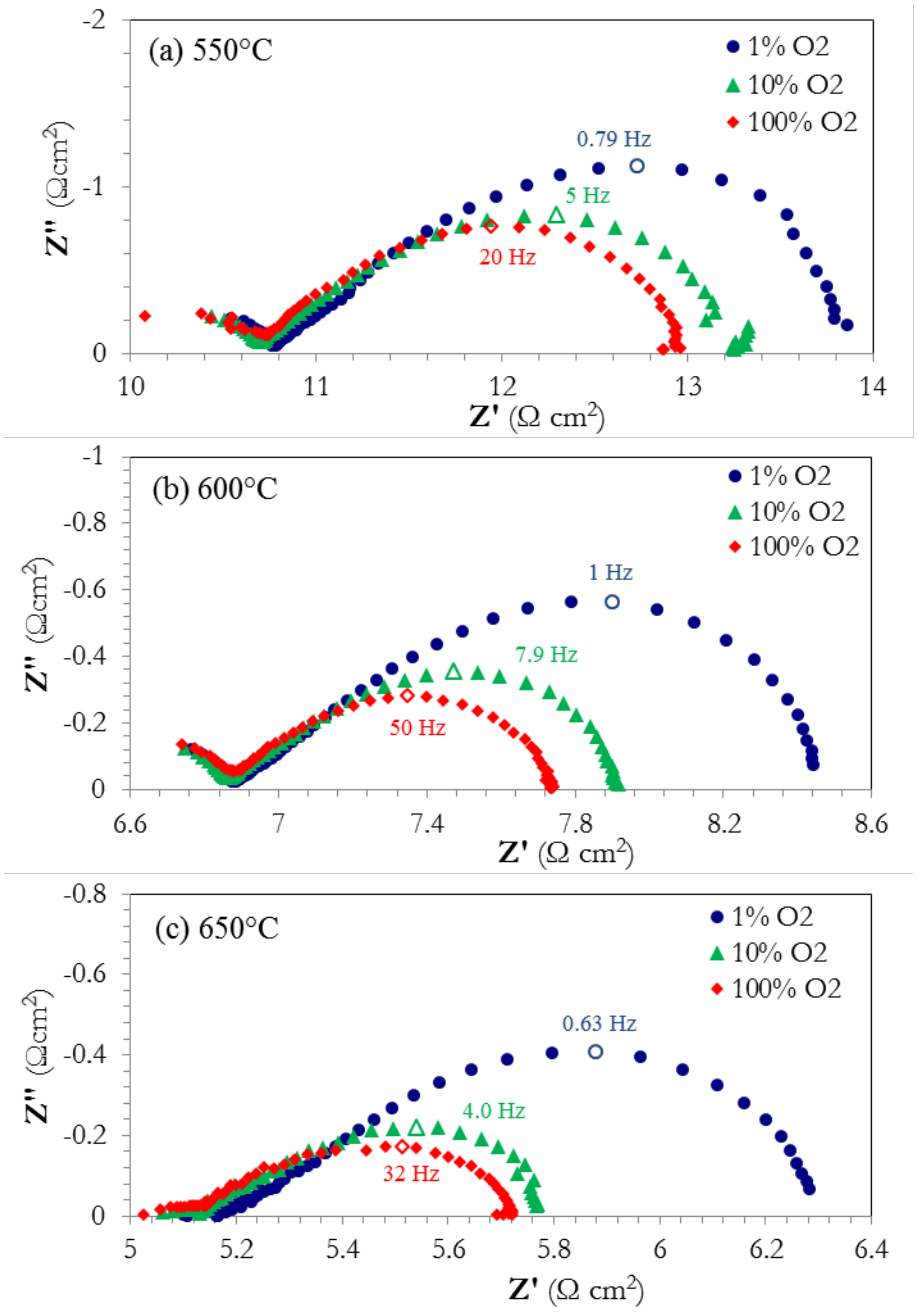

Figure 43. The EIS spectra at 0.01, 0. 1, and 0.01 atm O2 and 550, 600, and 650°C show a Gerischer-like shape, supporting a co-limitation of kinetics and diffusion.

Figure 44 summarizes the p_{O2} and temperature trends of the characteristic resistance and frequency, along with an estimation of the vacancy diffusion characteristic length (from relating the measured

capacitance to the predicted VSC). The characteristic frequency is especially sensitive to the surface kinetics; the observed p_{O2} dependence matches that of an equilibrium forward exchange rate proportional to $p_{O2}\delta^{1.7}$. The estimated characteristic diffusion length suggests that the active region of the electrode is confined to within 1-8 particle diameters of the electrolyte.

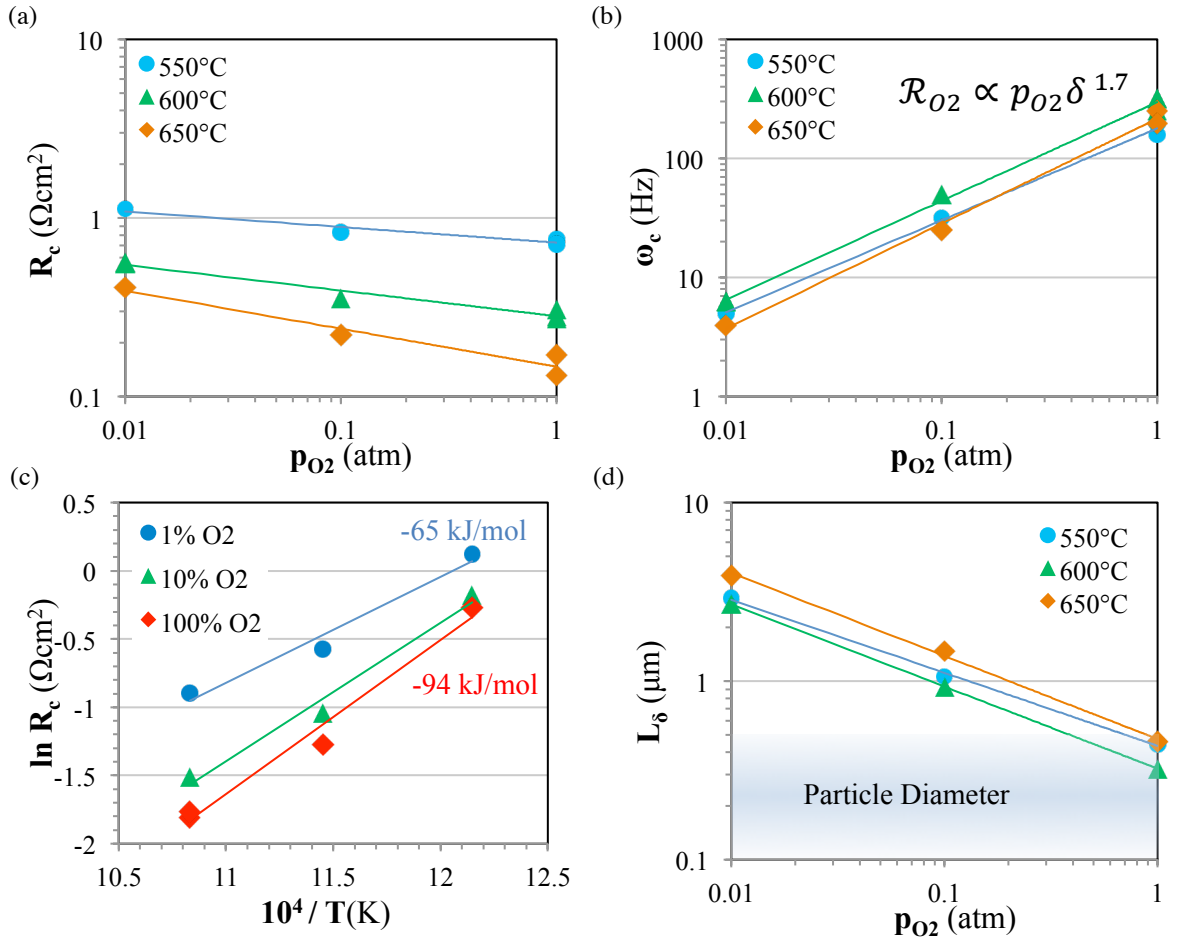

Figure 44. Summary of the pO_2 and temperature trends of the characteristic resistance, frequency, and vacancy diffusion length.

Figure 45 shows the characteristic resistance and capacitance over a ~1 year period in 650°C and 1 atm O_2. The initial 100 day period accounts for the majority of the cell's increase in R_c and C_{chem}, while the final 250 days exhibit a slowed exponential increase in R_c, with the capacitance remaining nearly constant.

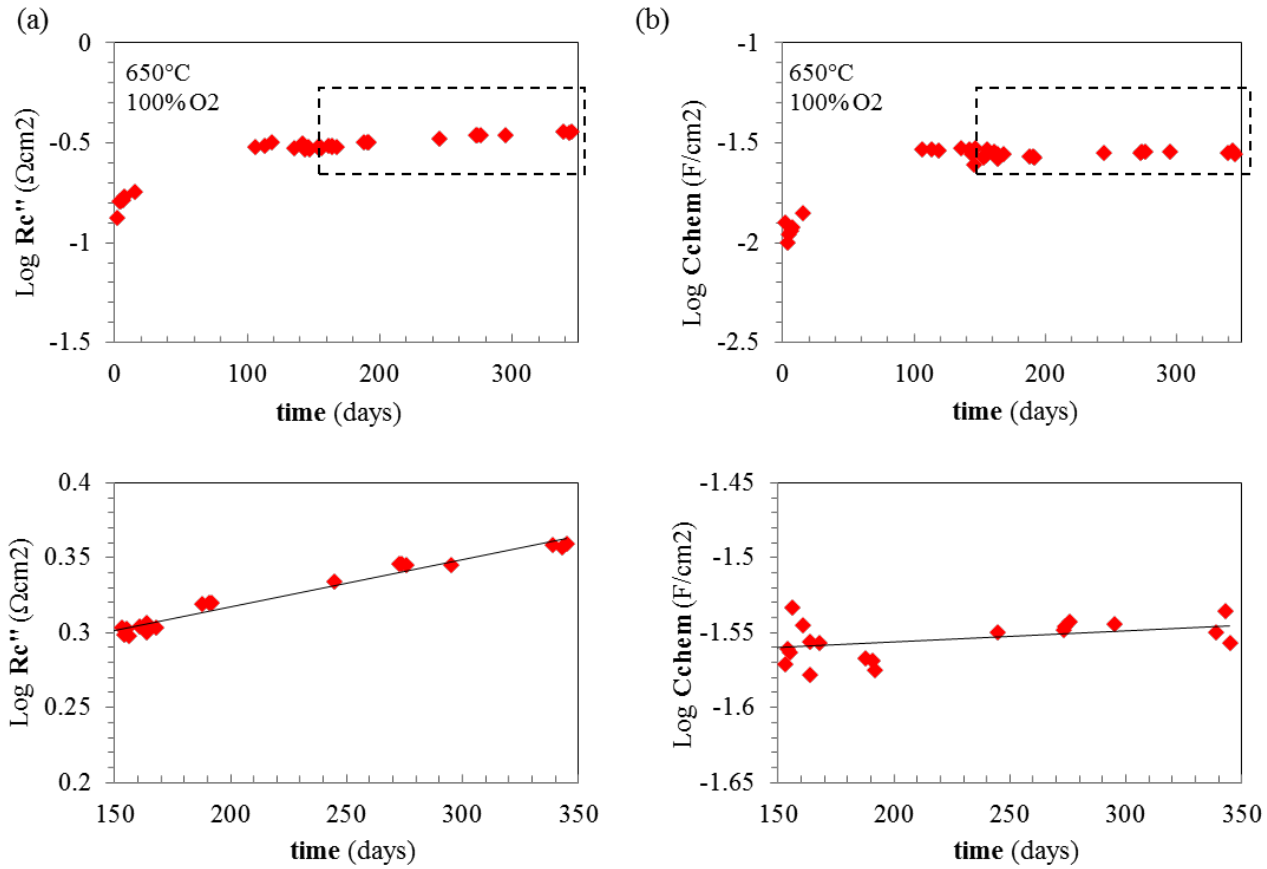

Figure 45. Characteristic resistance and capacitance over a ~1 year period in 650°C and 1 atm O_2.

Figure 46 shows the NLEIS spectra collected after 275 days at 650°C in 1% (blue), 10% (green), and 100% (red) O_2, well into the more stable region shown in Figure 47. Phasor lines indicate the shift in characteristic time constant of the harmonic response as a function of p_{O2}. U_{22} and U_{33} exhibit a clear clockwise phasor line rotation and shift of the low-frequency intercept towards the positive real axis with increasing p_{O2}.

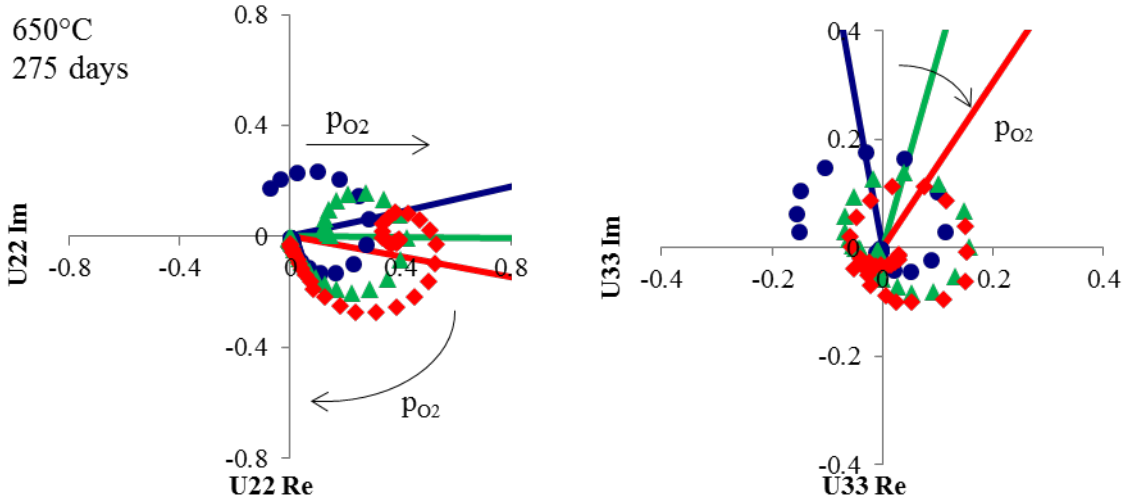

Figure 46. Second and third harmonic NLEIS spectra collected after 275 days at 650°C in 1% (blue), 10% (green), and 100% (red) O_2.

Using a p-type thermodynamic model, we were unable to fit the above spectra regardless of rate law, without assuming portions of the electrode to be of varying reducibility. However, using the empirical thermodynamic model, we could qualitatively capture the observed p_{O2} trends assuming a forward rate law proportional to $p_{O2}\delta^{1.5}$. This minor deviation of n from that predicted by EIS ($n \approx 1.7$) and the thin film measurements ($n \approx 1.8$) could be a manifestation of errors arising from neglecting surface transport, enhanced surface reducibility, or multi-dimensional transport.

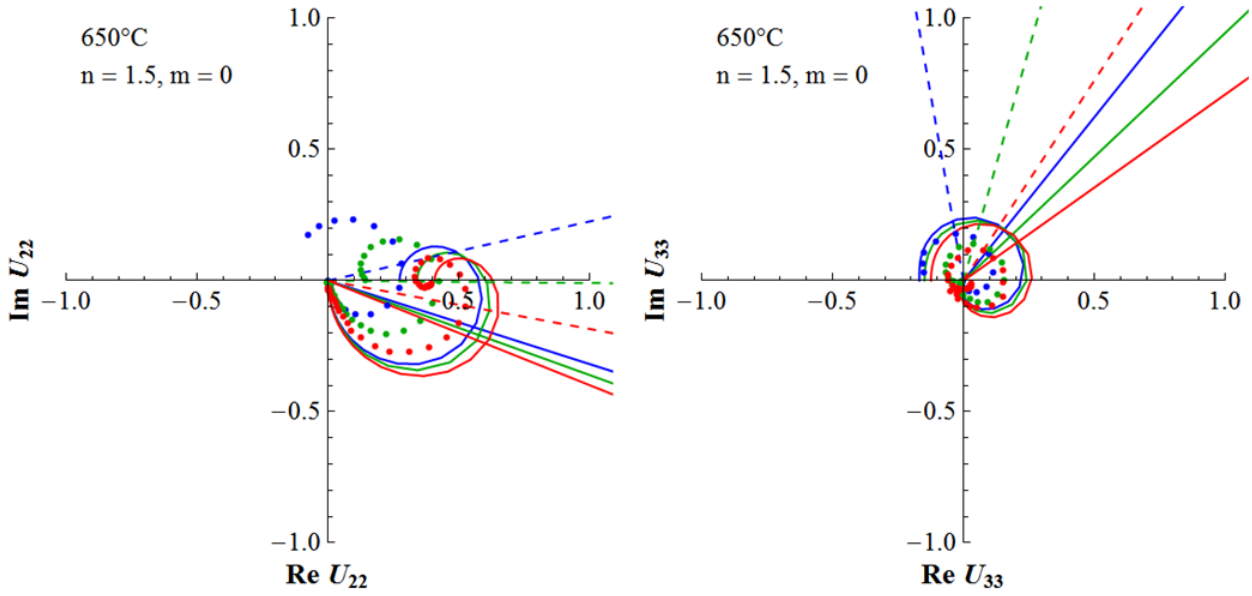

Figure 47. Best fit of the 1D macrohomogeneous model at 650°C.

Figure 48 shows the change in nonlinear response over the 1-year measurement period. U_{22} undergoes a 1.6x decrease in magnitude over the first 190 days, compared to the 2.7x change observed for R_c. Beyond 190 days, no measureable change in NLEIS spectra was observed.

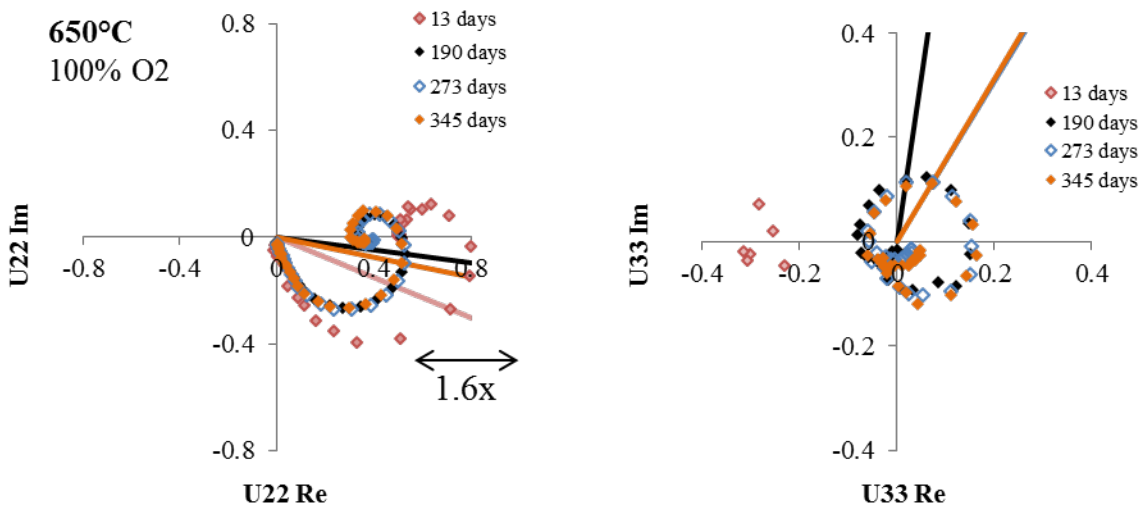

Figure 48. Shift in NLEIS response over 1-year measurement period in 100% O_2 and 650°C.

Because NLEIS scales out changes in the linear impedance, this diminishing of the harmonics implies that the phenomena affecting the transients are at least partially nonlinear. Therefore, linear phenomena (e.g. changes in microstructure, surface site availability/rate coefficient, etc.) alone cannot account for the observed initial drop in performance. However, the observed 1.6x change in U_{22} is much smaller than the 2.7^2x change expected for an entirely nonlinear system; this implies that even in this initial 190-day period, the majority of the degradation must be attributed to linear phenomena. A long-term equilibration process such as cation redistribution could account for the initial small nonlinear changes, while any purely linear phenomena (e.g. changes in surface rate coefficient) could account for the majority of degradation.

6.3 LBF and LBFM Electrode Preparation and Characterization

The materials studied in this section were pursued based on some theory predictions from UW developed under separate funding. While none of these studies were strictly part of this project, we mention the initial results here as they were the result of close collaboration among the team members, which was in part enabled by this grant. Powder samples of $La_{0.125}Ba_{0.875}FeO_{3-\delta}$ (LBF) and $La_{0.125}Ba_{0.875}Fe_{0.9}Mn_{0.1}O_{3-\delta}$ (LBFM) (provided by MIT) were prepared into electrode inks by mixing 1:1 by weight with an organic solution of 89.7% a-terpineol, 9.8% ethyl cellulose, and 0.5 wt. % oleic acid. The solids were evenly dispersed using a three-roll mill with a 0.127 mm roller spacing. The resulting ink was screen printed onto $Gd_{0.1}Ce_{0.9}O_{2-\delta}$ (GDC-10) electrolyte pellets, and fired in the presence of 250 sccm of synthetic air. Various firing conditions were tested in order to optimize electrode adhesion without compromising porosity.

6.3.1 XRD

Figure 49 below shows the XRD spectra of a LBF|GDC cell fired at 1050 °C for 1 hour, ramping at 2 °C/min. All peaks present correspond to the characteristic peaks of either ceria or a perovskite; no tertiary phases indicative of electrode-electrolyte reaction are observable.

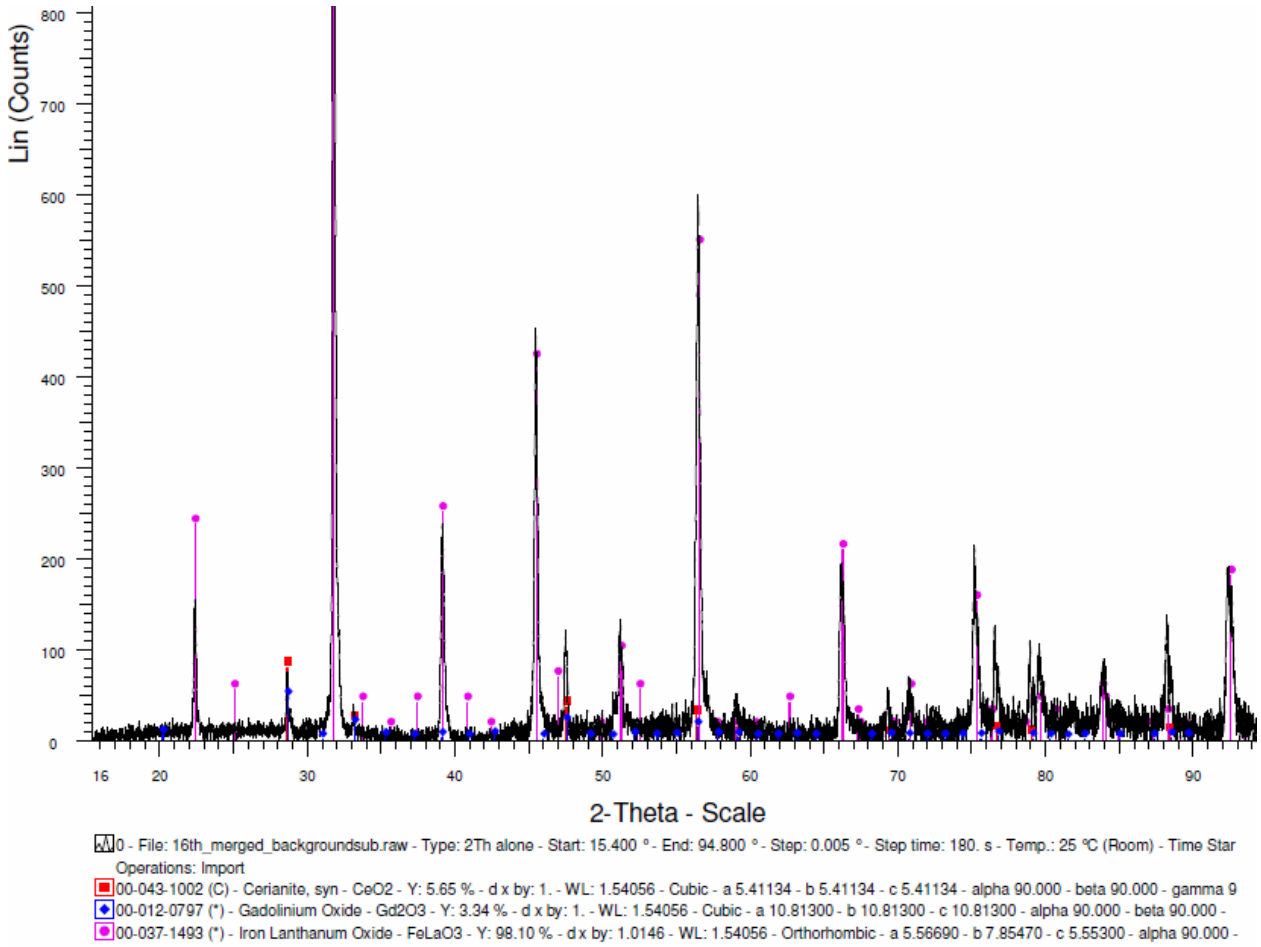

Figure 49. XRD spectrum of a La0.125Ba0.875FeO3-δ|GDC-10 cell compared to PDF's for ceria and $LaFeO_3$.

6.3.2 SEM

Figure 50 shows the cross-sections of two LBF|GDC cells fired at 1050 and 1200 °C for 1 hour, ramping at 2 °C/min. The former appears under-sintered with poor contact with the electrolyte; the latter shows slightly better contact with GDC, yet suffers from a drop in porosity. Intermediate temperatures, longer dwell times, and slower ramp rates for both LBF and LBFM failed to yield sufficient adhesion with the GDC electrolyte.

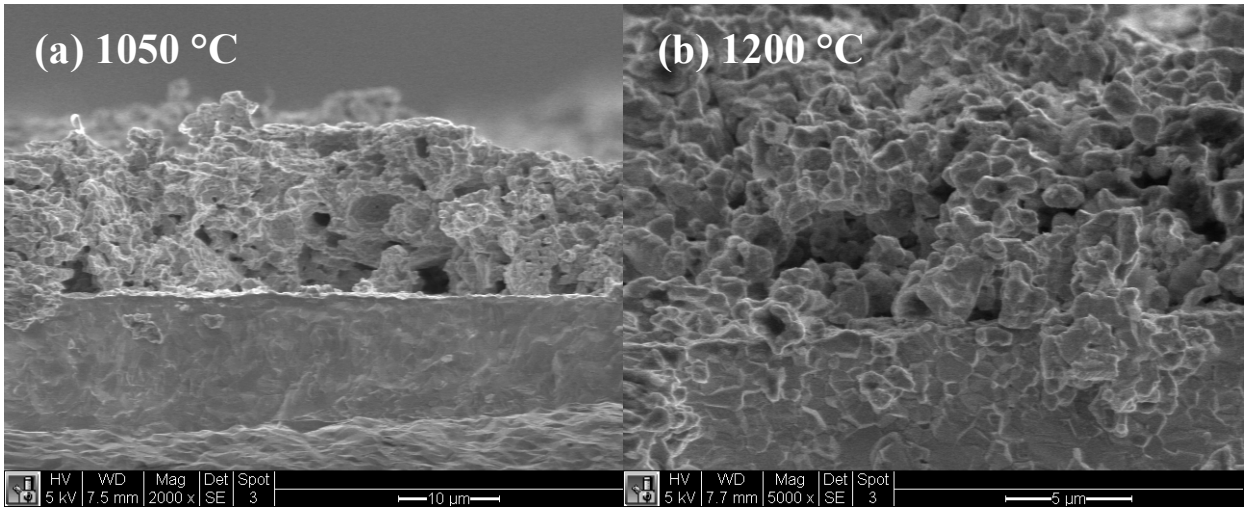

Figure 50. SEM images of LBF|GDC cross-sections, sintered at different temperatures.

6.4 Summary

Thin Film. Analysis of thin film impedance measurements allows the removal of microstructural effects and multiple diffusion pathways inherent to porous electrodes, in turn isolating the surface kinetics and material thermodynamics. Both linear and nonlinear impedance show that the p-type point-defect model typically used in iron-rich LSCF compositions was insufficient for describing LSCF-6428 under the conditions studied. An empirical thermodynamic model (fit to independent TGA data) and surface rate law proportional to $p_{O2}\delta^{n}$ were used to interpret our results. Both EIS and NLEIS spectra could be explained with a material of uniform thermodynamics and n = 1.8, closest to that of a dissociative adsorption rate law (n = 2) describing physisorption and dissociation of diatomic oxygen to two adjacent surface vacancy sites. Changes in impedance in a single gas environment were attributed to small changes in the surface reducibility; however, the driving force and mechanism for such a change are unclear.

Porous Electrode. The Gerischer shape of the EIS response implies a co-limitation of diffusion and kinetic phenomena. As a first approximation, we interpret the EIS and NLEIS spectra using a 1D macrohomogeneous model considering only bulk diffusion and uniform thermodynamics. The observed p_{O2} dependence of ω_c suggests a rate law of the form $p_{O2}\delta^{1.7}$. The measured capacitance suggests the active volume of the electrode is confined within 1-6 particle diameters of the electrolyte. Agreement between the NLEIS response and the 1D model was obtained assuming a rate law of the form $p_{O2}\delta^{1.5}$. As the only adjustable parameter, sufficient surface transport, enhanced surface reducibility, or multi-dimensional transport could complicate direct interpretation of n. Over the year-long testing period, LSCF was observed to be very stable, only undergoing a 2.7x increase in ASR. The majority of this deterioration happened over the initial 150 days gas exposure at 650°C. The nature of this degradation is tied principally to linear phenomena, evidenced by the minute changes in NLEIS response. However, a small portion of this degradation resulted in a measurable change in the second voltage harmonic, suggestion the presence of a long-term nonlinear equilibration process involving shifts in bulk composition.

7 Thrust 3: *Ab Initio* Calculations and Thermokinetic Modeling

7.1 Trends in Bulk and Surface Oxygen Defect Energetics of $La_{2-x}Sr_xMO_{4\pm\delta}$ (M=Co, Ni, and Cu)

7.1.1 *Ab Initio* Modeling Approaches

Spin polarized Density Functional Theory (DFT) calculations were preformed with the Vienna *Ab-initio* Simulation Package [26, 27] using the Projector-Augmented plane-Wave method [28] with a cutoff of 450 eV. Exchange-correlation was treated in the Perdew-Wang-91 [29] Generalized Gradient Approximation (GGA). The GGA+*U* calculations [30] are performed with the simplified spherically averaged approach [31], where the U_{eff} (U_{eff} = Coulomb *U* - exchange *J*) is applied to *d* electrons. (U_{eff}(Co) = 3.3 eV, U_{eff}(Ni) = 6.4 eV, and U_{eff}(Cu) = 4.0 eV) [32-34]. All calculations are performed in the ferromagnetic state in order to use a consistent and tractable set of magnetic structures.

Bulk defect calculations are performed using fully relaxed 56-atom and 112-atom supercells with and without oxygen defects, which correspond to oxygen nonstoichiometry content of δ = 0.125 and δ = 0.0625 for the defect containing supercells, respectively. Simulated supercells are shown in Figure **51**. Oxygen vacancies were created at the equatorial oxygen lattice site of the M-O octahedra, while oxygen interstitials were created inside the La-La tetrahedra between the AO Rocksalt layers. Although only one cation arrangement was chosen for the model at a specific Sr content, additional cation ordering studies suggest the coupling between oxygen defect stability and cation ordering leads to energy variation of ≤0.5 eV/defect for defect stability revealed below, as shown in **Figure 54**. On the other hand, the range of the defect formation energy vs. Sr content spans a few eV range as shown in the figures below in Section 6.2.2 (Figure 52 and Figure 53). Therefore, we expect the A-site cation ordering effect in $La_{2-x}Sr_xMO_4$ will not alter the trends of oxygen defect stability vs. Sr content discussed here. The many cation ordering studies were done with high throughput automated *ab initio* calculations using the workflow capabilities of the Materials Simulation Toolkit (MAST) [35, 36].

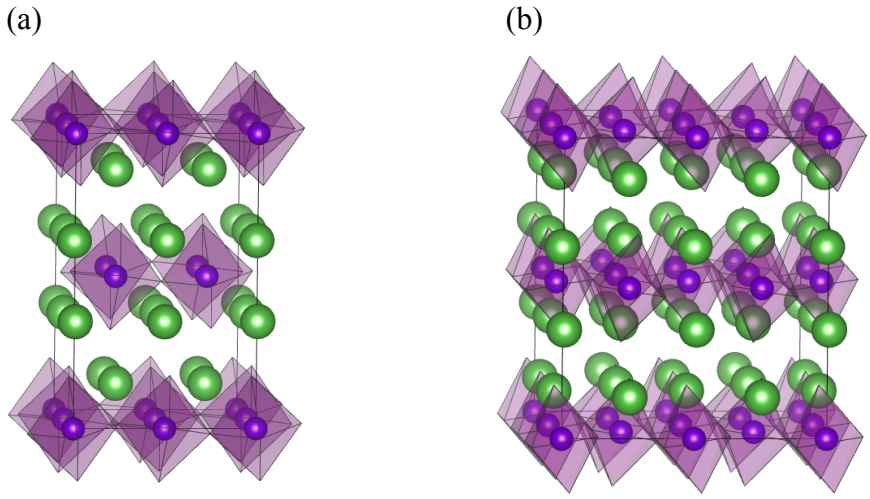

Figure 51**.** The simulated (a) 56-atom and (b) 112-atom $La_{2-x}Sr_xMO_4$ supercells (M=Co, Ni, and Cu). The green circles represent the La/Sr atoms and the purple circles represent the transition metals (M). Lattice oxygens are located at the corner of the M-O octahedra. For Sr doped $La_{2-x}Sr_xMO_4$ systems, Sr were distributed evenly in each A-O layer and the Sr were placed as far apart as possible within the AO layer and between two adjacent AO layers. Oxygen vacancies were created at the equatorial lattice oxygen site of the M-O octahedral while oxygen interstitials were created within the La-La tetrahedral between the two A-O Rocksalt layers.

7.1.2 *Ab initio* bulk oxygen defect formation energies for $La_{2-x}Sr_xMO_4$ (M=Co, Ni, and Cu)

Figure 52 and
Figure 53 show the computed DFT oxygen vacancy formation energies, $E(O_{vac})$s (red empty squares) , and two oxygen interstitial formation energies ($E(O_{int(ion)}$ - green filled circles, and $E(O_{int(peroxide)}$ - blue filled diamonds) as a function of the Sr content for $La_{2-x}Sr_xMO_{4\pm\delta}$ (M=Co, Ni, and Cu) bulk simulated using 56-atom and 112-atom supercells, respectively, Although the $E(O_{int})$s values shown in Figure 52 and
Figure 53 are lower than the $E(O_{vac})$s, the oxygen chemical potential reference (DFT total energy of an O_2 gas molecule with an O_2 overbinding energy correction of 0.33 eV taken from Ref. [33]) for the computed oxygen defect energetics is close to the room temperature and 1 atm oxygen partial pressure. Increasing temperature and/or decreasing oxygen partial pressure can decrease the stability of O_{int} while increasing the stability of O_{vac}. Therefore, the dominant oxygen defect species in the RP phases can be switched from O_{int} to O_{vac} by decreasing oxygen chemical potential (*i.e.* at sufficiently high temperature and/or low oxygen pressure condition, assuming the RP phase remains stable against decomposition) at a given Sr content, as well as by varying the Sr content at a given oxygen chemical potential condition. For example, the approximate change of effective oxygen gas phase chemical potential from room temperature to T=1000K at 1 atm is -0.83 eV/O[37],, which will stabilize oxygen vacancy by -0.83 eV/O_{vac} and destabilize oxygen interstitial by +0.83 eV/O_{int} (we note vibrational free energy contribution of lattice oxygen or O interstitial in oxides is neglected here, which may slightly reduce the magnitude by 0.2~0.3 eV/O[33, 38]) when T is increased to from room temperature to 1000 K. The opposite free energy shift of O_{int} and O_{vac} upon increasing T will then make the relative stability between O_{int} and O_{vac} become closer at T=1000 K as compared to that at room temperature for the same pO_2.

As shown in Figure 52 and Figure 53, the bulk $E(O_{vac})$s of $La_{2-x}Sr_xMO_4$ all decrease (become more stable) with increasing x, while bulk $E(O_{int(ion)})$ increases with increasing x and $E(O_{int(peroxide)})$ exhibit weak or no Sr dependence. As discussed in our previous quarterly reports, increasing Sr doping concentration causes oxidation of the transition metals in the RP phases, and the O^{2-} ion interstitial and Sr compete for electrons, which leads to strong Sr concentration dependence for the O^{2-} ion interstitial stability. On the other hand, the weak dependence on Sr content for $E(O_{int(peroxide)})$s is consistent with the fact that formation of O^- peroxide interstitial does not cause oxidation of transition metal cations, and therefore $E(O_{int(peroxide)})$ is relatively insensitive to the Sr concentration and oxidation state of transition metals. The distinct Sr dependences for the two O interstitial species results in a stability crossover between the O^- peroxide interstitial and O^{2-} ion interstitial for the investigated $La_{2-x}Sr_xMO_4$: O^{2-} ion interstitial is more stable in undoped La_2MO_4 while formation of O^- peroxide interstitial becomes more stable than O^{2-} ion interstitial for $La_{2-x}Sr_xMO_4$ at $x \geq \sim 0.75$(Figure 52) for M=Co, 0.5(Figure 53)~0.25(Figure 52) for M=Ni, and 0.25(Figure 52 and Figure 53) for M=Cu. The decreasing value of x, the concentration at which the O^{2-} ion interstitial and O^- peroxide interstitial have the same energy, as transition metal type goes from Co to Cu is consistent with the increasing difficulty of oxidizing the cations. Overall, the oxygen defect energetic trends shown in Figure 52 provide guidance on stability of the oxygen vacancy and oxygen interstitials of the investigated $La_{2-x}Sr_xMO_4$ with respect to the Sr content, x, and transition metal types, M. They defect energies demonstrate that two types of interstitials are expected to be relevant, and that under SOFC relevant conditions a crossover between interstitial and vacancy dominated defect chemistry may occur for all three transition metals, but at different Sr content.

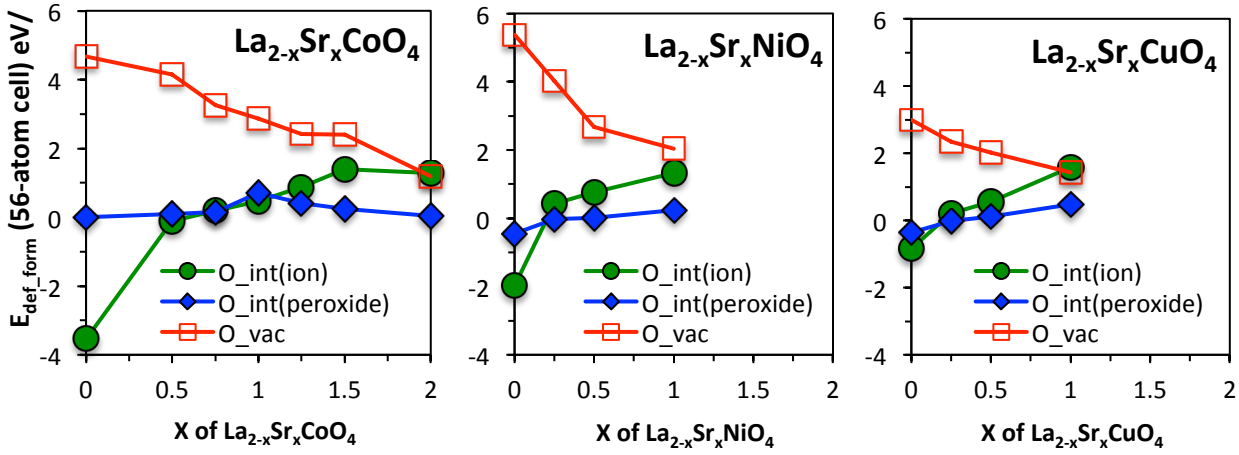

Figure 52. Predicted $La_{2-x}Sr_xMO_4$ (M=Co, Ni, and Cu) oxygen vacancy formation energies, $E(O_{vac})$-red empty squares, and two types of oxygen interstitial formation energies, ($E(O_{int\,(ion)})$-green filled circles, and $E(O_{int\,(peroxide)})$-blue filled diamonds), simulated using 56-atom supercells (corresponds to $\delta = 0.125$). All the defect formation energies shown in **Figure 52** are based on the overbinding corrected DFT O_2 energy reference[33], which corresponds to the condition of approximately 1 atm oxygen partial pressure at room temperature.

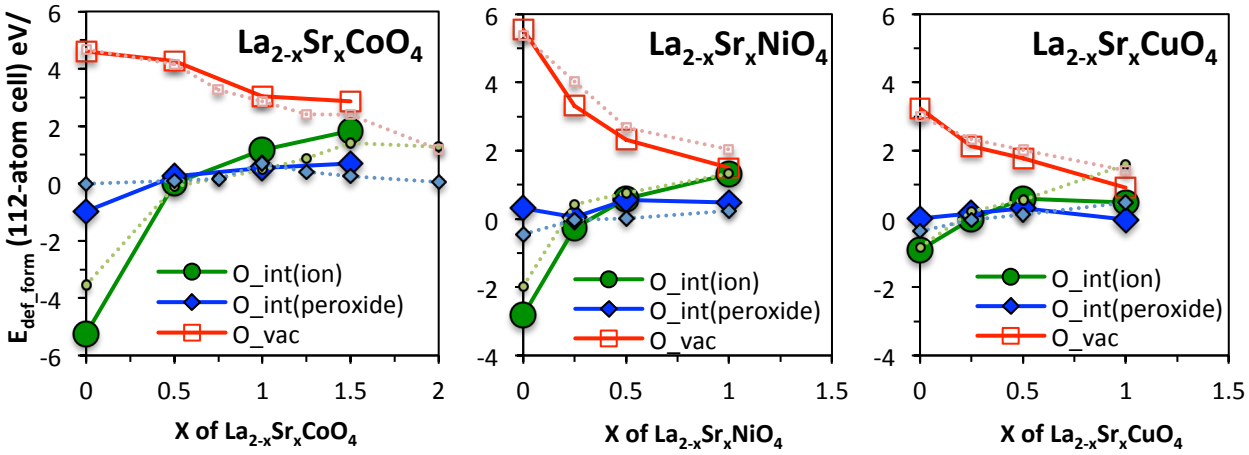

Figure 53. Predicted $La_{2-x}Sr_xMO_4$ (M=Co, Ni, and Cu) oxygen vacancy formation energies, $E(O_{vac})$-red empty squares, and two types of oxygen interstitial formation energies, ($E(O_{int\ (ion)})$-green filled circles, and $E(O_{int\ (peroxide)})$-blue filled diamonds), simulated using 112-atom supercells (corresponds to $\delta = 0.0625$). All the defect formation energies shown in **Figure 53** are based on the overbinding corrected DFT O_2 energy reference[33], which corresponds to the condition of approximately 1 atm oxygen partial pressure at room temperature. The light colored data are the same results as **Figure 52** for showing the defect concentration dependences.

7.1.3 High throughput *ab initio* oxygen interstitial formation energies for $La_{2-x}Sr_xCoO_4$

This approach builds on previous work studying defects in this system but provides a more complete set of structures and defects for the Sr alloyed system to assess Sr-defect interactions. Perfect $La_{2-x}Sr_xCoO_4$ is modeled at x = 0, 0.5, 1.0, 1.5 and 2.0 using supercells that have four formula units and 28 atoms. The supercells at x= 0.5, 1.0 and 1.5 are generated using the Special Quasi-random Structure (SQS) method [39] as implemented in the Alloy Theory Automated Toolkit (ATAT) [40] to simulate random occupations of La and Sr at A sites. Two and seven SQS structures are calculated at x= 1.0 and x= 0.5 and 1.5, respectively to explore the effect of different La and Sr configurations. For each perfect supercell structure, one O interstitial is introduced and all symmetrically distinct oxide and peroxide O interstitial sites are enumerated one by one. For all perfect and interstitial defected supercell structures, tilting of the octahedra is introduced while the overall Bravais lattice is kept tetragonal at the undefected lattice parameters and angles. For the undefected cell, structure relaxations are performed to find the equilibrium lattice constants of a and c with the only constrain of keeping the Bravais lattice tetragonal. All atom positions are also optimized. Overall, a large number of supercell structures and O interstitial sites with Sr concentrations covering the whole 0 to 2 range are each relaxed with multiple structural relaxation steps. Such a set of calculations normally takes large amount of manual labor but in this work it was reduced using the high-throughput automated workflow management implemented in the Materials Simulation Toolkit (MAST) [41, 42].

While this gives useful qualitative guidance, it could bias the results by missing stable Sr and defect arrangements. Therefore, here we should a more complete exploration of the bulk defect formation energetics, focusing on $La_{2-x}Sr_xCoO_4$. **Figure 54** shows the results of high throughput oxygen interstitial formation energies of bulk $La_{2-x}Sr_xCoO_4$. The energies are taken from the total energy an O interstitial containing bulk minus the total energy of the 28-atom $La_{2-x}Sr_xCoO_4$ perfect bulk at a

given x, and therefore the absolute number does not have a corresponding thermodynamic condition for oxygen at this stage of analysis. However, the energetic results shown in **Figure 54** provide stability trends of the two types of the O interstitials in bulk $La_{2-x}Sr_xCoO_4$ vs. Sr content, x.

Our results again confirm strong Sr doping concentration depedence for the oxygen ion interstitial in bulk $La_{2-x}Sr_xCoO_4$ over the range of Sr doping content, x=0.0-1.5, whereas the oxygen peroxide interstitial exhibits weak or almost no Sr doping concentration depedence. The weak dependence of the Sr interstitial above x≈1.5 is likely due to the Ni being fully oxidzed and the system reaching a relatively flat plateau where oxygen is not the redox active species. In addition, the multiple numbers within ~0.4 eV/O variation for x=0.5, 1.0, and 1.5 indicates coupling between A-site cation ordering and the oxygen interstitial formation energies is not a strong effect.

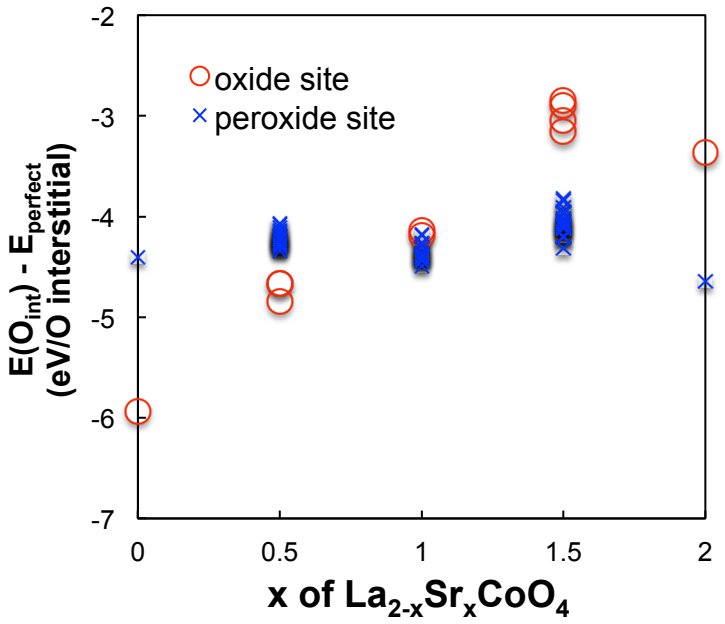

Figure 54. Oxygen interstitial formation energies of bulk $La_{2-x}Sr_xCoO_4$. Two oxygen interstitial species, oxygen ion interstitial (red) and oxygen peroxide interstitial (blue), were investigated. The energies do not have an absolute meaning at this stage but provide stability trend of the two O interstitial species in bulk $La_{2-x}Sr_xCoO_4$ vs. Sr content, x.

7.1.4 *Ab initio* surface oxygen adsorption and oxygen vacancy formation energies for $La_{2-x}Sr_xCoO_4$(x=0.5, 1.0, 1.5) and $La_{2-x}Sr_xNiO_4$ (x= 0.0, 0.5, 1.0) (001) AO Surfaces

Figure 55 shows the computed DFT (001) AO surface oxygen surface adsorption energies, $E(O_{ad})$s, as a function of the Sr content in $La_{2-x}Sr_xMO_4$ (M=Co and Ni) (001) AO terminated surface of the 9-layer symmetric (001) slabs (solid line with filled symbols), including surface adsorbed O^{2-} at the bridge site between two surface A-sites (red filled trangles) and surface adsorbed O^- bonded with a surface layer oxygen (O-O bond length ~ 1.5Å, green filled diamonds). For comparison, the two types of bulk oxygen interstitial formation energies, $E(O_{int})$s, for O^{2-} ion interstitial and O^- peroxide interstitial were also included (dashed lines with empty symbols). Our results suggest the surface adsorbed oxygens are more stable than their bulk oxygen interstitial analogs (*i.e.*, the surface

adsorbed O^{2-} vs. bulk O^{2-} ion interstitial and surface adsorbed O^{-} vs. bulk O^{-} peroxide interstitial) for the $La_{2-x}Sr_xCoO_4$ and $La_{2-x}Sr_xNiO_4$ that contain heavy Sr doping, *i.e.*, $La_{2-x}Sr_xCoO_4$ at x = 0.5, 1.0, and 1.5 and $La_{2-x}Sr_xNiO_4$ at x =0.5 and 1.0. In addition, the (001) AO surface adsorbed O^{-} peroxide is also found to be more stable than the adsorbed O^{2-} for $La_{2-x}Sr_xCoO_4$ at x > 0.5 and for $La_{2-x}Sr_xNiO_4$ at x ≥0.5.

Figure 56 shows predicted $La_{2-x}Sr_xCoO_4$ (x=0.5, 1.0, and 1.5) and $La_{2-x}Sr_xNiO_4$ (x=0.0, 0.5, and 1.0) surface oxygen adsorption energies at the fully Sr occupied (001) AO surface. It is seen that upon surface Sr segregation (full Sr substitution of surface layer A-sites), the adsorbed O^{-} peroxide stability is almost unaffected, while surface O^{2-} adsorption was further weakened at the (001) SrO surface.

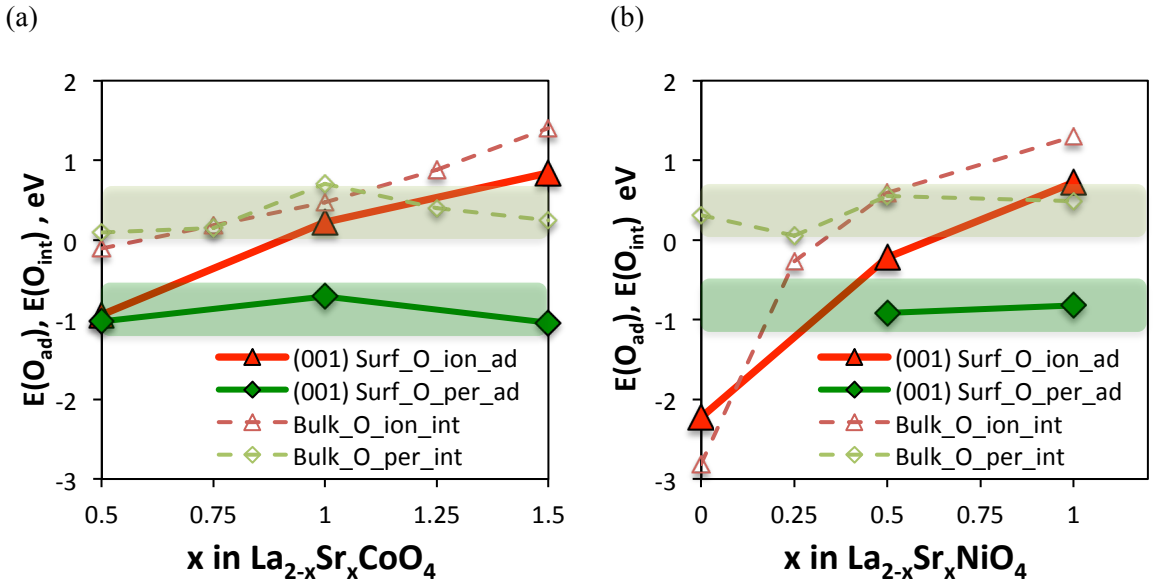

Figure 55. Predicted (a) $La_{2-x}Sr_xCoO_4$ (x=0.5, 1.0, and 1.5) and (b) $La_{2-x}Sr_xNiO_4$ (x=0.0, 0.5, and 1.0) surface oxygen adsorption energies: surface adsorbed O^{2-} at the bridge site between 2 surface A-sites, red filled trangles, and surface adsorbed O^{-} bonded with a surface layer oxygen (O-O bond length ~ 1.5Å, green filled diamonds) on the (001) AO surface. For comparison, the two types of bulk oxygen interstitial formation energies, $E(O_{int})$s, for O^{2-} ion interstitial and O^{-} peroxide interstitial, were also included (dashed lines with empty symbols). The shaded regions in the plots (light green for bulk and dark green for the surfaces) are to highlight the weak Sr dependence of the O^{-} interstitial stability.

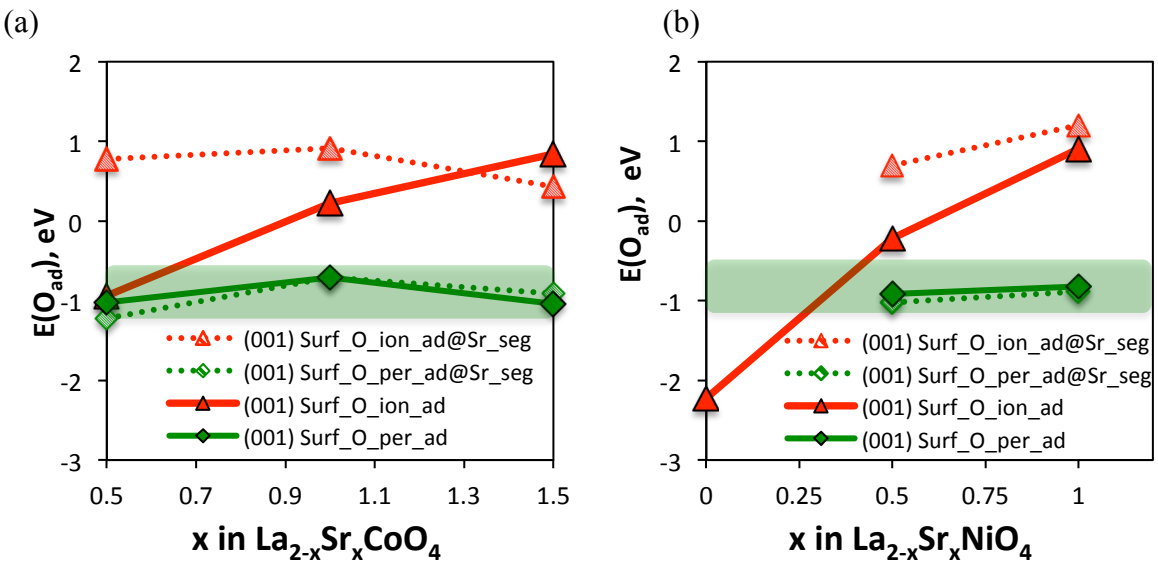

Figure 56. Predicted (a) $La_{2-x}Sr_xCoO_4$ (x=0.5, 1.0, and 1.5) and (b) $La_{2-x}Sr_xNiO_4$ (x=0.0, 0.5, and 1.0) surface oxygen adsorption energies at the fully Sr occupied (001) AO surface (shaded data points with dotted lines) for the surface adsorbed O^{2-} (red triangles) and surface adsorbed O^- (green diamonds). For comparison, surface adsorption energies of the adsorbed O^{2-} ion and O^- peroxide on the AO surface with the nominal bulk Sr content (same as those in **Figure 55**) were also included (solid lines with filled symbols). The shaded green region in the plots is to highlight the weak Sr dependence of the O^- interstitial stability.

Figure 57 shows the computed DFT bulk (empty sqaures) and (001) AO surface layer oxygen vacancie formation energies at the A-site Sr ccontent equalt to bulk (filled squares) and equal to 100% (shaded squares). Our results suggest the $La_{2-x}Sr_xCoO_4$ (x=0.5, 1.0, and 1.5) and $La_{2-x}Sr_xNiO_4$ (x=0.0, 0.5, and 1.0) (001) AO surface oxygen vacancy formation energies are close or comparable to their bulk, and upon surface Sr segregation (100% Sr occupation of surface layer A-sites), the surface oxygen vacancy formation energies are further decreased by 1~2 eV as compared to the bulk.

Overall, our results suggest that there is greater O^- peroxide stability adsorbed on the (001) AO surfaces than in the bulk $La_{2-x}Sr_xMO_4$ phase, and surface adsorbed O^- peroxide is more stable than surface adsorbed O^{2-} at heavy Sr doping. Surface Sr segregation was demonstrated to result in almost no influence on the stability of surface adsorbed O^- peroxide species, consistent with the trend of the bulk O^- peroxide interstitial stability vs. Sr content, while oxygen vacancy formation at the (001) AO surfaces strongly depends on the surface Sr content (surface $E(O_{vac})$s lowered by 1~2 eV at the SrO surface as compared to the AO surfaces at the bulk Sr content). These trends will support building surface models for understanding surface stability and surface exchange mechanisms of the $La_{2-x}Sr_xMO_4$ phases.

(a) (b)

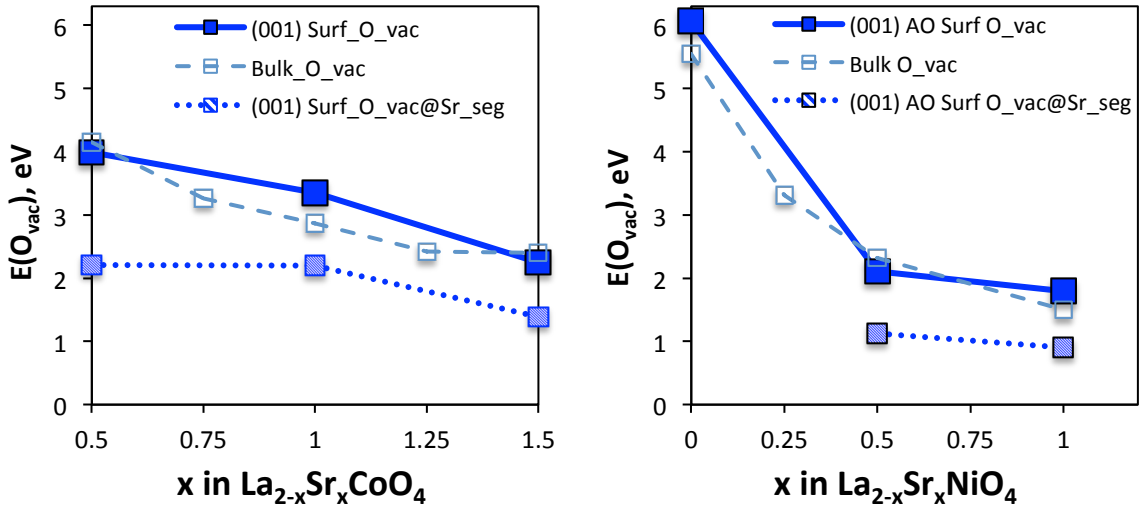

Figure 57. Predicted (a) $La_{2-x}Sr_xCoO_4$ (x=0.5, 1.0, and 1.5) and (b) $La_{2-x}Sr_xNiO_4$ (x=0.0, 0.5, and 1.0) bulk (empty sqaures) and (001) AO surface layer oxygen vacancies formation energies at the A-site Sr ccontent equalt to bulk (filled squares) and equal to 100% (shaded squares).

7.1.5 Summary

Energetics of bulk oxygen defects (O_{vac} and two types of O_{int}s) in $La_{2-x}Sr_xMO_4$ (M=Co, Ni, and Cu) bulk and surface oxygen adsorption as well as oxygen vacancy formation on the (001) AO surfaces of $La_{2-x}Sr_xCoO_4$ and $La_{2-x}Sr_xNiO_4$ were investigated. Our results suggest:

- O^{2-} ion interstitial is more stable than the O^- peroxide interstitial in La_2MO_4 bulk (M=Co, Ni, and Cu).
- Stability of O^- peroxide interstitial is almost independent of Sr content and becomes more stable than the O^{2-} ion interstitial for $La_{2-x}Sr_xMO_4$ at $x \geq \sim 0.75$ for $La_{2-x}Sr_xCoO_4$, $x \geq \sim 0.5$ for $La_{2-x}Sr_xNiO_4$, and $x \geq 0.25$ for $La_{2-x}Sr_xCuO_4$.
- The (001) AO surface adsorbed O^- peroxide is predicted to be more stable than the adsorbed O^{2-} for $La_{2-x}Sr_xCoO_4$ at $x > 0.5$ and for $La_{2-x}Sr_xNiO_4$ at $x \geq 0.5$. Upon surface Sr segregation (full Sr substitution of surface layer A-sites), the adsorbed O^- peroxide stability is shown to be almost unaffected, while surface O^{2-} adsorption was further weakened at the (001) AO (SrO) surface.
- The $La_{2-x}Sr_xCoO_4$ (x=0.5, 1.0, and 1.5) and $La_{2-x}Sr_xNiO_4$ (x=0.0, 0.5, and 1.0) (001) AO surface oxygen vacancy formation energies are found to be close to their bulk. Upon surface Sr segregation (full Sr substitution of surface layer A-sites), the surface oxygen vacancy formation energies are further decreased by 1~2 eV as compared to the bulk.

7.2 Kinetics of Oxygen Surface Exchange on Epitaxial Ruddlesden-Popper-Type Thin Films and Correlations to First-Principles Descriptors

Through alignment of theoretical modeling with experimental measurement of oxygen surface exchange kinetics on well-defined (001) oriented $La_{2-x}Sr_xMO_{4+\delta}$ (M= Co, Ni, Cu) thin films, we demonstrate the capability of the bulk O 2p-band centers to correlate with oxygen surface exchange kinetics of the (001)-oriented Ruddlesden-Popper oxide (RP_{214}) thin films. In addition, we demonstrate that the bulk O 2p-band centers can correlate with the experimental activation energies for bulk oxygen transport and oxygen surface exchange of both the RP_{214} and the perovskite polycrystalline materials in the literature, indicating effectiveness of the bulk O *2p*-band centers in describing the associated energetics and kinetics. We propose that the opposite slopes of the bulk O *2p*-band center correlations between the RP_{214} and the perovskite materials are due to the intrinsic mechanistic differences of their oxygen surface exchange kinetics bulk anionic transport.

7.2.1 Correlation between the bulk and (001) AO surface layer oxygen 2p band centers of $La_{2-x}Sr_xMO_4$ (M=Co, Ni, and Cu)

Figure 67 shows the computed O 2p-band centers of the (001) surface layers for the $La_{2-x}Sr_xMO_4$ (M=Co, Ni, and Cu) phases vs. the bulk O 2p-band centers, including the top surface layer (blue circles), the second surface layer (red circles), and the top two surface layers (green circles). Since the symmetry and local bonding of transition metal-oxygen (TM-O) environment in the AO layer and in the BO_2 layer are different (*e.g.,* oxygen in the AO layer contains only one long TM-O bond while oxygen in the BO_2 layer contains two short TM-O bonds), the computed O 2p-band centers (relative to the Fermi level, E_{Fermi}) of the AO surface layers for the investigated RP-phases were shown to be 1~1.5 eV higher than those of the BO_2 sub-surface layers. Nonetheless, the correlations consistently exist between the averaged bulk O 2p-band centers and a defined surface layer(s) of the $La_{2-x}Sr_xMO_4$ (M=Co, Ni, and Cu) phases, either the top surface layer, the second surface layer, or the top two surface layers, as shown in **Figure 67**. Such universal bulk vs. surface O 2p-band correlations suggest electronic structure of a defined surface termination for a series of $La_{2-x}Sr_xMO_4$ (M=Co, Ni, and Cu) materials can still be described by the bulk O 2p-band center as long as surface orientation of the materials remains the same.

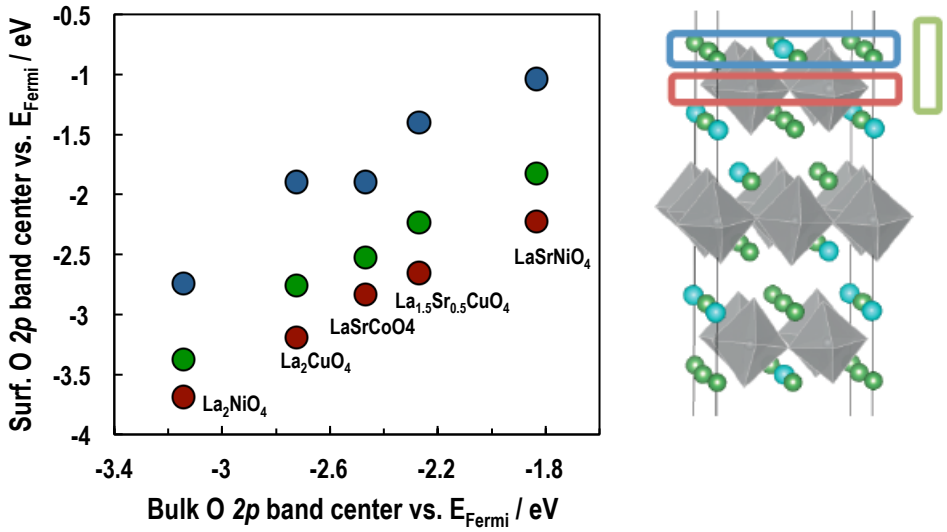

Figure 58. The computed O 2p-band centers of the (001) surfaces for the RP-214 phases-the top layer (blue circles), the second layer (red circles), and the top two surface layers (green circles) vs. the bulk O 2p-band centers. A schematic shown on the right hand side of the figure highlights the surface layers that were computed for the O 2p-band centers (same color as the data points).

7.2.2 Correlations between the bulk and (001) AO surface oxygen defect and adsorption energetics vs. bulk oxygen 2p band centers of $La_{2-x}Sr_xMO_4$ (M=Co, Ni, and Cu)

To further test the capability of the bulk O 2p-band center in describing bulk and surface oxygen defect and oxygen adsorption energetics, we plotted the bulk oxygen vacancy (green triangles), O^{2-} interstitial (blue diamonds) and O^- interstitial (red squares) formation energies vs. the computed bulk O 2p-band center of a series of $La_{2-x}Sr_xMO_4$ (M=Co, Ni, and Cu) phases, as shown in **Figure 68**(a), and surface oxygen vacancy formation and oxygen adsorption (adsorbed O^{2-} and O^-) energies vs. the computed bulk O 2p-band center of $La_{2-x}Sr_xMO_4$ as shown in **Figure 68**(b). These simulated RP materials were chosen based on the (001) oriented RP thin films grown by the MIT team and the corresponding surface exchange k^qs of the epitaxially grown (001) oriented films were also reported in our previous quarterly report. Our results suggest that both the bulk and surface oxygen defect formation and surface oxygen adsorption energies correlate with the bulk O 2p-band centers in a similar fashion. Furthermore, the opposite slope of the oxygen vacancy formation vs. the bulk O 2p-band centers as compared to that of the O^{2-} interstitial formation in the bulk or O^{2-} adsorption on the surface is consistent with the opposite charge transfer characteristics of the two types of the oxygen defect formation: generation of electrons in oxygen vacancy formation while generation of holes in O^{2-} interstitials formation or surface O^{2-} adsorption). That the almost flat slope of O^- interstitial formation in the bulk and O^- adsorption on the surface is also in good agreement with no or very little charge transfer associated with formation such peroxide oxygen species, *i.e.*, formation of O^- bound with an bulk or surface lattice oxygen causes no oxidation in the system: ½ O_2(gas)+O^{2-} (lattice) → O_2^{2-}. Overall, the existences of the correlations between the bulk as well as the surface oxygen defect formation/oxygen adsorption and the computed bulk O 2p-band centers for a series of $La_{2-x}Sr_xMO_4$ phases suggest the averaged bulk O 2p-band centers can be used to describe oxygen defect energetics for a specified surface orientation of the RP_{214} phases.

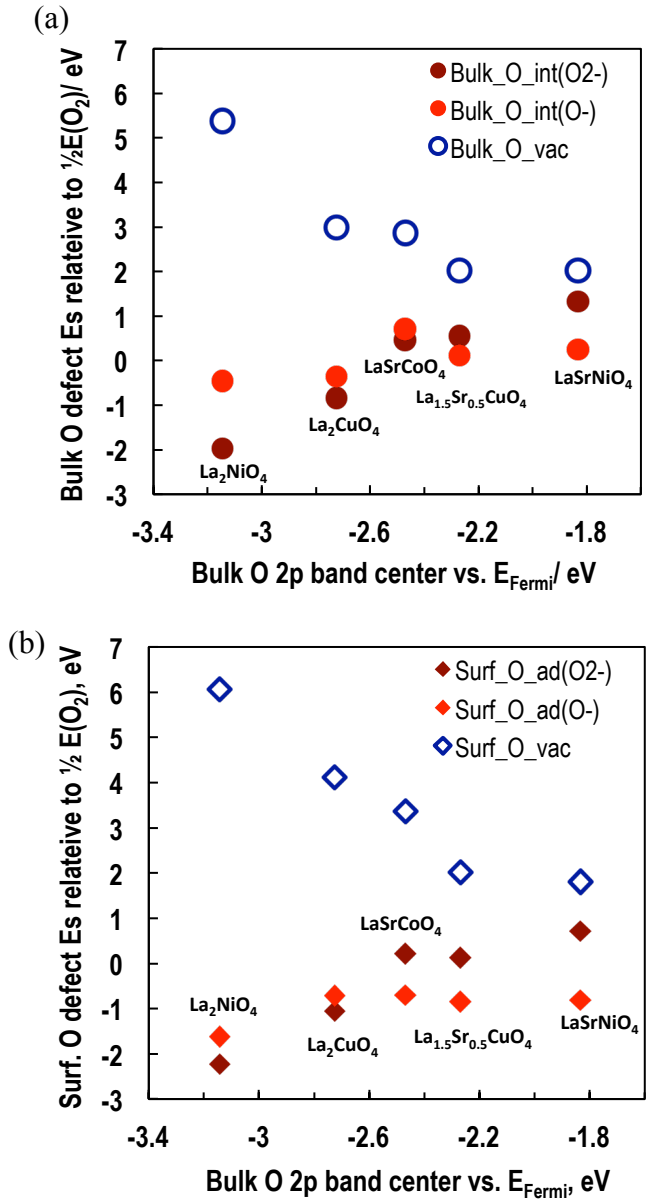

Figure 59. (a) The computed bulk oxygen defect energetics for oxygen vacancy, O^{2-} interstitial, and O^{-} interstitial vs. the bulk O 2p-band centers vs. E_{Fermi}. (b) The computed surface oxygen vacancy, surface adsorbed O^{2-}, and O^{-} vs. the bulk O 2p-band centers vs. E_{Fermi}.

7.2.3 Correlations between the experimentally measured k^q of the (001) oriented thin films vs. bulk oxygen 2p band centers for $La_{2-x}Sr_xMO_4$ (M=Co, Ni, and Cu)

Given the bulk O 2p-band centers were shown to correlate with the surface oxygen defect formation and adsorption energies for a defined surface orientation of various RP_{214} systems, which are in general considered to be key energetics for oxygen diffusion, oxygen surface exchange, and oxygen reduction reaction kinetics[43], we further examined correlations between the measured

experimental oxygen surface exchange k^q at T=550 C and P(O_2)=1 atm as shown in **Figure 60**. Indeed, our results revealed that there also existed a correlation between the experimentally measured surface exchange k^q for the (001) oriented epitaxial $La_{2-x}Sr_xMO_4$ films and their computed bulk O 2p-band centers. In addition, the slope of the correlation was found to be negative while the slope of the surface exchange k^*/k^q reported for the perovskite materials was positive[44]. It is hypothesized that the opposite k^*/k^q vs. the O 2p-band slopes between the RP_{214} phases and the perovskite materials may be associated with their distinct oxygen surface exchange mechanisms of the investigated RP materials (mediated by with oxygen interstitial related mechanisms) under the tested conditions

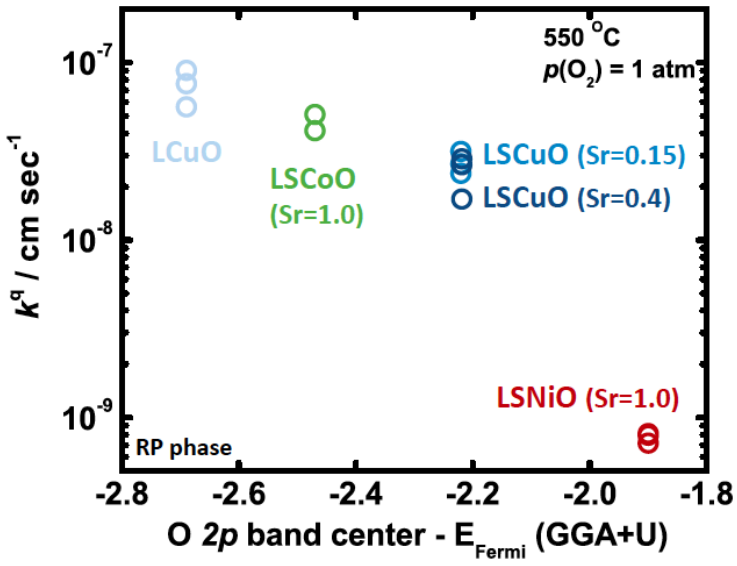

Figure 60. The experimentally measured oxygen surface exchange k^q of the RP phases (LCuO:La_2CuO_4, LSCoO(Sr=1.0):$LaSrCoO_4$, LSCuO(Sr=0.15):$La_{1.85}Sr_{0.15}CuO_4$, LSCuO(Sr=0.4):$La_{1.6}Sr_{0.4}CuO_4$, and LSNiO(Sr=1.0):$LaSrNiO_4$) at T=550 C and P(O_2)=1 atm vs. the bulk O 2p band centers vs. E_{Fermi}.

(T=550 C and P(O_2)=1 atm), as compared to the perovskite materials (mediated by oxygen vacancies)[44]. While our initial results indicate a correlation exists between the oxygen surface exchange rate and the bulk electronic structure descriptor – O 2p-band center, detailed analysis and further works are still needed to understand the exact surface reaction mechanisms of a wider range of the RP phases, including the role of the charge transfer processes which has been proposed as the rate-limiting step for the electrode surface reactions of some RP phase materials[45, 46], and how the anisotropy effect influences surface exchange activities[47].

7.2.4 Correlations between the bulk O 2p-band and experimental activation barriers of D* and K* for the RP_{214} and SOFC perovskite materials in the literature

Figure 61(a) shows the experimentally extracted activation barriers of D* and k* of the polycrystalline RP_{214} reported in the literature[48-50] vs. the computed bulk O 2p-band centers, in which a good liner correlation is observed. The same analysis was also performed on the SOFC perovskite materials, where the bulk O 2p-band centers were taken from those reported in Ref. [44]

and from that in Ref. [51] for $La_{0.5}Sr_{0.5}CoO_{3-\delta}$. The experimental activation barriers of D* and k* were taken from those summarized in the work by Tarancon *et al.*[43] (see Table 1 of Ref. [43]), except for those of $La_{0.6}Sr_{0.4}Co_{0.2}Fe_{0.8}O_{3-\delta}$, which were instead taken from Ref. [8] since the data adopted in Ref. [43] is from measurements obtained using gadolinia doped ceria electrolyte rather than yttria doped zirconia. Due to intrinsic material instability of $Ba_{0.5}Sr_{0.5}Co_{0.8}Fe_{0.2}O_{3-\delta}$[52], an additional activation barrier data for k* of $Ba_{0.5}Sr_{0.5}Co_{0.8}Fe_{0.2}O_{3-\delta}$ from Ref. [53] is also included, as there is a large difference in the activation barriers reported in the literature for the oxygen surface exchange coefficients of $Ba_{0.5}Sr_{0.5}Co_{0.8}Fe_{0.2}O_{3-\delta}$, *e.g.* 1.76 eV in Ref. [54] vs. 0.66 eV in Ref. [53]. The overall results are shown in Figure 61(b), where a good linear correlation is also observed between the calculated bulk O 2p-band centers vs. the activation barriers of D* and k* of the perovskite materials, whereas the activation barrier of k* of $Ba_{0.5}Sr_{0.5}Co_{0.8}Fe_{0.2}O_{3-\delta}$, adopted in Ref. 2 is found to be an outlier of the correlation. Interestingly, the slopes of the activation barriers vs. bulk O 2p-band correlations of the RP_{214} and the perovskite materials were shown to be opposite, supporting their distinct mechanistic nature of oxygen surface exchange and bulk oxygen transport between the two different material systems. Overall, our results demonstrated the effectiveness of the electronic structure descriptor – the bulk O 2p-band centers - in describing surface exchange and oxygen diffusion rates through the experimentally extracted activation barriers. Our results suggest search and design of the active RP_{214} phases with direct or indirect oxygen interstitial mediated mechanisms should seek for the materials with lower bulk O 2p-band centers relative to the Fermi level, in contrast to the active SOFC perovskite materials which have the higher O 2p-band centers relative to the Fermi level[44]. On the other hand, the experimental activation barriers of k* and D* for La_2CoO_4 shown in Figure 4(a) are already close to 0, and extrapolation of the O 2p-band correlation to go beyond La_2CoO_4 for the RP_{214} materials will predict that these RP_{214} materials have negative activation barriers for their bulk oxygen transport and oxygen surface exchange, which indicates issues associated with material instability, since the energies of the transition states will become lower than those of the reactants. Indeed, it was reported by Munnings *et al.*[48] that no k* and D* data were obtained for temperatures above 684°C for the pure $La_2CoO_{4+\delta}$ sample due to the relative instability of this material at elevated temperatures in air, which leads to decomposition into $LaCoO_3$ and La_2O_3 at temperatures above ~700° C. Although such a coupling between material catalytic activity and material instability is similar to the SOFC perovskite materials[44], where the more active SOFC perovskites are also less stable, the opposite trends (slopes) of oxygen surface exchange activity vs. the bulk O 2p-band centers (relative to the Fermi level) between the RP_{214} phase and the perovskites make distinction in how their intrinsic electronic structure properties that are associated with their material instability and the active oxygen defects that directly govern or indirectly influence on the kinetics of bulk anionic transport and oxygen surface exchange.

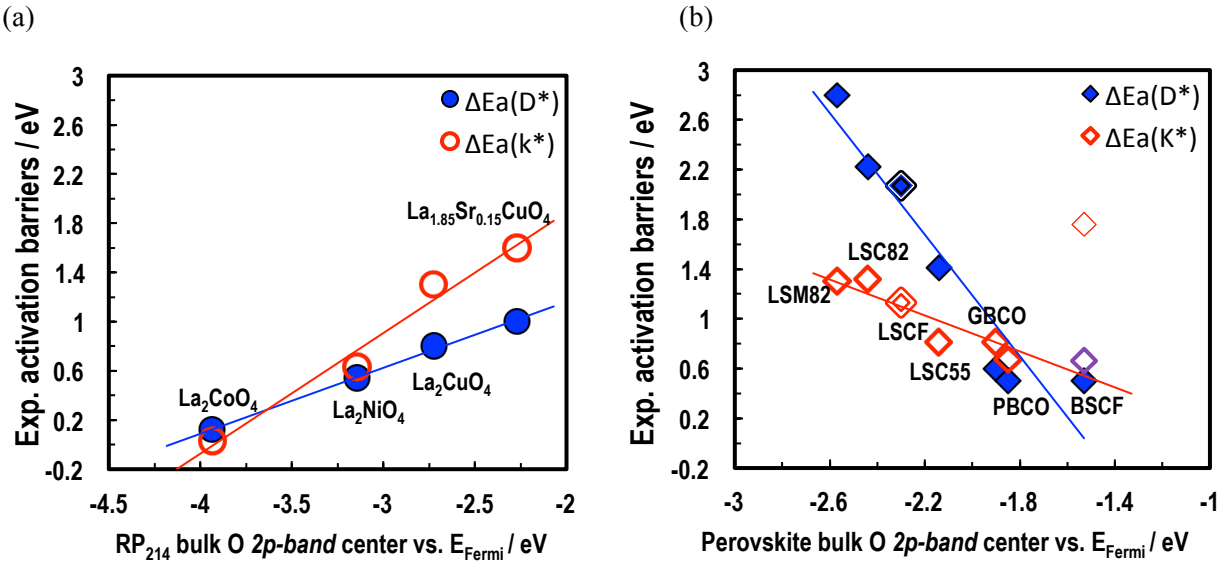

Figure 61. (a) The activation barriers (ΔE_a) for bulk oxygen transport (D*) and oxygen surface exchange (k*) for $La_2CoO_{4+\delta}$ [48], La_2NiO_4 [49], La_2CuO_4 [50] and $La_{1.85}Sr_{0.15}CuO_4$ [50] vs. the computed bulk oxygen *2p* band centers; (b) the activation barriers (ΔE_a) for bulk oxygen transport (D*, blue filled diamonds) and oxygen surface exchange (k*, red empty diamonds) summarized in Table 1 of Ref. [43] for $La_{0.8}Sr_{0.2}MnO_{3+\delta}$ (LSM82), $La_{0.8}Sr_{0.2}CoO_{3-\delta}$ (LSC82), $La_{0.5}Sr_{0.5}CoO_{3+\delta}$ (LSC55), $GdBaCo_2O_{6-\delta}$ (GBCO), $PrBaCo_2O_{6-\delta}$ (PBCO), and $Ba_{0.5}Sr_{0.5}Co_{0.8}Fe_{0.2}O_{3-\delta}$ (BSCF) vs. the computed bulk O 2p band centers collected from the previous works[44, 51] (LSC55 from Ref. [51]). For $La_{0.6}Sr_{0.4}Co_{0.2}Fe_{0.8}O_{3-\delta}$, both activation barriers of k* and D* (symbols with double lines) were taken from Ref. [8] instead of Ref. [43] (where the measurements were performed with gadolinia doped ceria electrolyte instead of yittria doped zirconia). Furthermore, an additional data of the activation barrier of the BSCF surface exchange coefficient from Ref. [53] (empty purple diamond) to contrast the large difference between the results of Ref. [43] vs. Ref. [53]. Overall, excluding the outlier of the ΔE_a for the BSCF k* from Ref. [43] , a clear correlation is observed for both ΔE_as of the k* and D* vs. the calculated bulk O 2p band centers.

7.2.5 Summary

Despite anisotropic nature in the electronic/ionic transport properties of the RP phases, by investigating epitaxial thin films with a well-defined surface orientation, trends were revealed between the bulk electronic structure descriptor , the O 2p-band center, and energetics of oxygen defects (O_{vac} and two types of O_{int}s/O_{ad}s) in bulk and on the (001) AO surfaces of $La_{2-x}Sr_xMO_4$ (M=Co, Ni, and Cu). In addition, the experimentally measured surface exchange coefficients k^qs of the (001) oriented RP epitaxial thin films were also shown to be correlated with the computed bulk O 2p-band centers. The correlation of the surface exchange k^qs vs. the computed bulk O 2p band centers of the investigated $La_{2-x}Sr_xMO_4$ (M=Co, Ni, and Cu) phases exhibited an opposite slope as compared to that reported for the perovskite systems, which were hypothesized to be associated with different active oxygen defects for their surface exchange kinetics (oxygen interstitials for the RP phases and oxygen vacancies for the perovskites). Further efforts are still needed to obtain detailed mechanistic understanding, including the role of factors such as material anisotropy, lattice dynamics *etc.*, for the oxygen kinetics of the RP_{214} phases. Such understandings, combined with the O 2p-band center descriptor, offer exciting opportunities for targeted search and develop of RP_{214} materials for SOFC cathodes.

7.3 *Ab initio* Surface Stability Analysis of $LSCF_{113}$ and $LaSrCoO_{4\pm\delta}$

The $LSCF_{113}$ surface stability is of significant interests in SOFC cathode performances as the ORR kinetics are strongly influenced by surface chemistry and degradation. In this work, we performed *ab initio* thermodynamic analysis to investigate surface stability of (001) AO and BO_2 at various Sr/La and Co/Fe composition relative to the bulk LSC_{113}, LSF_{113}, and $LSCF_{113}$ at a given relevant $P(O_2)$ and temperature to SOFC conditions, in order to understand stability of LSC_{113}, LSF_{113}, $LSCF_{113}$ surfaces and further model ORR reactions on the stable surfaces relevant to the SOFC conditions.

7.3.1 *Ab Initio* Modeling Approaches

Density functional theory (DFT) based *ab-initio* calculations are performed using Vienna *Ab-initio* Simulation Package (VASP), including the GGA+U (U_{eff} = 4.0 eV and 3.3 eV for the 3*d* electrons of Fe and Co, respectively). Bulk binary oxides (La_2O_3, SrO, Fe_2O_3, CoO, and Co_3O_4), perovskites (LSC_{113}, $LSCF_{113}$), and the Ruddlesden Popper phase (LSC_{214}) are fully relaxed for each structure. The energy cutoff was set to 450 eV and the Brillouin zone was sampled by a Monkhorst–Pack k-point mesh of 4×4×4 for a primitive ideal perovskite unit cell. Table 5 summarizes our calculated oxide formation energies (formation reactions of the binary oxides forming perovskites and the 214 Ruddlesden-Popper phase) vs. experimentally measured oxide formation enthalpies from the literature[55-57], and it is seen that the differences between the theoretical and experimental results are within the targeted energy accuracy of ±0.2 eV per formula unit for the relevant oxide compounds in this work.

LSC_{113}, LSF_{113}, and $LSCF_{113}$ surface calculations are performed using the 9-layer 2×2 symmetric (001) AO terminated and BO_2 terminated slabs with the central 5 layers fixed to a composition close to the bulk LSC_{113}, LSF_{113}, and $LSCF_{113}$ and the top two and bottom 2 layers varying the La/Sr and Co/Fe composition ($La_{1-x}Sr_xCo_{1-y}Fe_yO_3$ with x=0, 0.25, 0.5, 0.75, 1 and y=0, 0.25, 0.5, 0.75, 1), as illustrated in Figure 62. A total of 10 configurations (5 for the (001) AO surfaces and 5 for the (001) BO_2 surfaces) for LSC_{113} and LSF_{113}, and a total of 50 configurations (25 for the (001) AO surfaces and 25 for the (001) BO_2 surfaces) for $LSCF_{113}$, are calculated based on the 9-layer 2×2 symmetric slab model for the surface stability analysis.

Table 5. The calculated *ab initio* oxide formation energies vs. the experimentally measured oxide formation enthalpies from the literature [55-57] for the LSF_{113}, LSC_{113}, and LSC_{214} perovskites related compounds.

	Reactants in the Oxide Formation Reaction	DFT (eV/F.U.)	Exp. (eV/F.U.)	Difference (eV/FU)
$LaFeO_3$	La_2O_3, Fe_2O_3	-0.527	-0.669 [55]	0.142
$La_{0.75}Sr_{0.25}FeO_3$	La_2O_3, SrO, Fe_2O_3, O_2	-0.490	-0.652* [55]	0.162
$La_{0.5}Sr_{0.5}FeO_3$	La_2O_3, SrO, Fe_2O_3, O_2	-0.598	-0.664 [55]	0.066
$La_{0.25}Sr_{0.75}FeO_3$	La_2O_3, SrO, Fe_2O_3, O_2	-0.746	-0.706* [55]	-0.040
$LaCoO_3$	La_2O_3, CoO, O_2	-1.000	-1.115 [56]	0.115
$La_{1.25}Sr_{0.75}CoO_4$	La_2O_3, SrO, CoO, O_2	-1.009	-1.047 [57]	0.038
$LaSrCoO_4$	La_2O_3, SrO, CoO, O_2	-1.129	-1.219 [57]	0.090
$La_{0.75}Sr_{1.25}CoO_4$	La_2O_3, SrO, CoO, O_2	-1.417	-1.304 [57]	-0.113

*value from interpolation of the data between the two nearest Sr concentration in Ref. [55].

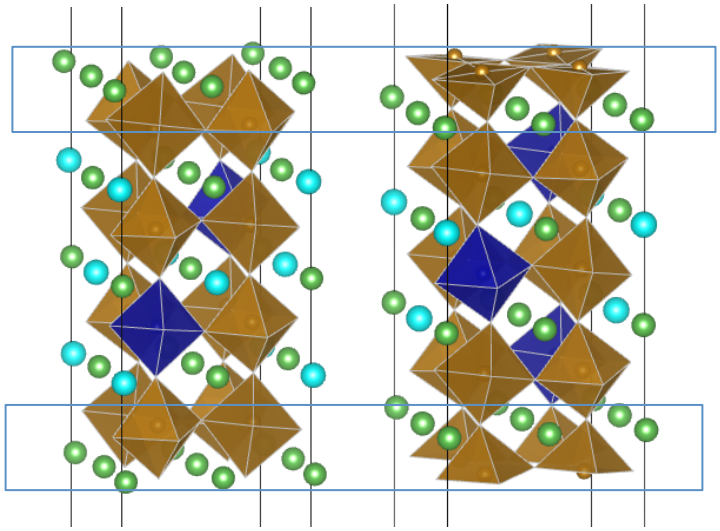

Figure 62. The adopted LSC_{113}, LSF_{113}, and $LSCF_{113}$ (001) slab models for the *ab initio* surface thermodynamic analysis. Green and light blue spheres represent La and Sr, while brown and deep blue polyhedral represent local Fe-O and Co-O environment, respectively. The top (and bottom) two surface layers, where La/Sr and Co/Fe compositions ($La_{1-x}Sr_xCo_{1-y}Fe_yO_3$ with x=0, 0.25, 0.5, 0.75, 1 y=0, 0.25, 0.5, 0.75, 1) are varied, are specified by the rectangle frames. The rest (central) part of the slabs are fixed to a composition close to $La_{0.75}Sr_{0.25}FeO_3$, $La_{0.75}Sr_{0.25}CoO_3$, and $La_{0.625}Sr_{0.375}Fe_{0.75}Co_{0.25}O_3$. A total of 10 configurations (5 for the (001) AO surfaces and 5 for the (001) BO_2 surfaces) for LSC_{113} as well as LSF_{113}, and a total of 50 configurations (25 for the (001) AO surfaces and 25 for the (001) BO_2 surfaces) are calculated based on the 9-layer 2×2 symmetric slab model for the surface stability analysis.

$LaSrCoO_4$ surface calculations are performed using the 9-layer 2×2 symmetric (001) AO terminated and 8-layer (100) A_2BO_4 terminated slabs with the top and bottom surface layers varying the A-site Sr concentration and the rest of the slab composition fixed to $LaSrCoO_4$, as illustrated in Figure 63. A total of 6 LSC_{214} (001) and (100) slab configurations (3 Sr/La compositions (x_{Sr} = 0.5, 0.75, and 1.0) for the A-site of the top and bottom surface layers of the (001) AO terminated slabs and 3 Sr/La compositions (x_{Sr} = 0.5, 0.75, and 1.0) for the A-site of the top and bottom surface layers of the (100) A_2BO_4 terminated slabs) are calculated for the surface stability analysis.

(a) 9-layer (001) AO slab (b) 8-layer (100) A_2BO_4 slab

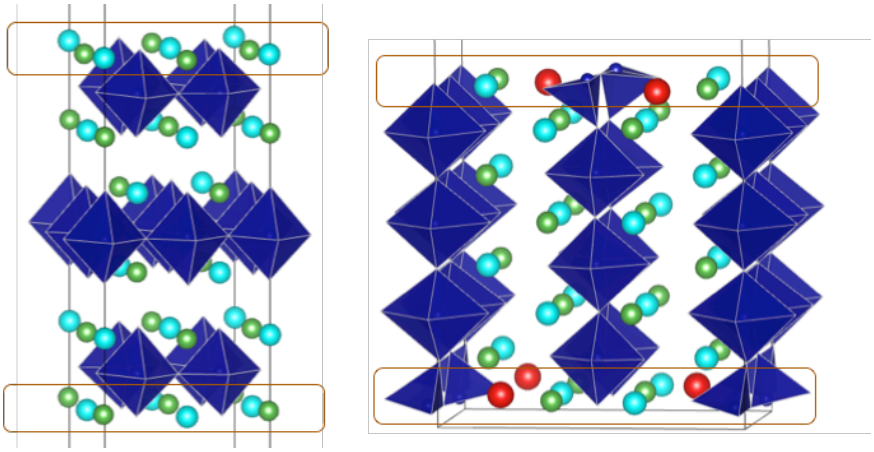

Figure 63. The adopted $LaSrCoO_4$ (a) 9-layer (001) AO and (b) 8-layer (100) A_2BO_4 slab models (after relaxation) for the *ab initio* surface thermodynamic analysis. Green and light blue spheres represent La and Sr, while deep blue polyhedral represent local Co-O environment, respectively. Local surface relaxation of the (100) A_2BO_4 slab introduces rearrangement of the surface Co-O square pyramidal configuration: a surface O (as shown in red) is displaced with an elongated Co-O bond (>2.8 Å) to form Co-O tetrahedral while the La/Sr-O bond is shortened (from ~ 2.5 Å to 2.2~2.4 Å). The top and bottom surface layers, where La/Sr compositions are varied, are specified by the rectangle frames. The rest (central) part of the slabs is fixed to the $LaSrCoO_4$ composition. A total of 6 configurations (3 for the (001) AO surfaces with surface layer Sr = 0.5, 0.75, and 1.0 and 3 for the (100) A_2BO_4 surfaces with the surface layer Sr = 0.5, 0.75, and 1.0) for LSC_{214} are calculated for the surface stability analysis.

7.3.2 *Ab Initio* Thermodynamic Modeling of $La_{1-x}Sr_xCo_{1-y}Fe_yO_3$ (001) Surface Stability

7.3.2.1 Ab Initio Surface Thermodynamic analysis

Surface stability analysis is performed using the following equation for surface energy, Γ_i:

$$\Gamma_i = \frac{1}{2A_s}\left[(E^{slab} - E^{bulk}) - N_O \cdot \Delta\mu_O(T,p) - (\sum_{j=La,Sr,Fe,Co}^{j-1} N_j \cdot \Delta\mu_j) - N_R \Delta\mu_R^{bulk}\right]$$

Eqn. 10

where A_s is the surface area of the simulated 9-layer 2×2 slab (a factor of 2 in front of A_s is to account for two surface terminations in the symmetric slabs), E_{total}^{slab} is the total energy of the slab,

$\Delta\mu_O(T,p)$ is the chemical potential of oxygen referenced to the O_2 gas phase at the standard condition (room temperature and 1 atm $P(O_2)$), T is temperature, p is the partial pressure of oxygen. The oxygen partial pressure dependence in the chemical potential of oxygen, $\Delta\mu_O(T,p)$, can be included based on the $\frac{kT}{2}\cdot Ln(p)$ term and here we take into account the vibrational free energy contribution of $\frac{1}{2}O_2(gas)+2e^-\rightarrow O^{2-}(oxide)$ for all the oxides with an Einstein temperature = 500 K in the Einstein model[33, 38]. We note that within the targeted energy accuracy of ±0.2 eV per formula unit, changing this Einstein temperature value by 50% in either direction from 250 to 750 K does not qualitatively impact our major conclusions[33, 38]. N_j and N_R are the numbers of atoms in the remaining part of the 9-layer symmetric slab after subtracting the number atoms in the 2×2×2 $LSCF_{113}$ bulk (5 La, 3 Sr, 2 Co, 6 Fe, and 24 O atoms), j denotes the three chosen constituents for their corresponding chemical potential conditions in the form of binary oxides, and R denotes the remaining constituent that is not among the specified j chemical potentials, which is set by the total energy of $LSCF_{113}$ and the chemical potentials of the specified constituents. For the chemical potentials of La, Sr, Co, and Fe in the oxide form of La_2O_3, SrO, Fe_2O_3, and Co_3O_4, $\Delta\mu_{La}$, $\Delta\mu_{Sr}$, $\Delta\mu_{Fe}$, and $\Delta\mu_{Co}$, chemical potentials are defined as the following:

$$\Delta\mu_{La}(T,p)=\frac{1}{2}[E^{ab\ initio}_{La_2O_3}-3\cdot(\frac{1}{2}E^{corr}_{O_2}+\Delta\mu_O(T,p)] \quad \textbf{Eqn. 11}$$

$$\Delta\mu_{Sr}(T,p)=E^{ab\ initio}_{SrO}-(\frac{1}{2}E^{corr}_{O_2}+\Delta\mu_O(T,p) \quad \textbf{Eqn. 12}$$

$$\Delta\mu_{Co}(T,p)=\frac{1}{3}[E^{ab\ initio}_{Co_3O_4}-4\cdot(\frac{1}{2}E^{corr}_{O_2}+\Delta\mu_O(T,p)] \quad \textbf{Eqn. 13}$$

$$\Delta\mu_{Fe}(T,p)=\frac{1}{2}[E^{ab\ initio}_{Fe_2O_3}-3\cdot(\frac{1}{2}E^{corr}_{O_2}+\Delta\mu_O(T,p)] \quad \textbf{Eqn. 14}$$

where $E^{ab\ initio}_{La_2O_3}$, $E^{ab\ initio}_{SrO}$, $E^{ab\ initio}_{Co_3O_4}$, and $E^{ab\ initio}_{Fe_2O_3}$ are the *ab initio* total energy of La_2O_3, SrO, Co_3O_4, and Fe_2O_3 normalized as per formula unit, and $E^{corr}_{O_2}$ is the *ab initio* total energy of O_2 molecule with a correction from fitting to experimental oxide formation enthalpies at room temperature[33]. When the chemical potentials of three metal constituents of $LSCF_{113}$ are specified by the chosen lower order oxides (e.g. $\Delta\mu_{La},\Delta\mu_{Sr},\Delta\mu_{Fe}$) at a given T and p (which defines $\Delta\mu_O(T,p)$), the chemical potential of the remaining constituent (e.g. $\Delta\mu_{Co}$) can be derived from:

$$\Delta\mu^{bulk}_{Co}(LSCF_{113})=(E^{bulk}-5\cdot\Delta\mu_{La}-3\cdot\Delta\mu_{Sr}-6\cdot\Delta\mu_{Fe}-24\cdot\Delta\mu_O(T,P))/2 \quad \textbf{Eqn. 15}$$

With the defined chemical potentials of the constituents for $LSCF_{113}$, the surface energy can be obtained through Eqn. 10.

7.3.2.2 Ab Initio Predictions for LSC_{113} and $LSCF_{113}$ (001) Surface Stability

Figure 64 shows the contour plots for the LSC_{113} stable surface composition vs. chemical potential of metals (here we chose μ(Sr) in SrO/LSC_{113} equilibrium and μ(Co) in Co_3O_4/LSC_{113} equilibrium as the metal chemical potential references) within the stability boundary of bulk LSC_{113} in equilibrium with La_2O_3, SrO, Co_3O_4, $LaCoO_3$, and $SrCoO_{2.5}$ based on the most stable surface energy of the investigated 10 LSC_{113} slab configurations at (a) T= 550ºC(823K) and $P(O_2)$=1.0 atm (b) T= 550ºC(823K) and $P(O_2)$= 50 atm and (c) T= 550ºC(823K) and $P(O_2)$=0.05 atm. We note the boundary lines in Figure 64 are for LSC_{113} bulk stability, while the contour colormap represents the most stable surface configurations among the investigated DFT slab models. The stable region shown in Figure 64 can be considered as a lower bound of bulk LSC_{113} stability, *i.e.,* including further more stable compounds only truncates the bulk stability region. Surface stability contour plots are then derived based on the calculated surface energy of the investigated slab configurations using the bulk Sr and Co metal chemical potential grid within the triangle region (stability boundaries vs. the binary oxides) shown in Figure 64.

(a)

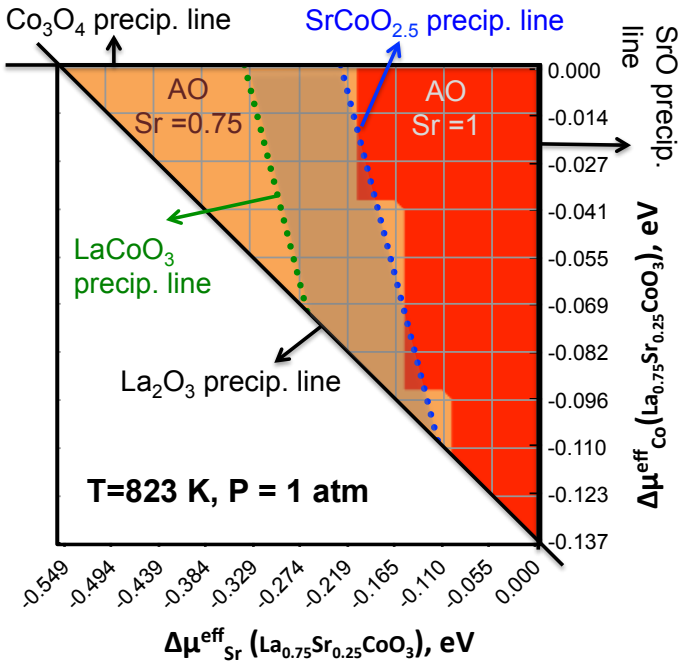

(b)

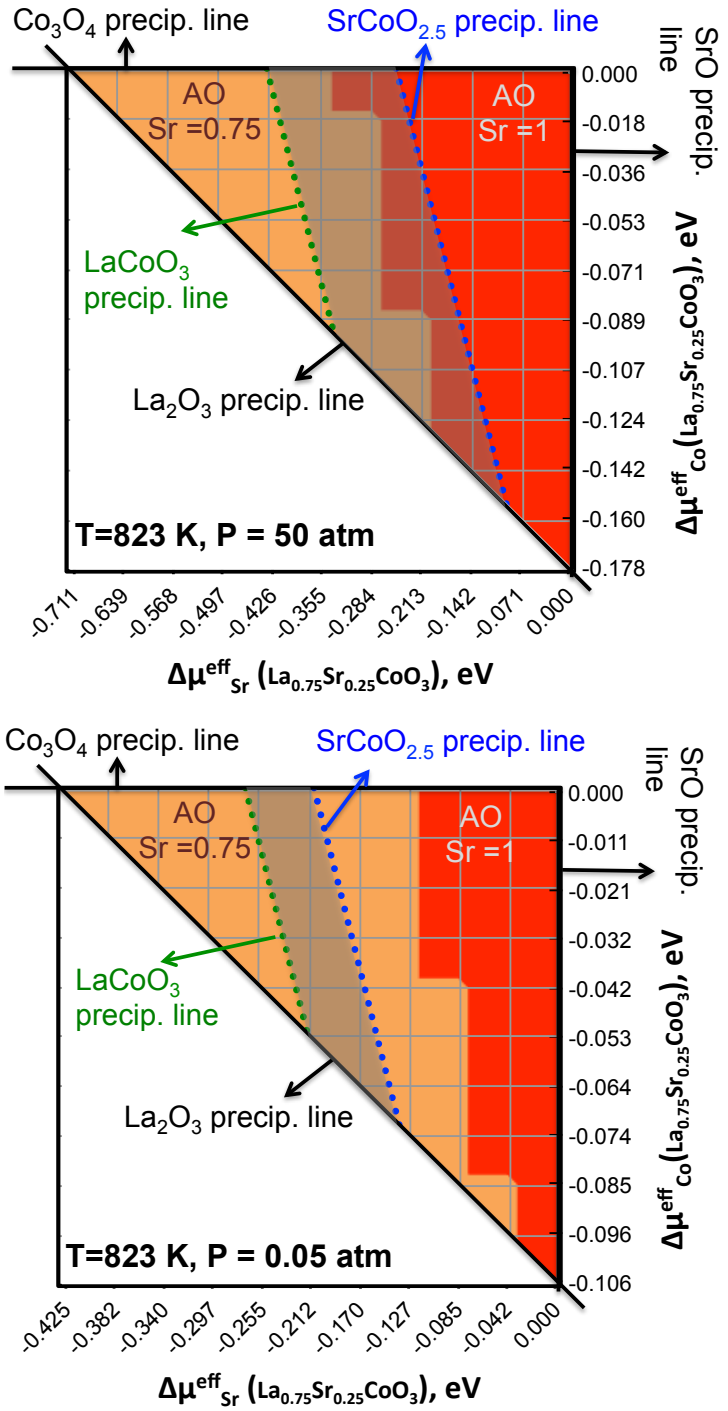

Figure 64. The predicted $La_{0.75}Sr_{0.25}CoO_3$ surface stability diagram at T = 550ºC (a) $p(O_2)$ = 1 atm, (b) $p(O_2)$ = 50 atm, and (c) $p(O_2)$ = 0.05 atm based on the chemical potentials of bulk $La_{0.75}Sr_{0.25}CoO_3$. The grid points represent the sampled bulk effective chemical potentials of Sr (x-axis; x=0 represents the equilibrium between $La_{0.75}Sr_{0.25}CoO_3$ and SrO) and Co (y-axis; y=0 represents the equilibrium between $La_{0.75}Sr_{0.25}CoO_3$ and Co_3O_4) in $La_{0.75}Sr_{0.25}CoO_3$, and the contour plot beyond the grid is constructed based on the calculated lowest surface energy among the investigated $La_{0.75}Sr_{0.25}CoO_3$ (001) surface configurations.

The *ab initio* thermodynamic analysis results suggest the most stable (001) surfaces within the bulk $La_{0.75}Sr_{0.25}CoO_3$ region is the AO surface termination with Sr concentration of 0.75 at T = 550 ºC and $p(O_2)$ = 1 atm. In addition, further increasing $p(O_2)$ to 50 atm, the stable bulk LSC_{113} region spans on both the AO surface with 75% and 100% Sr concentration on the A site as the most stable (001) surface, while decreasing $p(O_2)$ to 0.05 atm, the stable bulk LSC_{113} region is moved farther apart from the chemical potential region where the fully Sr-enriched AO surface is the stable (001) surface, as shown in Figure 64b and c. The $p(O_2)$ dependence of the LSC_{113} surface stability analysis suggests that the (001) AO surface with higher Sr content can be stabilized by increasing $p(O_2)$, consistent with the reported $p(O_2)$ dependence in surface Sr enrichment of Sr-doped $LaMnO_3$ and $LSCF_{113}$ perovskites[58, 59]. Particularly, the increase of the driving force for perovskite surface Sr segregation upon increasing $p(O_2)$ was proposed to be associated with electrostatic interactions based on the DFT and analytic models for Sr dopant interaction with charged cation and oxygen vacancies, as stability of cation and oxygen vacancies also exhibits $p(O_2)$ dependences.[58] Since no cation and anion vacancies were included in our slab models, our thermodynamic analysis suggests that enhanced perovskite surface Sr segregation upon increasing $p(O_2)$ can be attributed to minimizing surface free energy in responding to relative metal chemical potential change in bulk perovskites upon change of oxygen chemical potential, in contrast to dopant-point defect interactions.

Our results suggest Sr-rich (001) AO surfaces (surface layer Sr concentration =0.75~1.0) are the most stable surfaces among the investigated LSC_{113} (001) slab configurations. Although the current thermodynamic analysis do not contain comprehensive information of other possibly more stable phases for the LSC_{113} and LSF_{113} bulk [7, 60-62], the surface stability information will not be influenced by adding additional the bulk stability boundary lines.

Bulk and (001) surface stability analysis at a given T and $P(O_2)$ was further performed for the $LSCF_{113}$ system, where the number of independent degree of freedom is three, and the bulk phase diagram and surface stability counter plots become 3D. In Figure 65we chose a few specific chemical potentials of Fe (0, -0.12, -0.24, -0.36 eV relative to μ(Fe) in Fe_2O_3) for plotting the 2D surface stability contour plots similar to Figure 64, which correspond to a 2D truncation of the 3D plot at Δμ(Fe) = 0, -0.12, -0.24, -0.36 eV relative to μ(Fe) in Fe_2O_3. The results all show Sr-rich (001) AO surfaces are the most stable surfaces, which consistent with a very recent experimental study by Druce et al[63] on the $LSCF_{113}$ surfaces characterized with the LEIS technique. The high Fe activity condition (Δμ(Fe)> -0.12 eV relative to μ(Fe) in Fe_2O_3) can be excluded by further taking into the precipitation boundary line of the $La_{1-x}Sr_xFeO_3$ phases.

(a) $\Delta\mu^{eff}_{Fe}(La_{0.625}Sr_{0.375}Fe_{0.75}Co_{0.25}O_3) = -0.00$ eV vs. $\mu^{eff}_{Fe}(Fe_2O_3)$

Sr

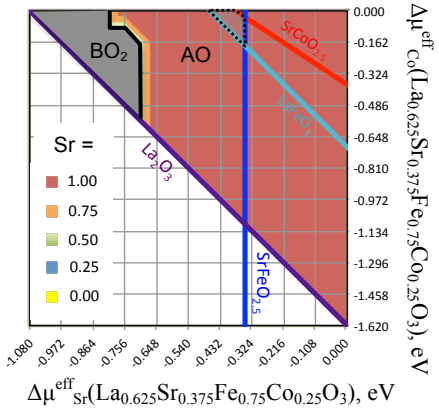

Co

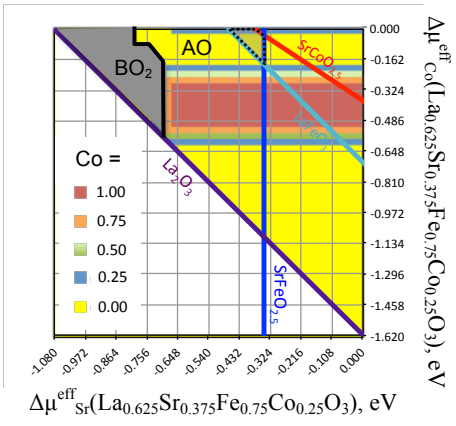

(b) $\Delta\mu^{eff}_{Fe}(La_{0.625}Sr_{0.375}Fe_{0.75}Co_{0.25}O_3) = -0.12$ eV vs. $\mu^{eff}_{Fe}(Fe_2O_3)$

Sr

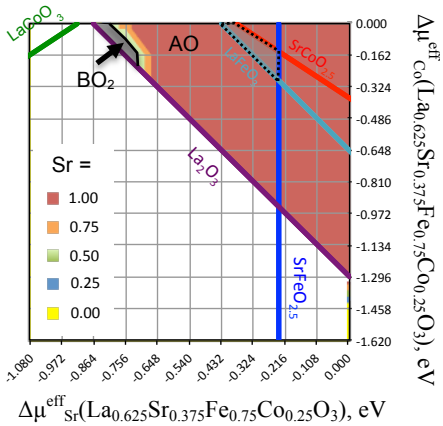

Co

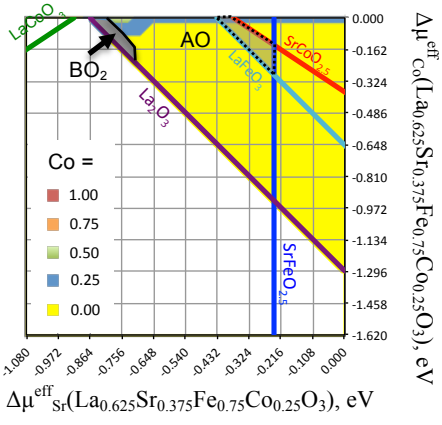

(c) $\Delta\mu^{eff}_{Fe}(La_{0.625}Sr_{0.375}Fe_{0.75}Co_{0.25}O_3) = -0.24$ eV vs. $\mu^{eff}_{Fe}(Fe_2O_3)$

Sr

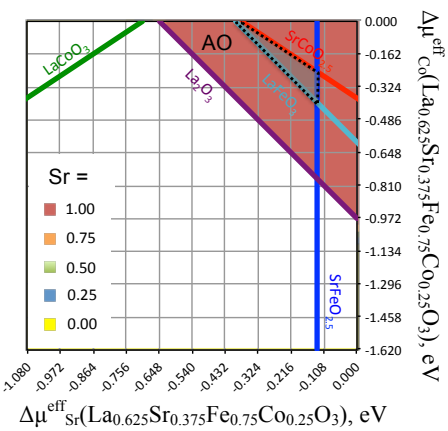

Co

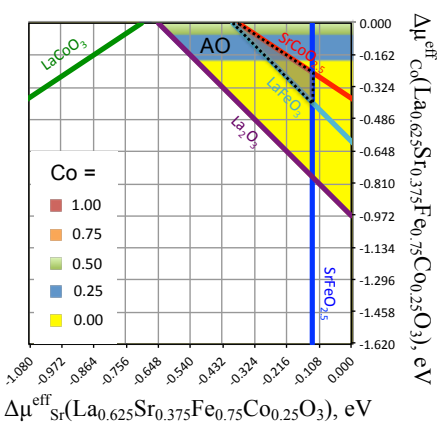

(d) $\Delta\mu^{eff}_{Fe}(La_{0.625}Sr_{0.375}Fe_{0.75}Co_{0.25}O_3) = -0.36$ eV vs. $\mu^{eff}_{Fe}(Fe_2O_3)$

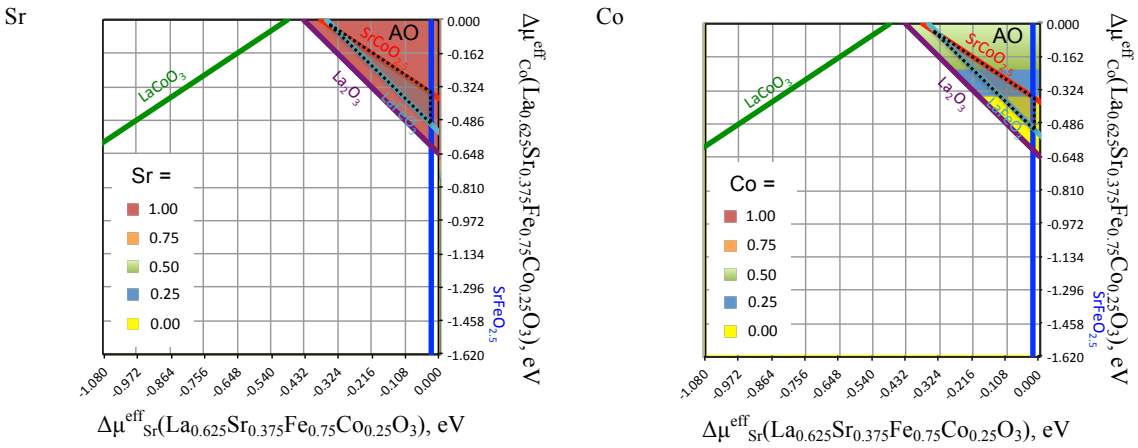

Figure 65. The predicted $La_{0.625}Sr_{0.375}Fe_{0.75}Co_{0.25}O_3$ surface stability diagram at T = 550 ºC and $p(O_2)$ = 1 atm based on the effective chemical potentials of metal constituents in bulk $La_{0.625}Sr_{0.375}Fe_{0.75}Co_{0.25}O_3$: (a) $\Delta\mu^{eff}_{Fe}(La_{0.625}Sr_{0.375}Fe_{0.75}Co_{0.25}O_3)$ = -0.00 eV vs. μ^{eff}_{Fe} (Fe_2O_3), (b) $\Delta\mu^{eff}_{Fe}(La_{0.625}Sr_{0.375}Fe_{0.75}Co_{0.25}O_3)$ = -0.12 eV vs. μ^{eff}_{Fe} (Fe_2O_3), (c) $\Delta\mu^{eff}_{Fe}(La_{0.625}Sr_{0.375}Fe_{0.75}Co_{0.25}O_3)$ = -0.24 eV vs. μ^{eff}_{Fe} (Fe_2O_3), and (d) $\Delta\mu^{eff}_{Fe}(La_{0.625}Sr_{0.375}Fe_{0.75}Co_{0.25}O_3)$ = -0.36 eV vs. μ^{eff}_{Fe} (Fe_2O_3). The two independent effective metal chemical potentials are represented by $\Delta\mu^{eff}_{Co}(La_{0.625}Sr_{0.375}Fe_{0.75}Co_{0.25}O_3)$ and $\Delta\mu^{eff}_{Sr}(La_{0.625}Sr_{0.375}Fe_{0.75}Co_{0.25}O_3)$, where $\Delta\mu^{eff}_{Co}(La_{0.625}Sr_{0.375}Fe_{0.75}Co_{0.25}O_3) = \mu^{eff}_{Co}(La_{0.625}Sr_{0.375}Fe_{0.75}Co_{0.25}O_3) - \mu^{eff}_{Co}(Co_3O_4)$ and $\Delta\mu^{eff}_{Sr}(La_{0.625}Sr_{0.375}Fe_{0.75}Co_{0.25}O_3) = \mu^{eff}_{Sr}(La_{0.625}Sr_{0.375}Fe_{0.75}Co_{0.25}O_3) - \mu^{eff}_{Sr}(SrO)$. The grid points represent the sampled bulk effective chemical potentials of Sr (x-axis; x=0 represents the equilibrium between $La_{0.625}Sr_{0.375}Fe_{0.75}Co_{0.25}O_3$ and SrO) and Co (y-axis; y=0 represents the equilibrium between $La_{0.625}Sr_{0.375}Fe_{0.75}Co_{0.25}O_3$ and Co_3O_4) in $La_{0.625}Sr_{0.375}Fe_{0.75}Co_{0.25}O_3$, and the contour plots beyond the grid are constructed based on the calculated lowest surface energy among the investigated 50 $La_{0.625}Sr_{0.375}Fe_{0.75}Co_{0.25}O_3$ (001) surface configurations. The left-hand-side plots in **Figure 65** a-d) represent the stable (001) AO surface A-site Sr content, while the right–hand-side plots represent the stable (001) AO surface sub surface layer B-site Co content. The effective chemical potential conditions in which the BO_2 surface is more stable than the AO are presented by the grey area. The shaded area within dotted lines in each plot represents the $La_{0.625}Sr_{0.375}Fe_{0.75}Co_{0.25}O_3$ bulk stable region relative to the lower order oxides, where the boundary lines represent the equilibrium between the bulk $La_{0.625}Sr_{0.375}Fe_{0.75}Co_{0.25}O_3$ and the chosen lower order oxides ($LaFeO_3$–light blue, $SrFeO_{2.5}$–deep blue, $LaCoO_3$–green, $SrCoO_{2.5}$–red, La_2O_3–purple, SrO–x=0, and Co_3O_4–y=0). The $La_{0.625}Sr_{0.375}Fe_{0.75}Co_{0.25}O_3$ (001) surface stability analysis results suggest the most stable surfaces are the AO surfaces with the surface layer A-site Sr concentration equal to 1.00 within the bulk stable region relative to the lower order oxides.

7.3.3 *Ab Initio* Thermodynamic Analysis of $LaSrCoO_4$ (001) and (100) Surfaces

7.3.3.1 Ab Initio Surface Stability Analysis for LSC_{214} (001) AO and (100) A_2BO_4 Surfaces

Figure 66 shows the contour plots for the LSC_{214} stable surface composition vs. chemical potential of metals (here we chose μ(Sr) in SrO/LSC_{214} equilibrium and μ(Co) in Co_3O_4/LSC_{214} equilibrium as the metal chemical potential references) within the stability boundary of bulk LSC_{214} in equilibrium with La_2O_3, SrO, Co_3O_4, $LaCoO_3$, and $SrCoO_{2.5}$ based on the most stable surface energy of the investigated 6 LSC_{215} slab configurations at (a) T= 823K and $P(O_2)$=1.0 bar. The boundary lines in Figure 66 are for LSC_{214} bulk stability, while the contour colormap represents the most stable surface configurations among the investigated DFT slab models.

As shown in Figure 66 our *ab initio* thermodynamic analysis predicts the fully Sr enriched surface is the most stable surface among the investigated (100) AO surface and (100) A_2BO_4 surface configurations within the bulk LSC_{214} stability region at $P(O_2)$ = 1 bar and T =823K (shaded region).

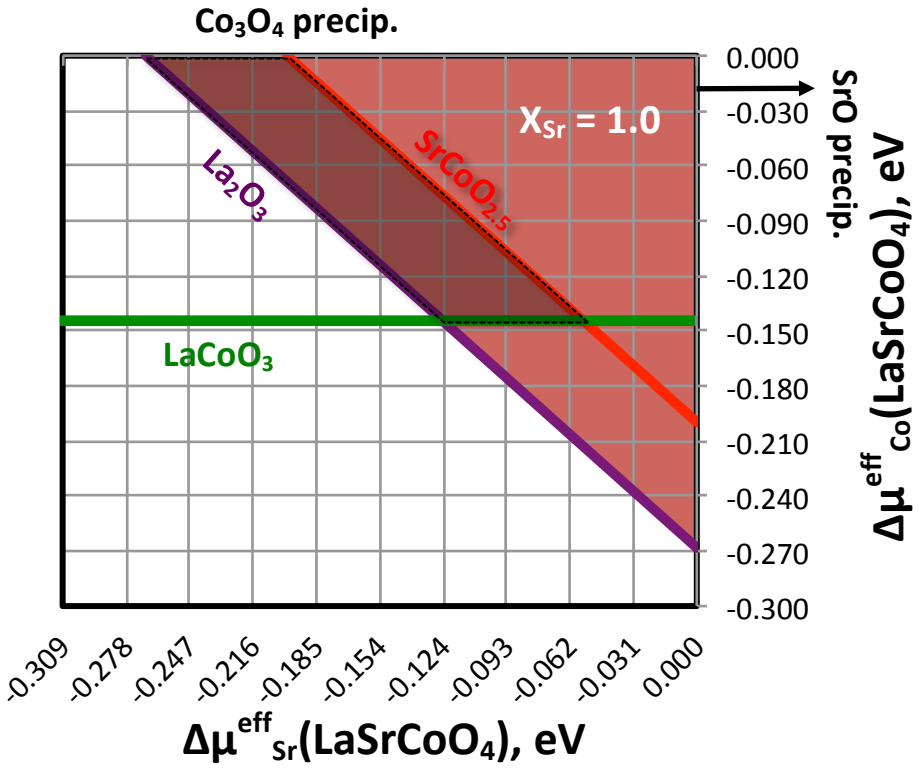

Figure 66. Predicted contour plots for the $LaSrCoO_4$ stable (001) and (100) surface layer compositions within the bulk $LaSrCoO_4$ stability boundaries (in equilibrium with La_2O_3, SrO, Co_3O_4, $LaCoO_3$, and $SrCoO_{2.5}$) based on the most stable surface energy of the investigated six $LaSrCoO_4$ slab configurations vs. chemical potentials of Sr (relative to SrO) and Co (relative to Co_3O_4) at (a) T= 823K and $P(O_2)$= 1.0 bar. The shaded region represents the stable bulk $LaSrCoO_4$. For the same surface orientation, both the (001) AO and the (100) A_2BO_4 surfaces are predicted to be stable with fully enriched surface layer Sr at the A-sites. The surface energy of the fully Sr-enriched (100) A_2BO_4 surface is found to be a factor of 1.2~2x the surface

energy (depending on chemical potentials) of the fully Sr-enriched (001) AO surface within the stable bulk $LaSrCoO_4$ region, suggesting the greater stability of the (001) AO surface with fully enriched Sr vs. the (100) A_2BO_4 surfaces.

Summarizing our *ab initio* predictions on the stable LSC_{214} (001) and (100), LSC_{113} (001), and $LSCF_{113}$ (001) surfaces, our *ab initio* thermodynamic analysis suggests the stable LSC_{113} (001) surface is the AO surface with 75% Sr, and the stable $LSCF_{113}$ and LSC_{214} surfaces are the (001) AO with 100% Sr, suggesting no (001) surface A-sites available for further enhancement of the surface Sr content. Both results are in qualitative agreement with the AES analysis for the LSC_{214} decorated vs. undecorated LSC_{113} and $LSCF_{113}$ (001) films. Nonetheless, it should be noted that the adopted thermodynamic model for predicting the stable surfaces is done within the stability region of bulk LSC_{113}, LSC_{214}, and $LSCF_{113}$ vs. lower order oxide compounds. Therefore, the current modeling approach is insufficient to explain formation of Sr secondary phases (such as SrO, $Sr(OH)_2$, $SrCO_3$, etc. [9, 64]), whose presence and growth upon annealing were found to correlate with degradation of surface exchange activity [9, 65].

7.3.3.2 Stability of the $LSCF_{113}$, LSC_{113}, and LSC_{214} at full Sr substitution relative to decomposition

Recent COBRA studies[18] reveal that the top surface layer in the perovskite phase of LSC_{113} films may contain Sr concentration at 60% on the A site and detect that discrete particles epitaxially grown to the film surface can have $SrCoO_{3-\delta}$-like composition, in which particle surface might be covered by electrochemically inactive Sr-rich phases (such as SrO). It was hypothesized that the surface particles of $SrCoO_{3-\delta}$ are most likely to decompose to form secondary phases such as $SrO/Sr(OH)_2/SrCO_3$, which can greatly impede the surface exchange kinetics.[66, 67]

In analogy to the valence stability assessment of SOFC perovskites proposed by Yokokawa *et al.,*[68] we further evaluate stability of $LSCF_{113}$ and LSC_{113} surfaces without vs. with LSC_{214} decoration against surface degradation by investigating decomposition of fully Sr substituted $LSCF_{113}$, $LSC_{113,}$ and LSC_{214} relative to the lower order binary oxides - SrO, Co_3O_4, Fe_2O_3, based on the surface Sr content reported in the COBRA measurements,[18] and the reported surface chemical inhomogeneity, i.e. formation of SrO like particles.[9, 59] Although these reaction energies are calculated for bulk compositions, we will assume the give at least qualitative guidance for the stability of the Sr enriched surface layers.

The decomposition reaction free energy (to form the lower order binary metal oxides - SrO, Co_3O_4, Fe_2O_3) is equivalent to the negative formation free energy of $LSCF_{113}$, $LSC_{113,}$ and LSC_{214} from the lower order binary metal oxides at a given T and $p(O_2)$ condition. We found that the calculated *ab initio* decomposition free energy of $SrCo_{0.25}Fe_{0.75}O_3$, $SrCoO_3$, and Sr_2CoO_4 at T = 550 °C and $p(O_2)$ = 1 atm are +0.443, +0.096, and +0.481 eV per formula unit, respectively, based on the defined effective chemical potential of oxygen and the computed *ab initio* formation energy of $SrCo_{0.25}Fe_{0.75}O_3$, $SrCoO_3$, and Sr_2CoO_4[19]. We note that an additional B-site configuration entropy term for $SrCo_{0.25}Fe_{0.75}O_3$, which corresponds to -0.04 eV per formula unit, is neglected here, which will further stabilize the $SrCo_{0.25}Fe_{0.75}O_3$. The positive reaction free energy means that an energy penalty is required to decompose the compound, and a larger value corresponds to a higher energy cost for the decomposition reaction and higher stability of the compound. Our *ab initio* decomposition reaction free energy results suggest that $SrCoO_3$ is more prone to decompose with

respect to the lower order binary metal oxides than $SrCo_{0.25}Fe_{0.75}O_3$ and Sr_2CoO_4, while both $SrCo_{0.25}Fe_{0.75}O_3$ and Sr_2CoO_4 exhibit comparable stability against the decomposition at T = 550 °C and $p(O_2)$ = 1 atm.

In addition to the decomposition reaction relative to the binary metal oxides, it is also likely that decomposition of the perovskite may occur via the following reaction:[69-71]

$$SrCoO_3 \rightarrow \frac{1}{2}Sr_2CoO_4 + \frac{1}{6}Co_3O_4 + \frac{1}{6}O_2 \quad \text{….. Eqn. 16}$$

$$SrCo_{0.25}Fe_{0.75}O_3 \rightarrow \frac{1}{8}Sr_2CoO_4 + \frac{1}{24}Co_3O_4 + \frac{1}{24}O_2 + \frac{3}{4}SrFeO_3 \quad \text{….. Eqn. 17}$$

The calculated reaction free energies for the reaction (1) and (2) are -0.144 eV, and -0.019 eV (or +0.011 eV with the B-site configuration entropy term for $SrCo_{0.25}Fe_{0.75}O_3$), respectively, at T = 550 °C and $p(O_2)$ = 1 atm. Again, the decomposition with respect to Sr_2CoO_4 and Co_3O_4 formation is more exothermic for $SrCoO_3$ than $SrCo_{0.25}Fe_{0.75}O_3$, indicating a poorer stability of $SrCoO_3$ than $SrCo_{0.25}Fe_{0.75}O_3$ with respect to formation of Sr_2CoO_4 and Co_3O_4. It is also hypothesized that the Co_3O_4 formation in the reaction (1) and (2) may cause degradation of surface exchange activity, due to loss of the more active perovskite phase. Therefore, upon LSC_{214} decoration, both the reaction (1) and (2) will reduce the tendency to decompose (increasing activity of the reaction product can reduce the reaction driving force), while a much weaker reduction in the thermodynamic driving force is expected for $SrCo_{0.25}Fe_{0.75}O_3$ than $SrCoO_3$, as the decomposition reaction free energy of reaction (2) is close to 0 eV. It is noted that an additional B-site configuration entropy term for $SrCo_{0.25}Fe_{0.75}O_3$, which corresponds to ~-0.04 eV per formula unit, is neglected here, which will further stabilize $SrCo_{0.25}Fe_{0.75}O_3$ and not alter the stability trend discussed above.

In general, these results suggest, for the high Sr content we studied, that addition of Fe stabilizes the LSC_{113} phase and that the RP structures are more stable than the ABO_3 structures, at least for Co. Overall, the predicted stability trends of bulk $SrCo_{0.25}Fe_{0.75}O_3$, $SrCoO_3$, and Sr_2CoO_4 are in good agreement with the observed experimental trends of surface stability for $LSCF_{113}$, LSC_{113} with and without LSC_{214} decoration, suggesting a correlation between surface degradation/particle formation and stability differences among $LSCF_{113}$, LSC_{113}, and LSC_{214} against decomposition.

7.3.3.3 Stability of LSC_{113} and LSC_{214} Relative to Binary Metal Oxides

Figure 67 shows the calculated stability diagram of LSC_{113} and LSC_{214} relative to the La_2O_3, SrO, and Co_3O_4 binary metal oxide references under the condition of T=823 K and $P(O_2)$ = 1 atm. Two additional phases, brownmillerite $Sr_2Co_2O_5$ and hexagonal phase $Sr_6Co_5O_{15}$[72], are also included in the analysis. For LSC_{214}, a $Sr_2CoO_{3.5}$ phase with oxygen vacancies located in the CoO_2 plane was found to be less stable (+0.02 eV per formula unit relative to SrO and Co_3O_4) than the Sr_2CoO_4 phase and is not included in the stability diagram. **Figure 67**(a) shows the normalized free energy (per Co) of LSC_{113} + (1/2 La_2O_3, SrO) vs. LSC_{214}, which corresponds to A-site rich condition constrained to the A-site vs. B-site ratio of LSC_{214}.

On the other hand, **Figure 67**(b) shows the normalized free energy (per A-site) of LSC_{113} vs. ½ LSC_{214} + $^1/_6$ Co_3O_4, which corresponds to the condition constrained to the A-site vs. B-site ratio of

LSC_{113}. Our results indicate the stoichiometric LSC_{113} phases (red squares) are comparable to or less stable than the LSC_{214} phases (in coexist with Co_3O_4 oxides, blue circles) at high Sr content, although the $Sr_6Co_5O_{15}$ (and $Sr_2Co_2O_5$) phase is found to be more stable than the Sr_2CoO_4 phase. Further works are still needed to include understoichiometric LSC_{113} and LSC_{214} phases and other relevant RP phases to refine the stability diagram. Overall, our results indicate stability of LSC_{113} and LSC_{214} can be greatly influenced by the Sr concentration and varying A-site and B-site ratio or local chemical inhomogeneity (La/Sr vs. Co ratio) can have a strong influence on the phase stability between the perovskite and RP_{214} phases at high Sr content. A further discussion of the relative stability trend between the $LSCF_{113}/LSCF_{214}$ and LSC_{113}/LSC_{214} systems will be discussed below.

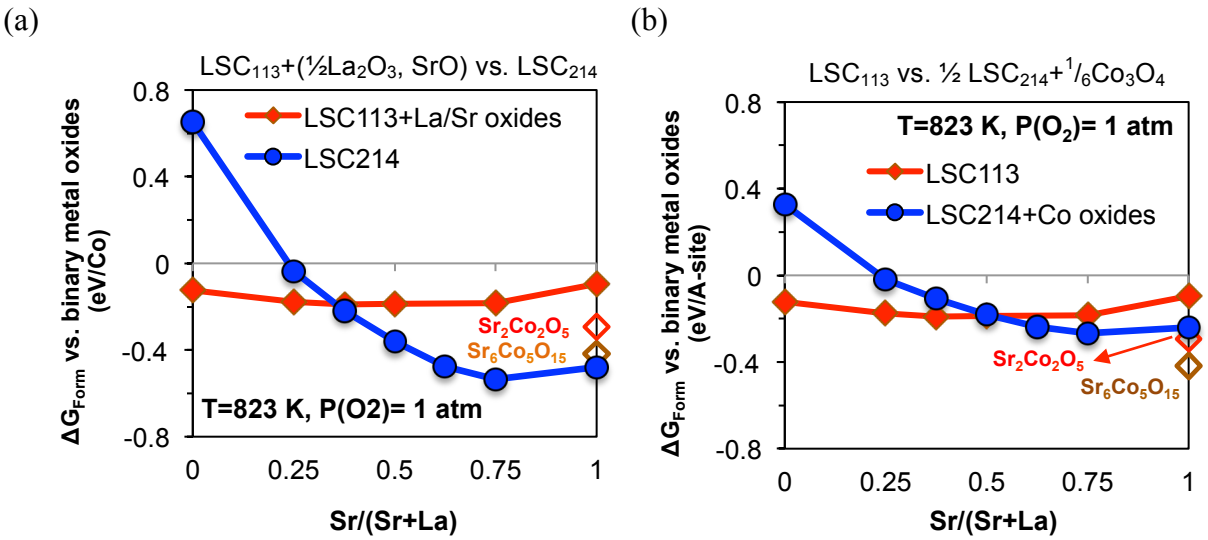

Figure 67. The computed stability (ΔG_{Form}) of LSC_{113} (red) and LSC_{214} (blue) at various Sr concentration relative to the La_2O_3, SrO, and Co_3O_4 references under the condition of T=823 K and $P(O_2)$= 1atm, based on the *ab initio* thermodynamic approach described in the Supporting Information of Ref. [19]: (a) LSC_{113} + ($\frac{1}{2}La_2O_3$, SrO) vs. LSC_{214}; *i.e.*, A vs. B site metal cation ion ration equal to 2 (b) LSC_{113} vs. ½ $LSC_{214}+{}^1/_6Co_3O_4$; *i.e.*, A vs. B site metal cation ion ration equal to 1. The empty red symbol represents the $SrCoO_{2.5}$ phase.

7.3.3.4 Stability of $LSCF_{113}$ and $LSCF_{214}$ Relative to Binary Metal Oxides

Similar analysis to that on LSC_{113} and LSC_{214} phases discussed above was also performed for $LSCF_{113}$ and $LSCF_{214}$ phases. To focus on the stability trend of $LSCF_{113}$ vs. LSC_{113} with respect to their RP_{214} phases, an artificial constraint of Fe/Co ratio fixed to 3 is imposed for the $LSCF_{113}$ and $LSCF_{214}$ phases (also imposed in the DFT models). In addition, a linear combination of the stability for the brownmillerite phases, $SrFeO_{2.5}$ and $SrCoO_{2.5}$ (relative to SrO, Co_3O_4 and Fe_2O_3), was used to represent $SrFe_{0.75}Co_{0.25}O_{2.5}$ phase (the empty brown triangles in **Figure 68**). Focusing on the condition of the A-site vs. B-site ratio equal to 2, *i.e.* the RP phases, similar behavior to the LSC_{113} and LSC_{214} system is observed: the $LSCF_{214}$ phases become stabilized over the $LSCF_{113}$ at high Sr content. On the other hand, under the condition of the A-site vs. B-site ratio equal to 1, *i.e.* the perovskite phases, the $LSCF_{113}$ phases were reveal to exhibit greater stability than all the RP_{214} phases even at high Sr content, consistent with the observed stability trend of $LSCF_{113}$ vs. LSC_{113} films[19]. Overall, Our results indicate a strong influence of on relative stability of the perovskite phase vs. the RP phase upon varying the A-site and B-site metal content for both LSC_{113} and

$LSCF_{113}$, and greater stability of the $LSCF_{113}$ phase at high Sr concentration as compared to the LSC_{113} phase.

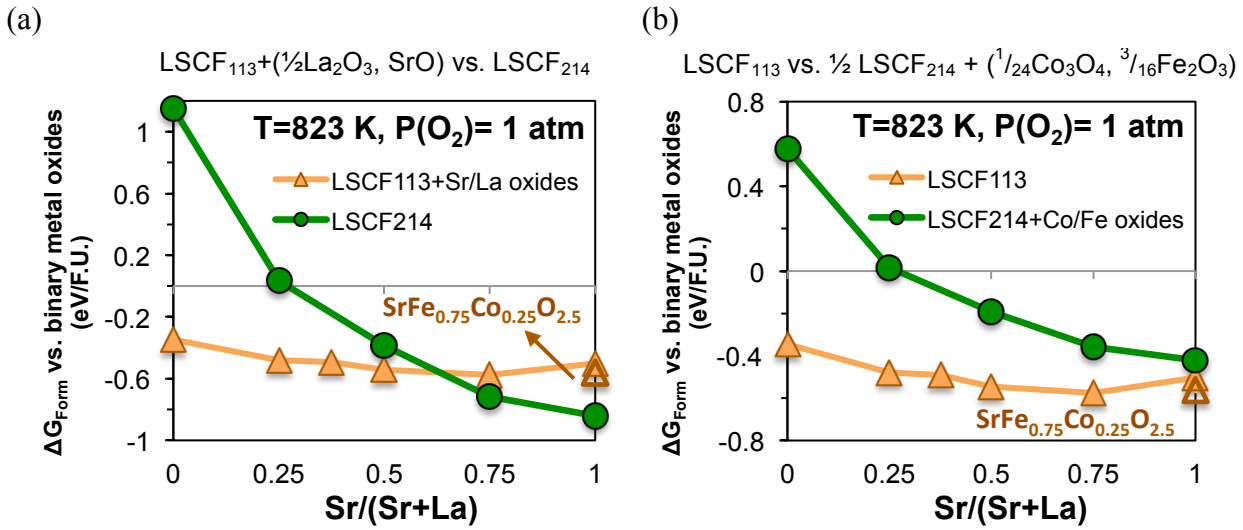

Figure 68. The computed stability (ΔG_{Form}) of $LSCF_{113}$ (orange) and $LSCF_{214}$ (green) at various Sr concentration relative to the La_2O_3, SrO, Co_3O_4, and Fe_2O_3 references under the condition of T=823 K and $P(O_2)$= 1atm, based on the *ab initio* thermodynamic approach described in the Supporting Information of Ref. [19]: (a) $LSCF_{113}$ +(½La_2O_3, SrO) vs. $LSCF_{214}$; *i.e.*, A vs. B site metal cation ion ration equal to 2 (b) $LSCF_{113}$ vs. ½ $LSCF_{214}$ + ($^1/_{24}Co_3O_4$, $^3/_{16}Fe_2O_3$); *i.e.*, A vs. B site metal cation ion ration equal to 1.We note the Fe/Co ratio in Figure 8 is fixed to 3 in the stability diagram. The brown empty triangles represent the brownmillerite phase $SrFe_{0.75}Co_{0.25}O_{2.5}$, obtained from a linear combination of ΔG_{Form}s of $SrFeO_{2.5}$ and $SrCoO_{2.5}$.

7.3.3.5 Summary

Ab initio based thermodynamic analysis was performed to investigate stability of the LSC_{113}, LSC_{214}, $LSCF_{113}$, and $LSCF_{214}$ phases relative to the binary metal oxides La_2O_3, SrO, Co_3O_4, and Fe_2O_3 at a wide range of Sr content under the experimental operating conditions (at T= 823K and $P(O_2)$ = 1atm). Our results indicate a strong influence of on relative stability of the perovskite phase vs. the RP phase upon varying the A-site and B-site metal content for both LSC_{113} and $LSCF_{113}$, and greater instability of the LSC_{113} phase at high Sr concentration as compared to the $LSCF_{113}$ phase. Our results can be further refined with more thorough exploration of possible stable phases (e.g. including oxygen nonstoichiometry) to construct an *ab initio* based SrO-La_2O_3-CoO_x ternary phase diagrams for LSC_{113}/LSC_{214} and an *ab initio* based quaternary SrO-La_2O_3-CoO_x-Fe_2O_3 phase diagram for $LSCF_{113}$ under a given T and $P(O_2)$.

7.4 *Ab initio* modeling of $LaSrCoO_{4\pm\delta}$/$LSCF_{113}$ Heterointerfaces

7.4.1 Ab Initio modeling for Sr substitution in LSC_{214}, $LSCF_{113}$, and the LSC_{214}–$LSCF_{113}$ interfaces

DFT calculations were performed to investigate energy for Sr substitution of La (Sr_{La}) in the structures of LSC_{214}, LSC_{113}, and $LSCF_{113}$, and the results are shown in Figure 69. The calculated Sr_{La} substitution energies in the relaxed bulk LSC_{214}, LSC_{113}, and $LSCF_{113}$ (all relative to that of LSC_{113}) suggest a weaker thermodynamic driving force (-0.12 eV) for Sr interdiffusion from $LSCF_{113}$ to LSC_{214} than from LSC_{113} to LSC_{214} (-0.7 eV). The Sr_{La} substitution energies are based on the most stable $LSCF_{113}$ and LSC_{214} configurations among the investigated ones. The upper bound and the lower bound of the calculated Sr_{La} substitution energies due to different cation arrangements are also included in Figure 69 to indicate possible Sr_{La} substitution energy variation. Although the range of Sr_{La} substitution energies is about half of the magnitude of the most stable configuration for $LSCF_{113}$ and LSC_{214}, the relative trend in Sr_{La} substitution of $LSCF_{113}$ vs. LSC_{113} (both relative to LSC_{214}) is sustained regardless of the Sr_{La} substitution energy variation.

To further understand the interfacial effect on the Sr_{La} substitution energies, three different Sr/La and Co/Fe arrangements in the LSC_{214}-$LSCF_{113}$ interface model are also investigated, as shown in Figure 70. It is seen that the most stable Sr_{La} substitution is located in the first interface layer of the interfacial region (B1). Moving from this interface layer with the most stable Sr_{La} substitution toward the $LSCF_{113}$ and LSC_{214} regions, the Sr_{La} substitution energies increase (less stable) and approach to the bulk $LSCF_{113}$ and LSC_{214} values. In contrast to the results of the previous the LSC_{214}-LSC_{113} interface study[32], where Sr_{La} substitution becomes monotonically more stable moving from the LSC_{113} toward the LSC_{214} region, the $LSCF_{113}$-LSC_{214} interface model results reveal an additional interfacial stabilization effect on Sr_{La} substitution, which can be attributed to the interfacial charge introduced by $LSCF_{113}$ bulk polarity (interface between polar LSCF and nonpolar AO-BO_2-AO LSC_{214})[73].

It is noted that the energies in **Figure 69** represent thermodynamic stability of Sr_{La} substitution (relative to the bulk LSC_{113}) for the simulated bulk phase composition, rather than the equilibrated interfacial configurations. The as-grown $LSCF_{113}$ film surfaces are likely to be Sr enriched, which has also been revealed in the case of LSC_{113} base film surfaces[18], and thereby the thermodynamic driving force for Sr_{La} interdiffusion from the decorated LSC_{214} phase backward to the LSC_{214}-$LSCF_{113}$ interfaces (as implied in

Figure 70) is expected to be reduced when the $LSCF_{113}$ surface contains high Sr content than the bulk.

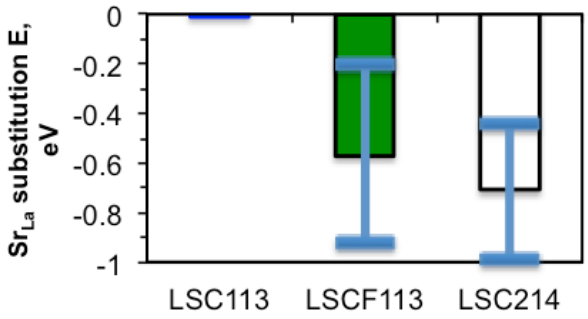

Figure 69. The calculated Sr_{La} substitution energies in relaxed bulk LSC_{214}, LSC_{113}, and $LSCF_{113}$ (all relative to that of LSC_{113}).

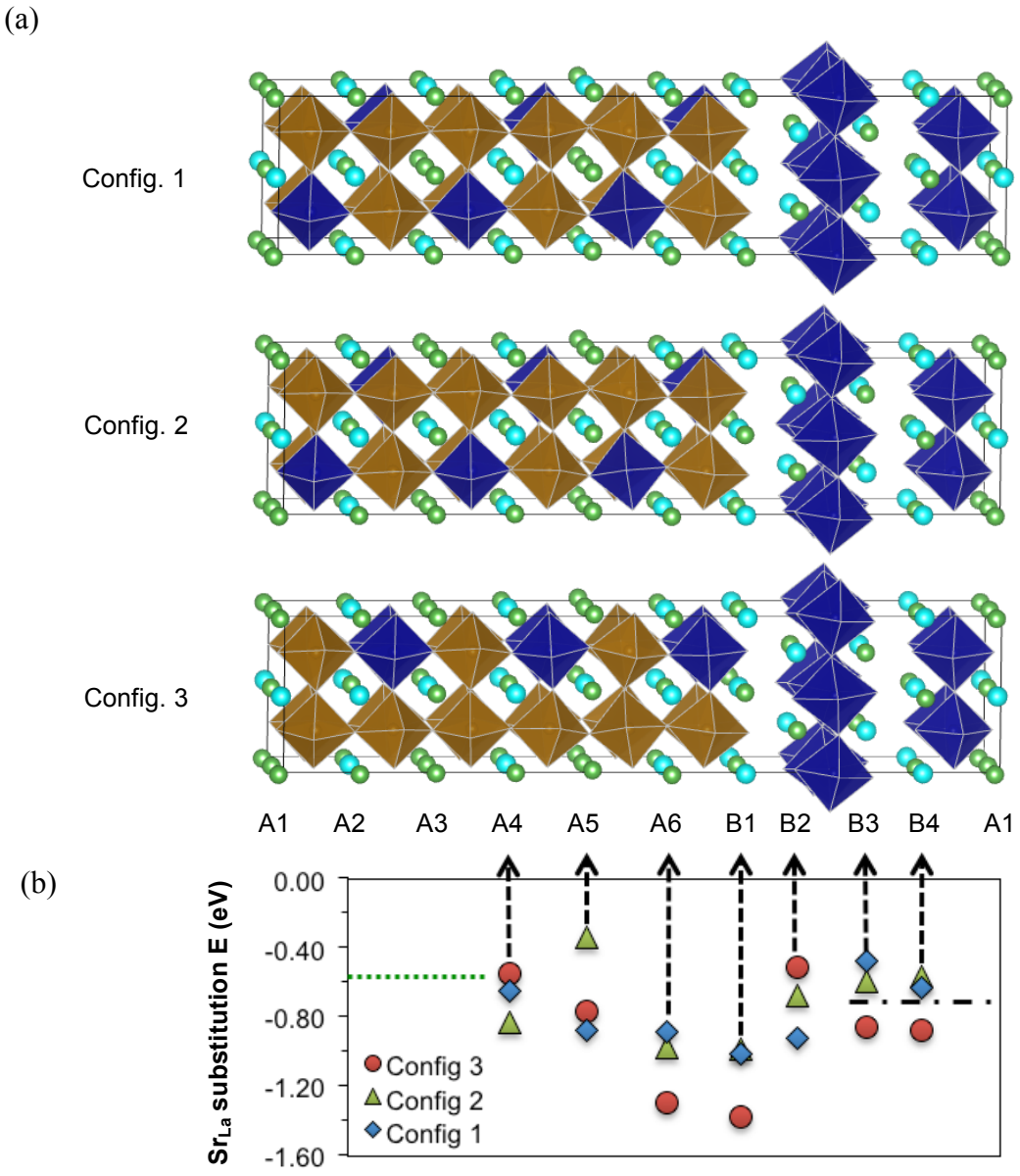

Figure 70. (a) Schematics of the heterostructured interfaces with various A-site and B-site arrangements in the DFT simulations. $La_{0.625}Sr_{0.375}Fe_{0.75}Co_{0.25}O_3$ represents the $LSCF_{113}$ phase and $(La_{0.5}Sr_{0.5})_2CoO_4$ represents the LSC_{214} phase. Elements are represented as: La (green), Sr (light blue), Fe (brown, center of the octahedra), and Co^{3+} (dark blue, center of the octahedra). O ions are located at the corners of all the octahedra. The AO planes are numbered from A1 through A6 in the $LSCF_{113}$ and B1 through B4 in the LSC_{214} phase. The planes A1, B1 and B2 represent an interfacial region. The relative stability of Sr_{La} substitution energy relative to $La_{0.75}Sr_{0.25}CoO_3$, or $E(Sr_{La})$-$E(Sr_{La})$ of LSC_{113}(25%Sr), with variation in the Sr_{La} defect position across the AO planes. Values are relative to a bulk LSC_{113}(25%Sr) reference (y=0). Also shown is a dotted horizontal line representing the Sr_{La} substitution energies for the bulk $LSCF_{113}$ (green dotted line, $E(Sr_{La})LSCF_{113}$ - $E(Sr_{La})LSC_{113}$(25%Sr)), and a black dash–dotted line for the bulk LSC_{214} (or $E(Sr_{La})LSC_{214}$ - $E(Sr_{La})LSC_{113}$(25%Sr)). Note that the more negative values on the y-axis correspond to the easier substitution of the Sr_{La} relative to bulk LSC_{113}(25%Sr).

Combining the *ab initio* modeling results for the Sr_{La} substitution energies in bulk LSC_{113}, LSC_{214}, and $LSCF_{113}$, as well as the LSC_{214}-$LSCF_{113}$ and LSC_{214}-$LSCF_{113}$ heterointerfaces, here we discuss on the underlying origins that are responsible for the distinct surface chemistry change upon the LSC_{214} decoration for the LSC_{113} vs. the $LSCF_{113}$ films.

In the case of the LSC_{113} (001) base film, the stable surface layer within the perovskite phase may contain Sr concentration at 60% (COBRA[18])~ 75% (DFT predictions, Figure 64), and additional surface particles, which may contain $SrCoO_{3-\delta}$[18] with other inactive Sr-rich passive phases, are formed above the surfaces. Upon LSC_{214} decoration, the decorated LSC_{214} phase acts as a Sr sink (based on the Sr_{La} substitution energy from the LSC_{113} to interface of LSC_{113}-LSC_{214} to the LSC_{214} phase[32] and surface) and the perovskite phase stabilizer[74]. Therefore, both the uncovered part of the LSC_{113} film surface and the surface of the decorated LSC_{214} phase allow increase of Sr content from 60~75% to ~100%, as revealed by the COBRA measurement[51], leading to the significant increase of surface Sr content of LSC_{214} decorated LSC_{113} vs. the LSC_{113} base film.

In the case of the $LSCF_{113}$ base film, the top (001) AO surface layer is predicted to be fully Sr occupied based on the *ab initio* surface stability analysis (Figure 65). Upon LSC_{214} decoration, there are no additional A-sites available for more Sr to be placed in the $LSCF_{113}$ surface lattice. In addition, the much smaller thermodynamic driving force for Sr interdiffusion from the bulk $LSCF_{113}$ to the bulk LSC_{214} (Figure 69) indicate that the LSC_{214} on $LSCF_{113}$ may contain smaller increase in Sr content as compared to the LSC_{214} decorated on the LSC_{113}. Overall, both no increase of Sr in the surface layer of $LSCF_{113}$ and smaller thermodynamic driving force for Sr interdiffusion from the $LSCF_{113}$ to LSC_{214} vs. that of LSC_{113} to LSC_{214} lead to a minor change in Sr content at the LSC_{214} decorate $LSCF_{113}$ surfaces.

With the observed surface chemistry change, here we discuss on how surface electronic structure change upon Sr segregation within the perovskite/Ruddlesden-Popper phases can be connected with the observed surface exchange kinetics enhancement for the LSC_{214} decorated $LSCF_{113}$ film (relative to the $LSCF_{113}$ base film) vs. the LSC_{214} decorated LSC_{113} film (relative to the LSC_{113} base film).

The increased Sr content within the perovskite phases has been shown to lead to upshift of the O 2p-band center relative to the Fermi level[44, 75], which further correlates with the observed surface oxygen exchange kinetics. In addition, by utilizing the surface layer Sr content within the perovskite phase from the COBRA measurement, it was also shown the upshift of the O 2p-band centers with increasing Sr can correlate with the observed activity enhancement for oxygen surface exchange of the LSC_{214} decorated LSC_{113} vs. LSC_{113}[51]. In Figure 71, we compare the relative change of the surface exchange coefficient k^q[19] vs. the calculated bulk O 2p-band centers (relative to the Fermi level) between the LSC_{214} decorated $LSCF_{113}$ (LSC_{113}) film surfaces and the $LSCF_{113}$ (LSC_{113}) base film surfaces, based on the predicted/measured surface Sr content of the LSC_{113} and $LSCF_{113}$ (001) base film surfaces, as well as the available Sr content information from the COBRA analysis[51] (for LSC_{214} decorated LSC_{113}) and the DFT modeling results for the calculated Sr_{La} substitution energies between LSC_{214} vs. $LSCF_{113}$ (for the LSC_{214} decorated $LSCF_{113}$ vs. the $LSCF_{113}$ base films). In the case of the LSC_{214} decorated LSC_{113} vs. LSC_{113} base films, the Sr content in the surface layer of the LSC_{113} can be increased from 60%~75% for the undecorated LSC_{113} film to 100% for the uncovered LSC_{113} film surfaces with the LSC_{214} decoration[51]. Furthermore, the fully Sr occupied top surface layer of

the LSC_{214} islands on the LSC_{113} film contains a higher O 2p-band center than the surface layer of the particles on the $LSCO_{113}$ film, which leads to higher activities (1~2 orders magnitude enhancement in surface exchange K^qs)[51].

On the other hand, both the Sr saturated $LSCF_{113}$ (001) surface layer (predicted by the DFT modeling) and the much smaller thermodynamic driving force for Sr_{La} interdiffusion from the $LSCF_{113}$ to the LSC_{214} shown in Figure 69 and Figure 70(b), suggests no change or smaller increase of Sr content in the surface of the LSC_{214} decorated $LSCF_{113}$ vs. the $LSCF_{113}$ base film, leading to almost no or slight upshift of the O 2p-band centers relative to the Fermi level, which is consistent with the only ~2 fold enhancement of the $LSCF_{113}$ surface exchange k^qs. Therefore, the unique Sr occupancy changes within the LSC_{214}-on-$LSCF_{113}$ and LSC_{214}-on-LSC_{113} heterostructure relative to the undecorated $LSCF_{113}$ and LSC_{113} base films may be responsible for the observed enhanced surface exchange kinetics.

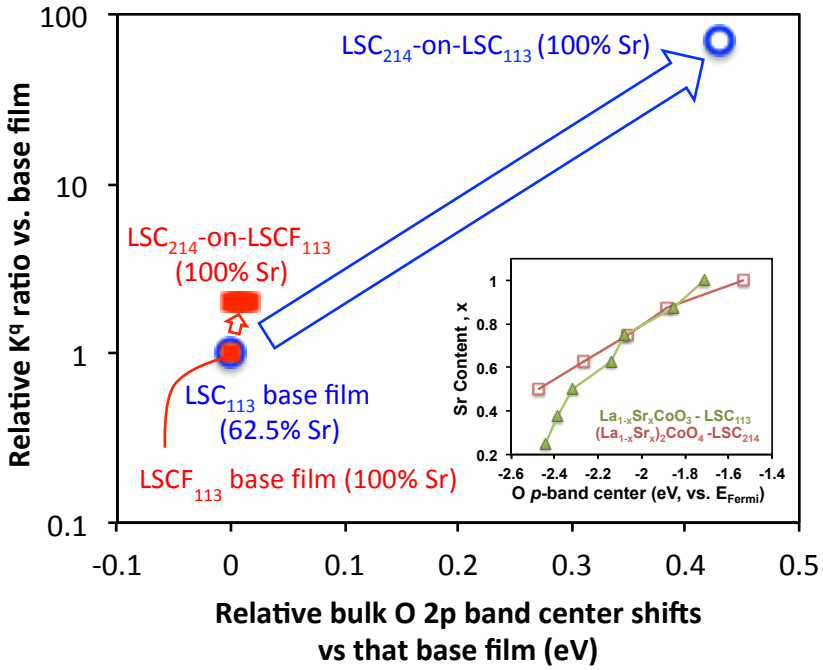

Figure 71. The relative ratio of the surface exchange coefficient k^q (with respect to the k^q of the base film) vs. the calculated bulk O 2p-band center shifts (relative to the Fermi level) between the LSC_{214} decorated $LSCF_{113}$ (LSC_{113}) film surfaces and the $LSCF_{113}$ (LSC_{113}) base film surfaces based on the surface Sr information from COBRA analysis [51] and DFT modeling predictions. The k^q data is taken from Figure 6 of the SECA Annual Report. The inlet figure is the Sr content vs. the calculated bulk O 2p-band centers of $La_{1-x}Sr_xCoO_3$ and $(La_{1-x}Sr_x)_2CoO_4$[19].

8 References

1. Yashiro, K., et al., *Composite Cathode of Perovskite-Related Oxides, (La,Sr)CoO[sub 3−δ]/(La,Sr)[sub 2]CoO[sub 4−δ], for Solid Oxide Fuel Cells*. Electrochemical and Solid-State Letters, 2009. **12**(9): p. B135.

2. Sase, M., et al., *Enhancement of oxygen exchange at the hetero interface of (La,Sr)CoO3/(La,Sr)(2)CoO4 in composite ceramics*. Solid State Ionics, 2008. **178**(35-36): p. 1843-1852.

3. Mutoro, E., et al., *Enhanced oxygen reduction activity on surface-decorated perovskite thin films for solid oxide fuel cells*. Energy & Environmental Science, 2011. **4**(9): p. 3689-3696.

4. Crumlin, E.J., et al., *Oxygen Reduction Kinetics Enhancement on a Heterostructured Oxide Surface for Solid Oxide Fuel Cells*. The Journal of Physical Chemistry Letters, 2010. **1**(21): p. 3149-3155.

5. Han, J.W. and B. Yildiz, *Mechanism for enhanced oxygen reduction kinetics at the (La,Sr)CoO3-[small delta]/(La,Sr)2CoO4+[small delta] hetero-interface*. Energy & Environmental Science, 2012. **5**(9): p. 8598-8607.

6. Maier, J., *On the correlation of macroscopic and microscopic rate constants in solid state chemistry*. Solid State Ionics, 1998. **112**(3-4): p. 197-228.

7. Hashimoto, S.-i., et al., *Oxygen nonstoichiometry and thermo-chemical stability of La0.6Sr0.4Co1-yFeyO3-d (y=0.2, 0.4, 0.6, 0.8)*. Solid State Ionics, 2010. **181**(37,Äì38): p. 1713-1719.

8. Benson, S.J., R.J. Chater, and J.A. Kilner. *Proceedings of the Third International Symposium on Ionic and Mixed Conducting Ceramics*. in *The Third International Symposium on Ionic and Mixed Conducting Ceramics*. 1997. Paris, France: Electrochemical Society (1998).

9. Kubicek, M., et al., *Relationship between Cation Segregation and the Electrochemical Oxygen Reduction Kinetics of La0.6Sr0.4CoO3,àíŒ¥ Thin Film Electrodes*. Journal of the Electrochemical Society, 2011. **158**(6): p. B727-B734.

10. Feng, Z., et al., *In Situ Studies of the Temperature-Dependent Surface Structure and Chemistry of Single-Crystalline (001)-Oriented La0.8Sr0.2CoO3,àíŒ¥ Perovskite Thin Films*. The Journal of Physical Chemistry Letters, 2013. **4**(9): p. 1512-1518.

11. Christen, H.M., et al., *Ferroelectric and antiferroelectric coupling in superlattices of paraelectric perovskites at room temperature*. Physical Review B, 2003. **68**(2): p. 020101.

12. Manning, P.S., et al., *The kinetics of oxygen transport in 9.5 mol % single crystal yttria stabilised zirconia*. Solid State Ionics, 1997. **100**(1,Äì2): p. 1-10.

13. Maier, J., *On the correlation of macroscopic and microscopic rate constants in solid state chemistry*. Solid State Ionics, 1998. **112**(3,Äì4): p. 197-228.

14. Perry Murray, E., M.J. Sever, and S.A. Barnett, *Electrochemical performance of (La,Sr)(Co,Fe)O3-(Ce,Gd)O3 composite cathodes*. Solid State Ionics, 2002. **148**(1,Äì2): p. 27-34.

15. Lee, D., et al., *Strontium Influence on the Oxygen Electrocatalysis of La2-xSrxNiO4±δ (0.0 ≤ xSr ≤ 1.0) Thin Films*. Journal of Materials Chemistry A, 2014. **2**: p. 6480-6487.

16. Kilner, J.A., R.A. De Souza, and I.C. Fullarton, *Surface exchange of oxygen in mixed conducting perovskite oxides*. Solid State Ionics, 1996. **86-88**(Part 2): p. 703-709.

17. Berenov, A.V., et al., *Oxygen tracer diffusion and surface exchange kinetics in La0.6Sr0.4CoO3-δ*. Solid State Ionics, 2010. **181**(17–18): p. 819-826.

18. Feng, Z., et al., *Revealing the Atomic Structure and Strontium Distribution in Nanometer-Thick La0.8Sr0.2CoO3-[small delta] Grown on (001)-Oriented SrTiO3*. Energy & Environmental Science, 2014.

19. Lee, D., et al., *Oxygen surface exchange kinetics and stability of (La,Sr)2CoO4+/-[small delta]/La1-xSrxMO3-[small delta] (M = Co and Fe) hetero-interfaces at intermediate temperatures*. Journal of Materials Chemistry A, 2015. **3**(5): p. 2144-2157.

20. Steele, B.C.H. and J.-M. Bae, *Properties of La0.6Sr0.4Co0.2Fe0.8O3−x (LSCF) double layer cathodes on gadolinium-doped cerium oxide (CGO) electrolytes: II. Role of oxygen exchange and diffusion*. Solid State Ionics, 1998. **106**(3–4): p. 255-261.

21. Kuhn, M., et al., *Oxygen Nonstoichiometry of Perovskite-type La0.6Sr0.4Co1-yFeyO3-δ (y=0, 0.2, 0.4, 0.5, 0.6, 0.8, 1) SOFC Cathode Materials*. ECS Transactions, 2011. **35**(1): p. 1881-1890.

22. Huber, T.M., et al., *Temperature gradients in microelectrode measurements: Relevance and solutions for studies of SOFC electrode materials*. Solid State Ionics, 2014. **268, Part A**(0): p. 82-93.

23. Kuhn, M., et al., *Oxygen Nonstoichiometry and Thermo-Chemical Stability of Perovskite-Type La0.6Sr0.4Co1-yFeyO3-δ (y = 0, 0.2, 0.4, 0.5, 0.6, 0.8, 1) Materials*. Journal of the Electrochemical Society, 2013. **160**(1): p. F34-F42.

24. Adler, S.B., J.A. Lane, and B.C.H. Steele, *Electrode kinetics of porous mixed-conducting oxygen electrodes*. Journal of the Electrochemical Society, 1996. **143**(11): p. 3554-3564.

25. Lu, Y., C. Kreller, and S.B. Adler, *Measurement and Modeling of the Impedance Characteristics of Porous La[sub 1−x]Sr[sub x]CoO[sub 3−δ] Electrodes*. Journal of the Electrochemical Society, 2009. **156**(4): p. B513-B525.

26. Kresse, G. and J. Hafner, *Ab initio molecular dynamics for liquid metals*. Physical Review B, 1993. **47**: p. 558.

27. Kresse, G. and J. Furthmuller, *Efficient iterative schemes for ab initio total-energy calculations using a plane-wave basis set*. Physical Review B, 1996. **54**(16): p. 11169-11186.

28. Blochl, P.E., *Projector Augmented-Wave Method*. Physical Review B, 1994. **50**(24): p. 17953-17979.

29. Perdew, J.P. and Y. Wang, *Accurate and simple analytic representation of the electron-gas correlation energy*. Physical Review B, 1992. **45**(Copyright (C) 2010 The American Physical Society): p. 13244.

30. Anisimov, V.I., F. Aryasetiawan, and A.I. Lichtenstein, *First-principles calculations of the electronic structure and spectra of strongly correlated systems: The LDA+U method*. Journal of Physics-Condensed Matter, 1997. **9**(4): p. 767-808.

31. Dudarev, S.L., et al., *Electron-energy-loss spectra and the structural stability of nickel oxide: An LSDA+U study*. Physical Review B, 1998. **57**(3): p. 1505-1509.

32. Gadre, M.J., Y.L. Lee, and D. Morgan, *Cation interdiffusion model for enhanced oxygen kinetics at oxide heterostructure interfaces*. Phys Chem Chem Phys, 2012. **14**(8): p. 2606-16.

33. Lee, Y.-L., et al., *Ab initio energetics of LaBO[sub 3](001) (B = Mn, Fe, Co, and Ni) for solid oxide fuel cell cathodes*. Physical Review B (Condensed Matter and Materials Physics), 2009. **80**(22): p. 224101.

34. Wang, L., T. Maxisch, and G. Ceder, *Oxidation energies of transition metal oxides within the GGA+U framework*. Physical Review B, 2006. **73**(19): p. 195107.

35. Mayeshiba, T., H. Wu, and D. Morgan. *MAterials Simulation Toolkit (MAST)*. 2015; Available from: https://pypi.python.org/pypi/MAST/

36. Angsten, T., et al., *Elemental vacancy diffusion database from high-throughput first-principles calculations for fcc and hcp structures*. New Journal of Physics, 2014. **16**(1): p. 015018.

37. NIST, *NIST Chemistry WebBook*, in *NIST Standard Reference Database No. 69,* http://webbook.nist.gov/chemistry/, P.J. Linstrom and W.G. Mallard, Editors. 2003, National Institute of Standards and Technology: Gaithersburg, MD.

38. Lee, Y.-L. and D. Morgan, *Ab initio and empirical defect modeling of LaMnO3+/-[small delta] for solid oxide fuel cell cathodes*. Physical Chemistry Chemical Physics, 2012. **14**(1): p. 290-302.

39. Zunger, A., et al., *Special Quasirandom Structures*. Physical Review Letters, 1990. **65**(3): p. 353-356.

40. van de Walle, A., M. Asta, and G. Ceder, *The Alloy Theoretic Automated Toolkit: A user guide*. Calphad-Computer Coupling of Phase Diagrams and Thermochemistry, 2002. **26**(4): p. 539-553.

41. MAST-development-team, *MAterials Simulation Toolkit (MAST)*. 2014: http://pypi.python.org/pypi/MAST.

42. Angsten, T., et al., *Elemental vacancy diffusion database from high-throughput first-principles calculations for fcc and hcp structures*. New Journal of Physics, 2014. **16**.

43. Tarancon, A., et al., *Advances in layered oxide cathodes for intermediate temperature solid oxide fuel cells*. Journal of Materials Chemistry, 2010. **20**(19): p. 3799-3813.

44. Lee, Y.-L., et al., *Prediction of solid oxide fuel cell cathode activity with first-principles descriptors*. Energy & Environmental Science, 2011. **4**(10): p. 3966.

45. Mauvy, F., et al., *Electrode properties of Ln2NiO4 + δ (Ln = La , Nd , Pr) : AC Impedance and DC Polarization Studies*. Journal of The Electrochemical Society, 2006. **153**(8): p. A1547-A1553.

46. Escudero, M.J., et al., *A kinetic study of oxygen reduction reaction on La2NiO4 cathodes by means of impedance spectroscopy*. Journal of Electroanalytical Chemistry, 2007. **611**(1–2): p. 107-116.

47. Burriel, M., et al., *Anisotropic oxygen diffusion properties in epitaxial thin films of La2NiO4+[small delta]*. Journal of Materials Chemistry, 2008. **18**(4): p. 416-422.

48. Munnings, C.N., et al., *Oxygen transport in the La2Ni1-xCoxO4+d system*. Solid State Ionics, 2005. **176**(23,Äì24): p. 1895-1901.

49. Sayers, R., et al., *Low temperature diffusion and oxygen stoichiometry in lanthanum nickelate*. Solid State Ionics, 2010. **181**(8–10): p. 386-391.

50. Claus, J., et al., *Combination of EBSP measurements and SIMS to study crystallographic orientation dependence of diffusivities in a polycrystalline material: oxygen tracer diffusion in La2 − xSrxCuO4 ± δ*. Materials Science and Engineering: B, 1996. **38**(3): p. 251-257.

51. Feng, Z., et al., *Anomalous Interface and Surface Strontium Segregation in (La1-ySry)2CoO4±δ/La1-xSrxCoO3-δ Heterostructured Thin Films*. Journal of Physical Chemistry Letters, 2014. **5**: p. 1027–1034.

52. Wang, F., et al., *The crystal structure, oxygen nonstoichiometry and chemical stability of Ba0.5Sr0.5Co0.8Fe0.2O3-[small delta] (BSCF)*. Physical Chemistry Chemical Physics, 2014. **16**(16): p. 7307-7314.

53. Bucher, E., et al., *Oxygen nonstoichiometry and exchange kinetics of Ba0.5Sr0.5Co0.8Fe0.2O3-delta*. Solid State Ionics, 2008. **179**(21-26): p. 1032-1035.

54. Wang, L., et al., *Oxygen tracer diffusion in dense Ba[sub 0.5]Sr[sub 0.5]Co[sub 0.8]Fe[sub 0.2]O[sub 3 - delta] films*. Applied Physics Letters, 2009. **94**(7): p. 071908.

55. Cheng, J., et al., *Thermochemistry of La1-xSrxFeO3-δ Solid Solutions ($0.0 \leq x \leq 1.0$, $0.0 \leq \delta \leq 0.5$)*. Chemistry of Materials, 2005. **17**(8): p. 2197-2207.

56. Cheng, J.H., et al., *Enthalpies of formation of LaMO3 perovskites (M = Cr, Fe, Co, and Ni)*. Journal of Materials Research, 2005. **20**(1): p. 191-200.

57. Prasanna, T.R.S. and A. Navrotsky, *Energetics of La2-xSrxCoO4-y ($0.5 < x < 1.5$)*. Journal of Solid State Chemistry, 1994. **112**(1): p. 192-195.

58. Lee, W., et al., *Cation Size Mismatch and Charge Interactions Drive Dopant Segregation at the Surfaces of Manganite Perovskites*. Journal of the American Chemical Society, 2013. **135**(21): p. 7909-7925.

59. Oh, D., D. Gostovic, and E.D. Wachsman, *Mechanism of La0.6Sr0.4Co0.2Fe0.8O3 cathode degradation*. Journal of Materials Research, 2012. **27**(15): p. 1992-1999.

60. Cherepanov, V.A., et al., *Phase equilibria in the La-Me-Co-O (Me=Ca, Sr, Ba) systems*. Ionics, 1998. **4**(3-4): p. 309-315.

61. Saal, J.E., et al., *Thermodynamic Properties of Co3O4 and Sr6Co5O15 from First-Principles*. Inorganic Chemistry, 2010. **49**(22): p. 10291-10298.

62. Kuhn, M., et al., *Oxygen nonstoichiometry and thermo-chemical stability of La0.6Sr0.4CoO3,àíŒ¥*. Journal of Solid State Chemistry, 2013. **197**(0): p. 38-45.

63. Druce, J., T. Ishihara, and J. Kilner, *Surface composition of perovskite-type materials studied by Low Energy Ion Scattering (LEIS)*. Solid State Ionics, (in press, 2013).

64. Crumlin, E.J., et al., *Surface strontium enrichment on highly active perovskites for oxygen electrocatalysis in solid oxide fuel cells*. Energy & Environmental Science, 2012. **5**(3): p. 6081-6088.

65. Lee, D., et al., *Surface Oxygen Kinetics and Stability of (La,Sr)2CoO4±δ/La0.8Sr0.2MO3-δ (M = Co and Fe) Hetero-interfaces at Elevated Temperatures*. Submitted, 2014.

66. Fischer, E., W.D. Shen, and J.L. Hertz, *Measurement of the surface exchange and diffusion coefficients of thin film LaCoO3 and SrCoOx*. Journal of Electroceramics, 2012. **29**(4): p. 262-269.

67. Vashook, V.V., et al., *Oxygen non-stoichiometry and electrical conductivity of the binary strontium cobalt oxide SrCoOx*. Solid State Ionics, 1997. **99**(1-2): p. 23-32.

68. Yokokawa, H., et al., *Thermodynamic and kinetic considerations on degradations in solid oxide fuel cell cathodes*. Journal of Alloys and Compounds, 2008. **452**(1): p. 41-47.

69. Hayd, J., H. Yokokawa, and E. Ivers-Tiffee, *Hetero-Interfaces at Nanoscaled (La,Sr)CoO3-delta Thin-Film Cathodes Enhancing Oxygen Surface-Exchange Properties*. Journal of the Electrochemical Society, 2013. **160**(4): p. F351-F359.

70. Morin, F., G. Trudel, and Y. Denos, *The phase stability of La0.5Sr0.5CoO3-delta*. Solid State Ionics, 1997. **96**(3-4): p. 129-139.

71. Ovenstone, J., J.S. White, and S.T. Misture, *Phase transitions and phase decomposition of La1-xSrxCoO3-delta in low oxygen partial pressures*. Journal of Power Sources, 2008. **181**(1): p. 56-61.

72. Harrison, W.T.A., S.L. Hegwood, and A.J. Jacobson, *A powder neutron diffraction determination of the structure of Sr6Co5O15, formerly described as the low-temperature hexagonal form of SrCoO3*. Journal of the Chemical Society, Chemical Communications, 1995(19): p. 1953-1954.

73. Nakagawa, N., H.Y. Hwang, and D.A. Muller, *Why some interfaces cannot be sharp*. Nat Mater, 2006. **5**(3): p. 204-209.

74. Unemoto, A., et al., *Oxygen Reduction at the Surface and the Hetero-Interface of La-Sr-Co-O-Oxides*, in *Ionic and Mixed Conducting Ceramics 7*, M. Mogensen, et al., Editors. 2010, Electrochemical Soc Inc: Pennington. p. 59-70.

75. Grimaud, A., et al., *Double Perovskite as a Family of Highly Active Catalysts For Oxygen Evolution in Alkaline Solution*. Nature Communication, 2013. **4**: p. 2439.